1986

ROLE OF NUCLEATION ENTROPY IN PRECIPITATION IN ALUMINUM-COPPER ALLOY.

J. KAROV
University of Windsor

Recommended Citation
KAROV, J., "ROLE OF NUCLEATION ENTROPY IN PRECIPITATION IN ALUMINUM-COPPER ALLOY." (1986). *Electronic Theses and Dissertations.* Paper 3364.

National Library
of Canada

Bibliothèque nationale
du Canada

Canadian Theses Service

Services des thèses canadiennes

Ottawa, Canada
K1A 0N4

CANADIAN THESES

NOTICE

The quality of this microfiche is heavily dependent upon the quality of the original thesis submitted for microfilming. Every effort has been made to ensure the highest quality of reproduction possible.

If pages are missing, contact the university which granted the degree.

Some pages may have indistinct print especially if the original pages were typed with a poor typewriter ribbon or if the university sent us an inferior photocopy.

Previously copyrighted materials (journal articles, published tests, etc.) are not filmed.

Reproduction in full or in part of this film is governed by the Canadian Copyright Act, R.S.C. 1970, c. C-30.

THIS DISSERTATION
HAS BEEN MICROFILMED
EXACTLY AS RECEIVED

THÈSES CANADIENNES

AVIS

La qualité de cette microfiche dépend grandement de la qualité de la thèse soumise au microfilmage. Nous avons tout fait pour assurer une qualité supérieure de reproduction.

S'il manque des pages, veuillez communiquer avec l'université qui a conféré le grade.

La qualité d'impression de certaines pages peut laisser à désirer, surtout si les pages originales ont été dactylographiées à l'aide d'un ruban usé ou si l'université nous a fait parvenir une photocopie de qualité inférieure.

Les documents qui font déjà l'objet d'un droit d'auteur (articles de revue, examens publiés, etc.) ne sont pas microfilmés.

La reproduction, même partielle, de ce microfilm est soumise à la Loi canadienne sur le droit d'auteur, SRC 1970, c. C-30.

LA THÈSE A ÉTÉ
MICROFILMÉE TELLE QUE
NOUS L'AVONS REÇUE

NL-339 (r.86/06)

Canada

ROLE OF NUCLEATION ENTROPY IN PRECIPITATION IN Al-Cu ALLOY

by

J. Karov

A Dissertation
Submitted to the Faculty of Graduate Studies
Through the Department of Engineering Materials
In Partial Fulfillment of the Requirements
For the Degree of Doctor of Philosophy
at the University of Windsor

Windsor, Ontario
1985

ISBN 0-315-29300-4

To Jenny, Yanir, Daniel
and Ron

ABSTRACT

The study of the effect of Be on precipitation in Al-3%Cu alloy is focussed on the clustering process, GP zone formation, and the θ'→θ transformation. An accelerated hardening is observed in the Al-3%Cu-0.1%Be alloy (weight percent) as compared to Al-3%Cu, when aged at room temperature and at 110°C. TEM analysis shows that GP zones are not present in Al-3%Cu-0.1%Be alloy aged to the hardness plateau, indicating that the faster hardening is not due to GP zone formation. A clustering process, in which clusters of Cu and Be atoms with vacancies are formed around dislocation lines, is proposed to explain the delay in GP zone formation and the observed rapid hardening.

The θ' and θ precipitation in the alloys is investigated using a resistivity technique, and the precipitation can be described by Avrami type equation. Similar activation energies and 'n' constants indicate that the addition of Be does not alter the growth mechanism of θ' and θ. A faster and earlier θ'→θ transition in Al-3%Cu-0.1%Be alloy is established using both TEM and resistivity techniques. The higher 'k' values of the Avrami equation and the larger θ particle density observed initially in Al-3%Cu-0.1%Be alloy, suggest that Be increases the nucleation rate of θ phase.

Strain energy for the formation of incoherent θ precipitate was calculated and found to be higher when Be is incorporated in the θ phase. The nucleation entropy of θ was estimated using the appropriate sequence of reactions. For

θ phase with Be, substantially larger (absolute) entropy change was obtained, indicating that the observed higher nucleation rate of θ phase (with Be) is in agreement with the nucleation entropy theory.

ACKNOWLEDGEMENTS

The author wishes to express his gratitude to Dr. W.V. Youdelis for his guidance, supervision and valuable discussions throughout this work. He would like to thank Mr. G. Vazsonyi and Mr. J. Robinson for their assistance with optical metallography and electron microscopy, respectively, and to Dr. R. Herring who carried out the dislocation loop analysis. Acknowledgement is given to the Aluminum Company of Canada for supplying the super-purity Al. The author also wishes to thank the Natural Sciences and Engineering Research Council of Canada for their financial support of this project in the form of a research grant.

TABLE OF CONTENTS

Page

/

LIST OF FIGURES

LIST OF TABLES

Table | Page

CHAPTER I

INTRODUCTION

The discovery of GP zones (1938) was followed by extensive study of aluminum alloys and led to better understanding of precipitation process in the solid-state. It is now well established that the stable phases in most alloys are the end product of a precipitation sequence in which clusters and metastable phases are formed first. Control of the precipitation sequence, coherency, and densities of particles can be exercised through proper aging conditions, and the resulting mechanical properties can be "tailored" for specific uses.

The addition of trace elements to Al-alloys affects strongly the aging response, mainly by changing the vacancy concentration and the thermodynamic characteristics of the precipitate phase. Decrease in vacancy concentration, for example, will drastically lower the diffusion rate and consequently the growth rate of precipitates. Incorporation of trace elements into the precipitate phase could change the interfacial, strain and free energy of formation. The latter, which can be related to the mixing or configurational entropy change for the system, is of particular interest, since the nucleation rate is greatly affected by small entropy changes accompanying the transformation.

In the present study, the effect of Be on the precipitation in Al-3%Cu alloy is investigated. The enhanced clustering and delay in GP zone formation that results when small amounts of Be are added is explained by the increased stability of clusters, and the corresponding depletion of Cu and vacancies in the matrix. In the study of θ' and θ formation, the onset of θ precipitation is investigated by combining TEM and resistivity techniques. For the analysis of Be in the θ phase, several analytical techniques were combined: X-ray diffraction, metallography, extraction technique and the difference method of Energy Dispersive Analysis.

The significantly higher nucleation rate of θ in Al-3%Cu-0.1%Be alloy compared to the Al-3%Cu alloy, as evidenced by the higher precipitate particle density and shorter transformation times, is explained using the nucleation entropy theory. The complete reaction sequence is analyzed in interpreting the results of the investigation, i.e., the stages including the initial cluster formation, through the transition GP zones, θ' and finally the stable θ phase formation.

CHAPTER II

LITERATURE REVIEW

A. PRECIPITATION IN Al-Cu ALLOY

(1) Introduction

In 1938 Guinier(1) and Preston(2) independently announced new experimental results from an X-ray study on single crystals of Al-Cu alloy: streaks on a Lauë photograph indicating the presence of Cu-rich zones on the (200) planes of Al. Preston(3) found that during subsequent aging the streaks broke up into discrete spots due to the formation of the metastable phase θ', and that overaging induced the transition from θ' to the equilibrium phase θ. Guinier(4) detected an additional metastable phase which preceeds θ', which is generally designated as θ". Silcock, Heal and Hardy(5) carried out the first comprehensive examination of the structural changes, hardness, and the zone size during aging. At 130°C the reaction sequence is represented by

$$\text{(supersaturated matrix)} \rightarrow \text{GP1} \rightarrow \text{GP2} \rightarrow \theta' \rightarrow \theta. \quad (1)$$

(2) Clustering

De Sorbo et al(6) used resistivity and calorimetry techniques to study clustering which preceeds GP zone formation. A 5% increase in the resistivity with an energy release of 238 J/g.atom of alloy were observed. The clustering process has an activation energy of 50.2 kJ/g. atom and the isothermal clustering rate decreases with time. The results indicate that a vacancy mechanism is involved in the clustering of Cu atoms. Turnbull et al$^{(7)}$ studied the resistivity change in Al-Cu and other Al alloys. Distinction was made between the initial, fast, and the latter, slower reaction. The initial clustering proceeds with an activation energy of 48.2 kJ/mole and is independent of the solute concentration. A model in which the resistivity change consists of clustering of Cu atoms and the annealing of vacancies was proposed. It was also suggested that the clustering is a surface energy driven process, without a nucleation barrier, and a kinetic equation derived. The latter and slower reaction proceeds for days, at a rate which indicates a presence of a high, non-equilibrium concentration of vacancies. Several explanations were offered, including the presence of stable vacancy clusters. Tucker and Webb$^{(8)}$ have shown that the clustering process proceeds by a vacancy mechanism, which can be promoted by electron irradiation. Hart$^{(9)}$ has proposed the formation of vacancy-Cu clusters which migrate through the matrix, collecting more solute atoms. One of the possible consequences of this mechanism is the formation of new metastable phases. The concept of "ternary clusters" consisting of Cu, Mg and vacancies was used by Entwistle et al$^{(10)}$ to explain the accelerated hardening in Al-Cu-Mg alloy. Holmes and Noble$^{(11)}$ suggested that Cu-Cd-vacancy clusters cause the observed anomalous rise in resistivity in Al-Cu-Cd alloy and Noble$^{(12)}$ proposed the existence of mobile-vacancy-solute clusters in Al-Cu alloy with trace quantities of Cd, In or Sn. Takahashi et al$^{(13)}$ used the combined hardness, resistivity, X-ray and the TEM techniques, in the study of aging in Al-2%Cu* with traces of Sn. Cu clusters were found to form in the quenched alloy, prior to GP zone formation, and disappeared on subsequent aging. Abe et al(14) observed spherical Cu clusters while studying GP1 and GP2 structures by Field Ion Microscope (FIM). Yoshida et al(15) used the TEM lattice imaging technique and detected clusters of Cu on (111) planes. The clusters have diameters of less than 10 atoms and disappear at a later stage.

(3) GP1 and GP2 (θ'')

The first model of GP zones is due to Guinier(16) and Preston(3) who proposed a single layer of Cu on the (200) matrix planes with the surrounding Al planes displaced toward it. Guinier(4,17) also proposed that GP2 consist of (200) planes spaced 0.2:0.19:0.19:0.2 nm apart. The central plane was envisaged as 100%Cu, the next two planes - mixture of Cu and Al and the two basal planes 100%Al, giving the overall composition of $CuAl_2$. The structure of GP2 is tetragonal with a = 0.404 nm and c = 0.79 nm. Silcock et al(5) reported a change in c from 0.80 to 0.76 nm during aging at 130°C, but a constant (0.76 nm) on aging at 190°C. A structure of alternate Cu and Al planes was suggested for GP2 by Nicolson and Nutting(18). Gerold(19,20) proposed that the displacement field around GP1 zones disappears at the 14th plane, and Toman(21,22) suggested that the displacement field diminishes after the 4th plane and allowed the concentration of Cu to

---

* Concentrations, weight percent indicated by %, atomic percent % omitted.

drop gradually over 10 planes. The proposed Cu gradient in Toman's model was proven incorrect (Toman(23)) as it requires too much copper. Nicholson and Nutting(18), using TEM, observed strong contrast fields sensitive to tilt associated with the GP1 and GP2 zones due to the coherency strains. Parson et al(24) used two beam lattice images and resolved the 0.202 nm spacing of (200) planes in Al-4%Cu. Tensile distortion was observed 2-3 nm from each side of the zone.

Philips(25) studied GP zones immediately after quench and after longer aging treatments (4 days at 130°C). Groups of GP zones, 0.2-0.4 nm thick and 1-6.5 nm in diameter were observed in the quenched material. The displacement field was found to be complex and fell to zero approximately 1.6 nm from the zone. GP zones after longer aging treatment were 0.2-1 nm thick and 4-24 nm in diameter. The thicker zones show bending of matrix planes toward the zone and the displacement field extends outwards 3 nm. Moire fringes were observed on some GP zones and their spacing suggests that the thicker zones have 100%Cu on the surface and approximately 20%Cu in the centre. Philips(26) also observed a continuous structural progression from GP1 to GP2 zones, which is associated with diffuse maxima on GP1 streaks in electron diffraction patterns, and resolved the c planes of GP2 spaced 0.79nm apart.

Yoshida et al(27) used the weak beam technique to analyze the GP1 and GP2 structures. The experimental images were analyzed by comparison to the computed image profiles based on the model of edge dislocation loop with adjustable burger vector and the loop radius. Best fit was obtained with $\bar{b}$ = 0.2a indicating much faster decrease in displacement than proposed by Gerold's model. GP2 zones appeared wider and were often accompanied by a number of closely spaced fringes. Auvray et al(28) analyzed GP zones with diffuse X-ray scattering technique and found that the zones are single or multi layers of 100%Cu with the nearest neighbour spacing as in matrix. The matrix is depleted of Cu, the (200) matrix planes collapse toward the zone, and the displacement field decreases more rapidly than predicted by Gerold model. Yoshida(29) observed normal distributions of GP1 and GP2 and concluded that the mechanism of nucleation and growth of GP zones proceeds by random walk of the solute atoms. The transition from GP1 to GP2 occurs at critical GP1 size which is a function of the aging conditions. Abe et al(30) used FIM to study GP1 and GP2 and found that GP1 zones are Cu-rich, plate-like zones, ~~non~~ homogeneous in thickness, complex in shape containing ledges, holes and Al atoms. The GP2 zones consist of two parallel, Cu-rich layers separated by matrix planes. Yoshida et al(15) employed lattice imaging technique and observed single layer GP1 zones and double layer GP2 separated by 2-3 planes of Al.

(4) θ' and θ

Silcock et al(5) have established the bct structure of θ' with a = 0.404 nm and c = 0.58 nm, and confirmed the bct structure of θ with a = 0.6076 nm and c = 0.4874 nm reported by Bradley and Jones(31). They also showed that under suitable conditions the first phase detected can be GP1, GP2 or

θ', implying that direct nucleation of the various phases is possible. Laird and Aaronson(32,33) and Sankaran and Laird(34) studied the θ'/α interface and the migration kinetics. Broad θ' faces are initially coherent, but interface dislocations are observed at a later stage as the result of plastic deformation during the θ' growth. The thickening of θ' plates is slower than required for a volume diffusion controlled rate, and interface controlled kinetics is proposed. However, the thickening proceeds by lateral movement of ledges which itself is volume diffusion controlled. Chen and Doherty(35) argued that the thickening rate can be described as a volume diffusion process. Papazian(36) using differential scanning calorimetry (DSC) found that θ' formation can be described by an Avrami equation with $n = 1-1.2$ and concluded that the overall reaction is diffusion controlled. Melle et al(37) employed hardness measurements and TEM in studying θ' growth, and also proposed an Avrami equation with an activation energy of 106 kJ to describe the θ' growth.

Several mechanisms for $\theta' \rightarrow \theta$ transition have been proposed. Direct nucleation of θ on θ' has been reported(26,38), but it has also been proposed(39) that nucleation of θ from the matrix is possible. Laird and Aaronson(40) found that only a small fraction of θ' serve as nucleation sites for θ, the latter growing by consuming the θ' host while nearby θ' precipitates dissolve. The controlling factor of θ formation is the concurrent growth of θ into the matrix rather than the θ' consumption. The calculated diffusion coefficient is an order of magnitude higher than the value reported by Murphy(41) due to the surface contribution to diffusion in thin foils. The lengthening rate of θ precipitates is constant whereas the shortening rate of the dissolving θ' particles increases with time.

Kang and Laird(42) studied the θ precipitation in thin foils using hot stage electron microscopy. Dislocations and ledges were observed on broad faces of θ and the morphology is sensitive to the degree of supercooling. Kinsman et al(38) investigated the α/θ interface and established, contrary to previous views, that the interface is not completely incoherent. In a recent study, Buttler(43) observed a dislocations net linking θ' to θ during θ'→θ transition, and proposed that the θ' dissolution occurs by an atomic detachment followed by a pipe diffusion.

B. TRACE ELEMENTS IN Al-Cu ALLOY

Sully et al(44) observed that small quantities of tin increase the ductility of solution treated material. The natural aging rate is lower but higher hardness, yield and ultimate strength values are obtained for artificially aged samples. Hardy(45) and Hardy et al(46) found that Al-Cu alloy with trace amounts of In or Sn tends to a single stage aging process. The overall aging process is faster and a higher maximum hardness is obtained. These observations were interpreted as an accelerated GP2 formation caused by short range grouping of Cu and trace elements.

Silcock et al(47) used X-ray diffraction to study the effect of Cd, In, and Sn, and found that both GP1 and GP2, are suppressed while θ' formation is enhanced. Additional diffraction effects, relpoints and relrods, appear to be related to the θ' formation and originate from structural modification around θ' particle. Such modification could result in easier θ' nucleation. Silcock(48) suggested that Cd or In form an effective nucleus for θ', and noted that fast quenching or cold working can destroy this effect. Entwistle et al(10) proposed that a segregation of vacancies to In atoms slows down the Cu diffusion and suppresses GP zone formation. Holmes and Noble(11) observed a raise in resistivity, which is attributed to the formation of Cu-Cd vacancy clusters. It was suggested, based on activation energy calculation, that diffusion of the entire cluster rather than Cu atoms occurs, and that the coalescence of the clusters form a θ' nucleus.

Nuyten(49) studied "quenched-in" loops in Al-Cu, and observed a higher loop density with smaller average size when Cd is present in the alloy. Upon aging at 218°C, θ' nucleated on the large loops resulting in denser θ' population. A mechanism in which Cd stabilizes the loops and keeps vacancies available for diffusion and faster θ' formation was proposed. Noble(12) extended the "mobile cluster" model(11) to Al-Cu alloys containing In or Sn. The θ' nucleation in these alloys is thought to occur by a coalescence of these clusters, while the growth of θ' is controlled by the diffusion of clusters to the θ' particle.

Das et al(50) reported that 2021 Al-alloy containing traces of Cd and Sn, when aged 24 h at 163°C, exhibits only

θ', while the binary Al-4%Cu has a mixture of θ'' and θ'. The strain fields of θ' in the ternary alloy are similar to those of θ'' in binary alloy, implying that the particles θ' are coherent with matrix, with the coherency maintained by the segregation of trace elements to the α/θ' interface. The trace elements also reduce the θ' size. This observation is explained by assuming that Cu-Cd-Sn-vacancy clusters limit the growth rate of θ'. The nucleation of θ' appears to be homogeneous, possibly due to lower surface energy of θ' in 2021 alloy with trace elements.

Sankaran and Laird(51) used TEM and detected Cd, In, and Sn segregation around θ' plate edges. The broad θ' faces show higher density of ledges when trace elements are present, but the growth rate is not affected. The kinetic analysis suggests that the trace elements reduce the critical radius of θ' plate. Suzuki et al(52) found that the effect of Sn in Al-Cu depends critically on aging temperature and Cu content and that the aging rate can be retarded or enhanced. Secondary defects, vacancy sinks and sources are invoked to explain this behaviour.

Trace elements other than Cd, In, and Sn were studied less intensively. Fink et al(53) reported that 0.25%Mn has no appreciable influence on the aging of Al-Cu alloy, but 0.5-1% reduces the aging response. Chitty(54) found that Si increases the quenched and peak hardness as well as the aging rate. Above 0.9% no further change in hardness and aging rate is observed as the solubility of Si in Al is exceeded.

Mn addition up to the solubility limit increases the quenched and the peak hardness, and accelerates the hardening, but beyond the solubility limit (~0.21%) a decrease in hardness and aging rate are observed due to formation of the T phase which removes Cu from solid solution. Chitty(54) observed only decrease in hardness and the hardening rate in Al-Cu with traces of Fe. This is consistent with the low solubility (0.01%) of Fe and the formation of β phase which depletes the matrix of Cu. It is also in agreement with other workers (55-56), who found that even small amount of iron (~0.1%) inhibits the aging behaviour of Al-Cu alloy due to formation of ternary phases.

Nuyten(57) studied the effect of 0.007%Be in Al-3.9%Cu alloy and found that Be lowers the hardness at room temperature. A mechanism in which Be traps vacancies and thereby reduces the GP zone formation was proposed. Aging at 218°C produced many dislocation loops on which a heterogeneous θ' precipitation was observed. According to Entwistle et al(10) 0.04%Mg has little effect, while quantities above 0.09% accelerate age hardening and ternary GP zones are formed.

The combined effect of Ag, Sn, Cd or In when added to Al-Cu was studied by Noble(12) who found that 1% of Ag added to Al-Cu-Cd alloy suppresses θ' precipitation, but has no effect on Al-Cu-Sn alloy. In Al-Cu-In-Ag alloy delayed θ' nucleation resulted in coarser precipitates. Noble et al(58) found that 0.4-1.5%Li in Al-4.5%Cu results in the formation of two kinds of GP zones. Zones of Cu were observed during aging between 0°-50°C, but their formation was retarded due to the reduction of quenched-in vacancies. Aging between 80°C-130°C caused Cu-Li zones to form. The θ' formation was accompanied by an anomalous rise in resistivity due to Cu-Li clusters or small θ' precipitates.

It appears that the trace elements can be divided into two groups:

(a) trace elements that change the vacancy availability, distribution, or condensation. Change in one or all of these characteristics will markedly affect the diffusion and the kinetics of the precipitation. The GP zone formation may be delayed or accelerated and the growth of the latter, more stable phases will be affected as well. Vacancy loops, in the case of massive vacancy condensation, will not only deplete the matrix of vacancies, but also serve as nucleation sites for phases that favour heterogeneous nucleation. When insoluble phases are formed as the result of the trace element presence, the role of these phases as vacancy sinks must be considered.

(b) trace elements that change the structure and the composition of the new phase. By taking part in the new phase, the trace element will modify the thermodynamic properties like surface energy, strain energy and the volume free energy.

C. NUCLEATION IN CONDENSED SYSTEMS

(1) Classical Nucleation Theory

The classical theory for nucleation from vapour phase, as first developed by Volmer and Weber$^{(59)}$, Becker and

Doring(60) (referred to as the V.W.B.D. theory) was extended by Turnbull and Fisher(61) to describe homogeneous nucleation in a condensed system. As in the V.W.B.D. theory, a steady state distribution of embryos with 'n' atoms is assumed giving:

$$N_n = N_o \exp[-\Delta G_n/kT] \qquad (2)$$

where N_o, N_n and ΔG_n are the total number of atoms in the system, the number of embryos with n atoms and the free energy of formation respectively. Critical sized embryos (with n* atoms) transform into stable nuclei by absorbing an additional atom. For a spherical embryo, in the absence of strain energy, the free energy of formation ΔG is:

$$\Delta G = \frac{4}{3}\pi r^3 \Delta G_v + 4\pi r^2 \gamma \qquad (3)$$

where r, ΔG_v and γ are the radius, the free energy change per unit volume and the interfacial energy respectively. Minimizing eqn. (3) with respect to 'r' gives for the free energy of formation of critical sized embryos:

$$\Delta G^* = \frac{16\pi\ \gamma^3}{3(\Delta G_v)^2} \qquad (4)$$

and the number of critical sized embryos is given by:

$$N_n^* \propto \exp[-16\pi\gamma^3/3\Delta G_v^2\ kT] \qquad (5)$$

The resulting homogeneous nucleation rate, which is proportional to the density of critical embryos and the diffusion rate across the embryo's boundary may be expressed as:

$$\dot{N} = K \exp[-\frac{16\pi\ \gamma^3}{3(\Delta G_v)^2 kT}] \qquad (6)$$

where the parameter K includes the embryo surface concentration of atoms and the jump frequency for the atom which has an exponential dependency on the activation energy for diffusion ($e^{-E_{diff}/kT}$).

For heterogeneous nucleation, substrates reduce the surface energy needed to form a nucleus, and thereby decrease the free energy of formation of the critical sized nucleus by a factor that is a function of the contact angle (θ) at the nucleus/substrate interface. The substrate effect is included in expressing the free energy change for the formation of a critical sized embryo for the heterogeneous case (ΔG^*_{het}) thus,

$$\Delta G^*_{het} = \frac{16\pi\gamma^3}{3(\Delta G_v)^2} f(\theta) \qquad (7)$$

where the function $f(\theta)$ is given by,

$$f(\theta) = (2-3\cos\theta + \cos^3\theta)/4 \qquad (8)$$

(2) <u>The Nucleation Entropy Theory</u>

Although ΔG_v may be formally related to extensive and partial molar free energies of the solid and liquid solutions (e.g., see Christian$^{(62)}$), this approach for calculating ΔG_v is not feasible for most alloy systems since the free energy data for the solutions are not available. The volume free energy of nucleation may be more usefully, albeit approximately, related to the volume entropy change for the transformation and the degree of supercooling.

It can be shown that $\Delta G_v \simeq -\Delta S_v \Delta T$ where ΔS_v is the volume entropy of nucleation (entropy change for the solid/liquid system per unit volume of solid phase nucleated). Substitution of the above for ΔG_v into the classical nucleation rate expression gives,

$$\dot{N} \propto \exp[-K.16.\pi.\gamma^3/3(\Delta S_v)^2(\Delta T)^2.kT] \qquad (9)$$

where K is a parameter determined by nucleus geometry, contact angle (for heterogeneous nucleation), etc., and ΔT is the degree of supercooling. It is evident from eqn. (9) that the nucleation rate in alloys increases exponentially with the square of the volume entropy of nucleation, and alloy systems having high nucleation entropies should correspondingly exhibit fine solidification structures.

(a) Nucleation Entropy for Binary and Multicomponent Systems

Youdelis(63) has derived an expression for the nucleation entropy for the special case of regular solution behaviour for binary alloy phases, assuming isothermal, isobaric, constant phase-composition conditions are maintained during nucleation. The molar entropy of nucleation $\Delta S (= V_m \, \Delta S_v$, where V_m denotes the molar volume) can be separated into two parts: the entropy change due to freezing of the pure components (ΔS_F) and the change in the mixing entropy for the solid/liquid system resulting from the precipitation of the solid phase (ΔS_M), i.e.,

$$\Delta S = \Delta S_F + \Delta S_M \qquad (10)$$

where,

$$\Delta S_F = N_1^s(S_1^s - S_1^\ell) + N_2^s(S_2^s - S_2^\ell) \qquad (11)$$

and,

$$S_M = R[N_1^s \, \ell n(N_1^\ell/N_1^s) + N_2^s \, \ell n(N_2^\ell/N_2^s)] \qquad (12)$$

In the above equations, the N's refer to the mole fractions, the S's to the molar entropies, the subscripts 1, 2 to the components, the superscripts s, ℓ to the solid and liquid phases respectively.

The extension of eqns. (11) and (12) to the multicomponent system is straightforward and is obtained by including terms for all components in the system in the equations for the binary system(64), thus

$$\Delta S_F = \sum_{r=1}^{n} N_r^s (S_r^s - S_r^\ell) \tag{13}$$

and,

$$\Delta S_M = R \sum_{r=1}^{n} N_r^s \ell n (N_r^\ell / N_r^s) \tag{14}$$

where N_r^s and N_r^ℓ refer to the mole fractions of the rth component in the solid and liquid phases respectively, and S_r^s and S_r^ℓ are the molar entropies of the rth component in the pure solid and liquid states respectively at the nucleation temperature.

The application of eqns. (13) and (14) to simple binary eutectic systems shows that in general $|\Delta S_M|$ increases with increasing separation of solidus and liquidus lines and for the eutectic system is maximum at the eutectic composition. It follows that the nucleation rate (and thus grain refinement) should increase with solute concentration for a binary eutectic system; and moreover, that the tendency for nucleation and grain refinement should be particularly strong in alloys precipitating primary phases or intermetallic compounds of components present in the alloy in dilute concentration.

The behaviour of ΔS_F and ΔS_M for the multicomponent system will be similar to that for the binary system, i.e., both ΔS_F and ΔS_M are always negative and $|\Delta S_M|$ increases with difference in composition between solid and liquid phases. For the multicomponent system $|\Delta S_M|$ will also increase with the number of components present in the system. This is so particularly for the precipitation of intermediate compounds or phases of limited solubility range, when only the principal component (solvent, 1) is concentrated in the liquid phases ($N_1^\ell > N_1^s$), and the remaining minor components (solutes 2,3,...,n) are concentrated in the solid phase ($N_r^\ell << N_r^s$, r = 2,3,...,n), so that only the first term in eqn. (14) is positive (decreasing $|\Delta S_M|$), while the remaining terms are negative. In general, since a redistribution of all components necessarily occurs during the nucleation of the primary phase or intermediate compound in the liquid alloys, it follows that the nucleation entropy and corresponding nucleation rate (other factors being equal) increase with the number of components comprising the alloy system and results in an increased refinement of the solidification structure.

(b) Role of Nucleation Entropy in Grain Refinement of Aluminum Alloys

The effect of third element additions on the grain refinement of Al by Ti has been investigated by Youdelis and coworkers(65-67). In the case of Si(65), Ge(66), Be(67) additions, it was found that the addition of small amounts of these elements (~0.2%) greatly enhanced grain refinement of Al by Ti. The Si-enhanced grain refinement effect in Al-Ti can be attributed to a constitutional and a kinetic effect of Si on the Al-Ti system. Youdelis(68) has shown that the addition of Si extends the range of the peritectic-like reaction to lower Ti concentrations, and a 3-phase mono-variant region forms in which the peritectic-like reaction occurs over a temperature interval. These two constitutional effects increase the peritectic reaction and thereby grain refinement. In calculating the ternary phase diagram (Kaufman method), it was assumed that there are no intermediate ternary compounds present which would influence the Al corner of the Al-Ti-Si system; however, the presence of the ternary compound $TiAl_{2.4}Si_{0.6}$ in the Al-Ti-Si system reported by Ramon and Schubert(69) and confirmed by Yang(67), and the probability that the compound will undergo the peritectic reaction to form Al crystals, introduces a kinetic factor which must be considered in the grain refinement mechanism. Although the peritectic reaction is generally accepted to be a principal factor in the grain refinement of Al by Ti(70), it is a secondary stage and first requires the nucleation of the primary $TiAl_3$ crystals.

Youdelis(64) has developed a method for determining the nucleation entropy of intermediate compounds of phases of limited solubility when the formation entropy is known, and has shown that the nucleation entropy for $TiAl_{2.4}Si_{0.6}$ is substantially higher than for $TiAl_3$, and that the nucleation rate (a result of the exponential dependency on the square of the nucleation entropy) for the ternary compound is several orders of magnitude higher than for the binary compound. Thus

Si enhancement in grain refinement of Al by Ti could be attributed to a kinetic as well as a constitutional effect, and it is probable that both effects are operative. It would be difficult to determine the relative importance of each factor from the above grain refinement results. However, the rapid increase in the nucleation rate with small increases in the nucleation entropy indicates that the kinetic effect may be predominant.

(c) The Role of Nucleation Entropy in the Refinement of Carbides

In an investigation on carbide refinement in superalloys, it was shown that the addition of Ta or Nb significantly refined the primary carbides in the Co-base alloy (HS21)(71), but had virtually no effect on the primary carbides in the Ni-base alloy (713C)(72). The results for both superalloys are consistent with the proposed nucleation entropy theory for structure refinement. The primary carbides in the Co-base alloy were determined to be $M_{23}C_6$ type having the approximate stoichiometric formula $(Cr_{0.77}Co_{0.15}Mo_{0.08})_{23}C_6$(71). Increasing the Ta or Nb content in the alloy progressively transformed the carbides to MC type, and for Ta or Nb contents exceeding ~1%, the transformation to fine and numerous TaC or NbC carbides was essentially complete. The considerably finer and more numerous carbide particles in the HS-alloys containing Ta and Nb is in agreement with the higher calculated nucleation entropies and rates for MC vs. the $M_{23}C_6$ type carbides.

For the Ni-base superalloy (713C), the primary carbides were determined to be MC type having the approximate composition $(Nb_{0.77}Ti_{0.23})C^{(72)}$. The addition of Ta or Nb to the alloy resulted in the incorporation of Ta or Nb into the carbides mostly at the expense of Ti, but the carbide type was not changed. No significant refinement of carbides occurred on Ta and Nb additions to 713C alloy, which is in agreement with the absence of any significant differences in the nucleation entropies.

D. ISOTHERMAL TRANSFORMATIONS IN SOLID STATE

Transformation in the solid state proceeds by nucleation and growth until impingement occurs with the neighbouring transformed regions. The mutual impingement restricts the growth and has to be considered in derivation of a kinetic law for the transformation process. The problem was first treated by Johnson and Mehl(73) and by Avrami(74), for the case of recrystallization where no diffusion is required, by introducing the concept of the extended volume. For the case of a constant nucleation rate ($\dot{N}$) and constant isotropic growth rate (Y) in three dimensions, the volume fraction transformed (ξ) is given by:

$$\xi = 1 - \exp[-\pi Y^3 \dot{N} t^{4/3}] \qquad (15)$$

Avrami has considered the more general case when $\dot{N}$ is not constant, and nucleation occurs on preferred sites which are exhausted according to a first order rate law. If the nucleation sites are exhausted at an early stage in the reaction, i.e., nucleation is fast and not rate controlling,

$$\xi = 1 - \exp[(\frac{-4\pi\bar{N}}{3})Y^3t^3] \qquad (16)$$

where $\bar{N}$ is the initial density of nucleation sites. In general,

$$\xi = 1 - \exp(-kt^n) \qquad (17)$$

(referred to in this text as the Avrami equation) where the parameters "k" and "n" are determined by the nucleation and growth mechanism for the transformation (Christian(75)).

Wert and Zener(76) derived an expression for the volume transformed in which the growth is diffusion controlled and the diffusion fields of adjacent particles overlap (termed soft impingement). Assuming that the interface of a spherical particle grows sufficiently slow to give a steady state approximation for the concentration gradient, Wert and Zener also obtain the Avrami type expression with n = 3/2. For a plate-like precipitate with diffusion controlled thickening and a linear radial growth n = 5/2(77).

Ham(78) has treated the soft impingement problem using a cubic array for the precipitate particle distribution. For spheres Ham also obtained n = 3/2 for short times, but for longer times of precipitation n=1. Ham assumes that growth conditions at the edge of a disc are not constant as assumed by Wert and Zener, and obtains for disc of constant aspect ratio n = 3/2 (each dimension varies as $\sqrt{t}$) for the initial stages, but n = 1 for the latter stages of the transformation. For a disc of constant thickness, and assuming an initial linear growth rate, Ham(79) obtains n=2, which for longer times again decreases to n=1.

Cottrell and Bilby$^{(80)}$, derived an equation for solute precipitation on an edge dislocation, assuming that the diffusion current is the result of interaction potential only. The fraction of solute precipitated is given by:

$$\xi = 2L(\tfrac{1}{2}\pi)^{1/3}(ADt/kT)^{2/3} \qquad (18)$$

where L is the length of dislocations per unit volume and A and D are interaction energy and diffusion constants respectively. Harper$^{(81)}$ proposed that the competition between dislocations can be treated using the Avrami method for impingement, and derives:

$$\xi = 1 - \exp[-2L(\tfrac{1}{2}\pi)^{1/3}(ADt/kT)^{3/3}] \qquad (19)$$

Ham$^{(82)}$ has criticized the neglect of solute current due to concentration gradients in Cottrell and Bilby and Harper treatments. By comparing calculations assuming impingement factor $(1-\xi)$ used by Harper, to the calculations in which diffusion transfport is treated rigorously, Ham has shown that Harper's equation underestimates the precipitation at longer times and proposes the kinetic equation,

$$\xi = 1 - \exp(-\lambda_0^2 Dt) \qquad (20)$$

where λ_0 is a constant related to the dislocation density. The Harper equation can be used only as an approximation for very short times of the precipitation, or in the case that solute distribution during the precipitation can be represented by a steady state equation normalized far from the particle to the instantaneous value of the average density.

E. STRAIN ENERGY IN SOLID→SOLID TRANSFORMATIONS

Transformations in the solid state are usually accompanied by volume changes that result in elastic strain which must be included in the calculation of the free energy of nucleation of the critical-sized nucleus ΔG^*. Two general cases must be considered:

(a) incoherent nucleation where there is no lattice continuity between the precipitate and matrix, and the strain is hydrostatic in character, and

(b) coherent nucleation in which the lattices of the precipitate and the surrounding matrix are constrained to match, and the strain is determined by the degree of mismatch of the lattices.

The two cases are discussed below:

(1) Incoherent Precipitate

The theoretical basis of elastic energy calculations in the case of incoherent nucleus is the misfitting sphere model (Christian$^{(13)}$). A single atom B with radius $r_B = (1+\varepsilon)r_A$ is introduced into infinite lattice of A atoms with atomic radius r_A. Using equilibrium equations of elasticity and the appropriate boundary conditions the displacements are found, the stress and the strain fields defined and elastic energy calculated. The total elastic energy (W_T) of atom B and the surrounding matrix is:

$$W_T = 2\mu_A C_6 (v_B - v_A)^2 / 3v_B \tag{21}$$

where μ_A, v_A and v_B are the shear modulus of matrix and the atomic volume of A and B respectively. The C_6 parameter is a measure of partition of the elastic energy between matrix and precipitate and is given by:

$$C_6 = K_B/(3K_B + 4\mu_A) \tag{22}$$

where K_B is the bulk modulus of B. Assumptions inherent in eqn. (21) are that only shear strains are present in the matrix$^{(83)}$ and that the finite size of the matrix does not alter significantly the results obtained for the infinite medium.

The effect of shape of the nucleus was analyzed by Nabarro$^{(84)}$ who proposed a general equation:

$$W_T = \{2\mu_A C_6 (v_B - v_A)^2/3v_B\} E(\frac{c}{r}) \tag{23}$$

where E is a function of the semi-minor and semi-major axes c and r of an ellipsoid and is shown in Figure (1).

(2) Coherent Precipitate

The general treatment for homogeneous (matrix and precipitate are assumed to have the same elastic constants) and isotropic transformation has been given by Eshelby$^{(85)}$. The procedure involves several imaginary steps:

(i) A small volume from the centre of matrix (α) is removed and allowed to undergo an unconstrained transformation to β.

(ii) Surface traction is applied to β particle to restore its original size and shape, and the particle is inserted in the hole.

(iii) α and β regions are welded together over their

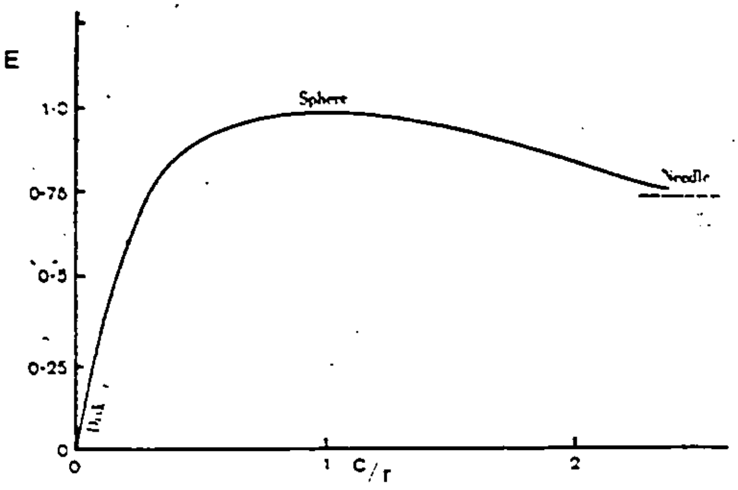

Figure 1 E, the normalized elastic energy of ellipsoid as a function of (c/r); a is the major and c the minor semiaxes.

surface of contact.

(iv) The built-in surface layer of force is removed by applying an equal and opposite layer of force.'

The free transformation α→β in step (i) is characterized by the strain tensor ℓ_{ij}^{T}. Using Hooke's law, the stress applied X_{ij}^{T} in step (ii) is given by:

$$X_{ij}^{T} = \lambda \, \Delta^{T} \delta_{ij} + 2\mu \ell_{ij}^{T} \qquad (24)$$

where Δ^{T} is the fractional volumetric change for the free transformation and is given by:

$$\Delta^{T} = \varepsilon_{11} + \varepsilon_{22} + \varepsilon_{33} \qquad (25)$$

where ε_{ii} are the principal strains.

δ_{ij} is the Kronecker delta given by:

$$\delta_{ij} = \begin{cases} 1 & i = j \\ 0 & i \neq j \end{cases} \qquad (26)$$

and λ is the Lame constant given by:

$$\lambda = \nu E/(1+\nu)(1-2\nu) \qquad (27)$$

where ν and E are Poisson's ratio and Young's modulus, respectively.

In step (iii) the matrix is still stress and strain free whereas in step (iv) the applied stress X_{ij}^{T} produces strain field ℓ_{ij}^{c} in the matrix and is the actual strain field created by the α→β transformation.

Eshelby has shown that the total strain energy in the matrix and the precipitate is:

$$W_{T} = -\tfrac{1}{2} \int_{v} X_{ij}^{I} \ell_{ij}^{T} dv \qquad (28)$$

where v is the volume of precipitate and X_{ij}^{I} is given by:

$$X_{ij}^{I} = X_{ij}^{C} - X_{ij}^{T} \qquad (29)$$

where X_{ij}^{C} is the final stress field in matrix and is obtained using eqn. (24) with Δ^{C} and ℓ_{ij}^{C}, the fractional volumetric change and the strain field for constrained transformation. Eqn. (28) can be solved for a precipitate of ellipsoidal shape and for the simple case of pure and uniform dilatation, the strain energy is:

$$W_T = \frac{2}{9}\,\frac{1+\nu}{1-\nu}\,\mu(\Delta^{T})^{2}v_B \qquad (30)$$

The restriction to ellipsoidal shape was removed by Khachaturyan(86), who reformulated the Eshelby's treatment and found a Fourier transform solution for an arbitrary shape of coherent precipitate. The method is applicable for the anisotropic case, but requires homogeneous elastic properties. Minimum strain energy criteria was applied to determine the optimum shape and orientation assuming nonsignificant contribution of the surface energy. A simplified Khachaturyan solution was used by Wert(87) to calculate strain energies of disc-shaped precipitate in various metals as a function of the orientation and the elastic energy of GP zones was estimated to be 8.6 cal per mole of alloy.

N. Kinoshita and T. Mura(87a) extended Eshelby's treatment and expressed the stress and strain fields in terms of series and integral which allows to treat anisotropic cases of general shape. Barnett et al(88) applied Eshelby method to a non-homogeneous case but maintained the isotropic restriction and assumed that transformation proceeds by pure dilatation. Calculations of strain energy W normalized to W_o, the strain energy for isotropic and homogeneous transformation, were carried out as a function of $\beta(=\frac{c}{r})$. Three cases were considered: $\mu^* = \mu$, $\mu^* = 3\mu$ and $\mu^* = \frac{1}{3}\mu$ where μ^* and μ are the shear modulus of precipitate and matrix respectively. Spherical morphology was found to result in minimum strain energy for $\mu^*>\mu$ and in maximum energy in the reverse case. Lee et al (89) extended the work of Barnett (88) and examined the effect of orientation on W/W_o. The elastic energy was found to be sensitive to the precipitate/matrix orientation in particular if only small differences in elastic constants between matrix and precipitate exist, the significance of orientation increases for lower symmetry. For precipitation of Cu in Al matrix, Lee et al consider several possible orientations (Table 1) and calculate the corresponding strain energy ratios, W/W_o (Figure 2). Minimum strain energy is obtained for a disc morphology when the cubic directions of precipitate and matrix are parallel (orientation No. 1 in Table 1), and is in agreement with the experimentally observed orientation of disc-like GP zones in Al-4%Cu alloy.

The inclusion of W in the free energy of formation of disc-shaped, incoherent particle of semi-thickness c and radius r gives for c<<r:

$$\Delta G = \frac{4}{3}\pi r^2 c\Delta G_V + 2\pi r^2\gamma + \frac{4}{3}\pi r^2 cW \qquad (31)$$

Minimizing with respect to r and c gives (90) (for $\Delta G \sim -\Delta S\Delta T$):

$$\Delta G^* = \frac{32\pi}{3} W^2\gamma/(\Delta S\Delta T)^4 \qquad (32)$$

Lee et al (83) obtained for the more general case (anisotropic, inhomogeneous) of a coherent ellipsoidal nucleus:

$$\Delta G = \frac{4}{3}\pi r^3\beta[\Delta G_V + W] + \pi r^2\gamma[2+g(\beta)] \qquad (33)$$

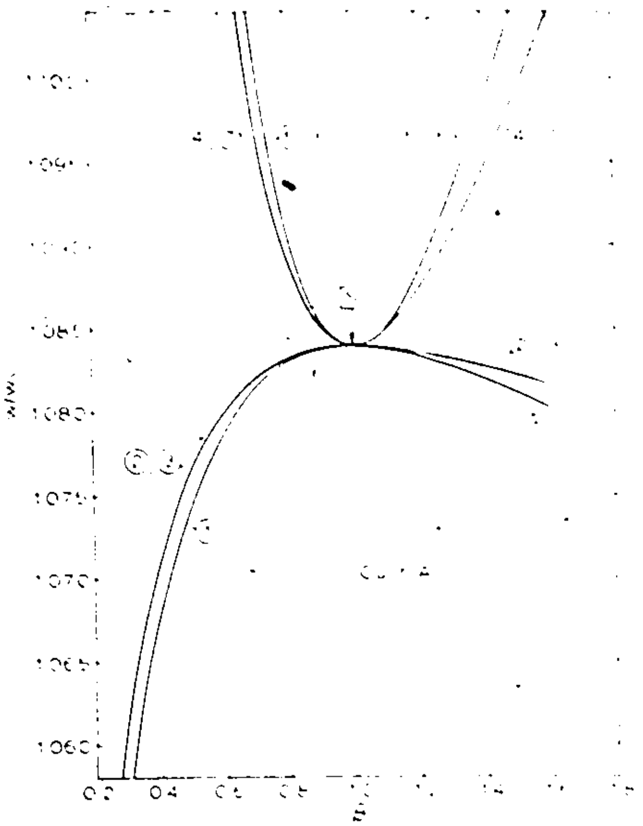

Figure 2 Normalized strain energy of a Cu precipitate in an Al matrix vs. aspect ratio for different orientations. Each number indicates an orientation relationship listed in Table 1. The S denotes a spherical precipitate (after Lee et al[88]).

Table 1

Orientation Relationships Examined (after Lee et al(88).)

Number	Ellipsoid Axes			Remarks
	a	b	c	
1	$[100]_m[100]_i$	$[010]_m[010]_i$	$[001]_m[001]_i$	(111)/(0001)
2	$[\bar{1}01]_m[100]_i$	$[1\bar{2}1]_m[010]_i$	$[111]_m[001]_i$	
3	$[1\bar{2}1]_m[0\bar{1}0]_i$	$[111]_m[001]_i$	$[\bar{1}01]_m[100]_i$	
4	$[\bar{1}01]_m[111]_i$	$[1\bar{2}1]_m[\bar{1}01]_i$	$[111]_m[1\bar{2}1]_i$	
5	$[1\bar{2}1]_m[\bar{1}01]_i$	$[111]_m[1\bar{2}1]_i$	$[\bar{1}01]_m[111]_i$	
6	$[\bar{1}01]_m[\bar{1}01]_i$	$[1\bar{2}1]_m[1\bar{2}1]_i$	$[111]_m[111]_i$	
7	$[\bar{1}01]_m[\bar{3}32]_i$	$[1\bar{2}1]_m[1\bar{1}3]_i$	$[111]_m[110]_i$	Nishiyama O.R.

m = matrix phase.

i = ellipsoid precipitate phase.

where $\beta = \frac{c}{r}$, the ratio of semi-minor (c) and semi-major (r) axes of the ellipsoid. The function $g(\beta)$ is given by:

$$g(\beta) = \begin{cases} \dfrac{2\beta^2}{\sqrt{1-\beta^2}} \tanh^{-1}(\sqrt{1-\beta^2}) & \text{when } \beta < 1 \\ 2 & \text{when } \beta = 1 \\ \dfrac{2\beta}{\sqrt{1-\beta^{-2}}} \sin^{-1}(\sqrt{1-\beta^{-2}}) & \text{when } \beta > 1 \end{cases} \tag{34}$$

Minimizing with respect to r and β gives:

$$\Delta G^* = \frac{\pi\sigma^3[2+g(\beta^*)]^3}{12(\beta^*)^2(\Delta G_v+W)^2} \tag{35}$$

where β^* is determined numerically. Calculations of ΔG^* show that the critical shape, for strain energies smaller than $W \sim 0.8\Delta G_v$, is spherical. The resulting ΔG^* is obtained by substituting $\beta=1$ and $g(\beta) = 2$ into eqn. (32), giving (for $\Delta G_v \sim -\Delta S\Delta T$):

$$\Delta G^* = \frac{16\pi}{3} \frac{\sigma^3}{(-\Delta S\Delta T+W)^2} \tag{36}$$

CHAPTER III

EXPERIMENTAL

To assist the reader through the various stages of the investigation, a flow-chart, summarizing the experimental procedure is given in Figure 3.

A. ALLOY PREPARATION

The appropriate amounts of superpurity Al (4N grade), electrical conductivity grade Cu (99.99%), and Al-5.23%Be master alloy were used in preparing the binary and ternary alloys. The Al was supplied by the Aluminum Company of Canada and the Al-5.23%Be master alloy by Kawecki Berylco Industries. The Al-3%Cu and Al-3%Cu-0.1%Be alloys were prepared in graphite crucibles, by induction melting in air, using a 15 KVA Ajax Inductotherm unit at a frequency of 10 kilohertz. The melts were heated to 750°C, well above liquidus, kept at this temperature for 5 minutes to ensure complete homogenization, stirred and poured into the graphite molds ~25 mm dia. x 60 mm length at room temperature. The temperature of the melt was measured by an occasional immersion of a chromel-alumel thermocouple, and also by constantly monitoring a thermocouple embedded in the graphite mold. The subsequent experimental work was carried out on the central parts of ingots to ensure similar initial microstructures and compositions.

Cold working as a supplementary homogenization procedure was omitted in this investigation, for it can be assumed that the work hardening rates of the Al-Cu and Al-Cu-Be alloys

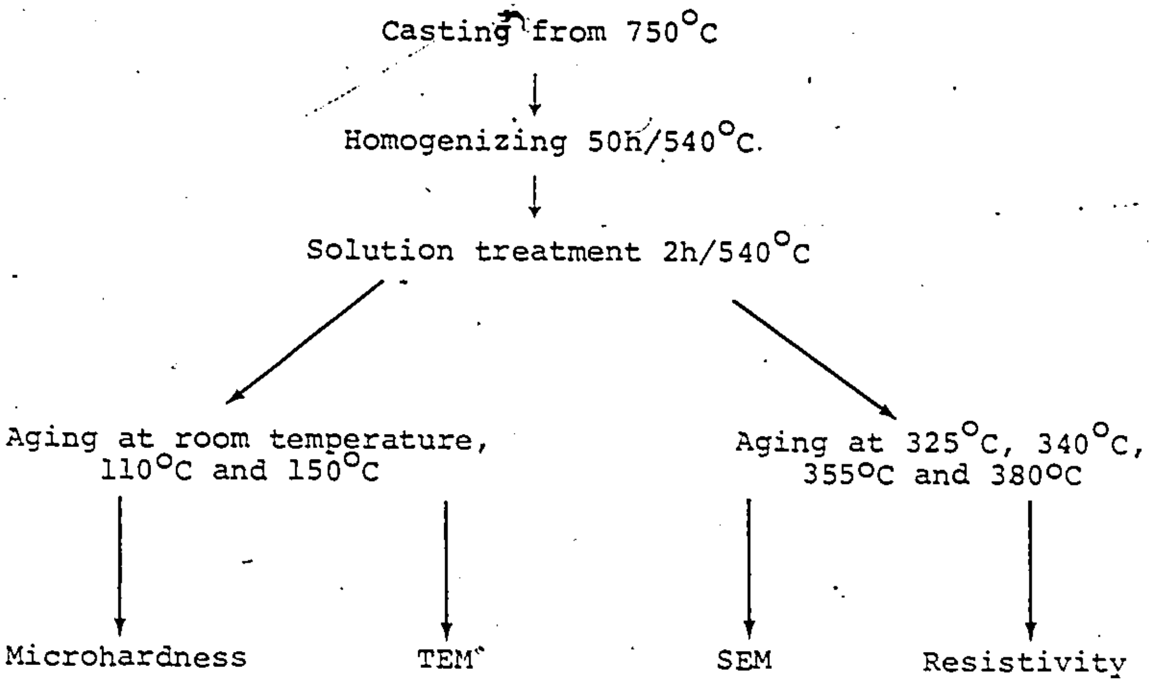

Figure 3 Flow chart for the experimental procedure.

would differ to give dissimilar dislocation densities. The (potential) nucleation site concentrations would thereby differ, and thus tend to obscure the nucleation entropy role in the subsequent aging experiments.

Optical micrographs of the as-cast alloys (Figure 4) show secondary phases in both alloys assumed to be the θ in Al-3%Cu alloy and θ phase plus Be particles in the Al-3%Cu-0.1%Be alloy. The as-cast alloys were annealed for 50 h at 540°C for homogenization. Complete dissolution of θ phase was observed in Al-3%Cu alloy (Figure 5(a)), whereas in the Al-3%Cu-0.1%Be alloy, an insoluble phase remained (Figure 5(b)), later determined to have the approximate composition of Al_4Cu_9 containing some Be. An additional homogenization for 170 h at 540°C did not significantly diminish the secondary phase, which can be assumed thermodynamically stable at and below 540°C.

To estimate the amount of Be that can be dissolved in the Al_2Cu phase and the effect on the crystal structure, Al-53%Cu and Al-53%Cu-2.7%Be alloys were induction melted under vacuum. The melts were kept at 900°C for 10 minutes to assure liquid homogenization, and then furnace cooled under Argon. These alloys were subjected to spectroscopic (energy dispersive) and X-ray diffraction analyses. A supplementary metallographic analysis, to determine Be content in θ phase, was also performed. Eutectic alloys (Al-35%Cu) with 0, 0.14, 0.3 and 0.5%Be were induction melted under vacuum, and the melt temperatures raised to 1100°C for liquid homogenization before furnace cooling under vacuum.

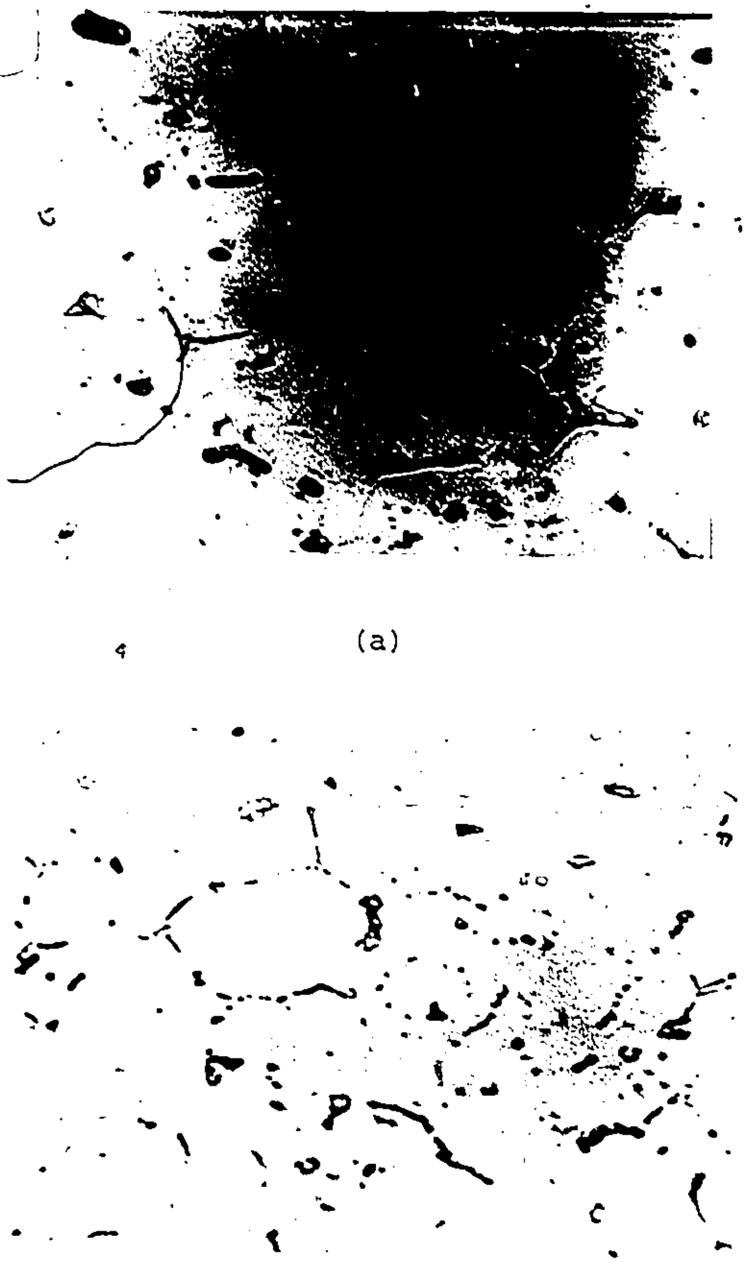

(a)

(b)

Figure 4 As-cast microstructures, x500: (a) Al-3%Cu alloy; (b) Al-3%Cu-0.1%Be alloy.

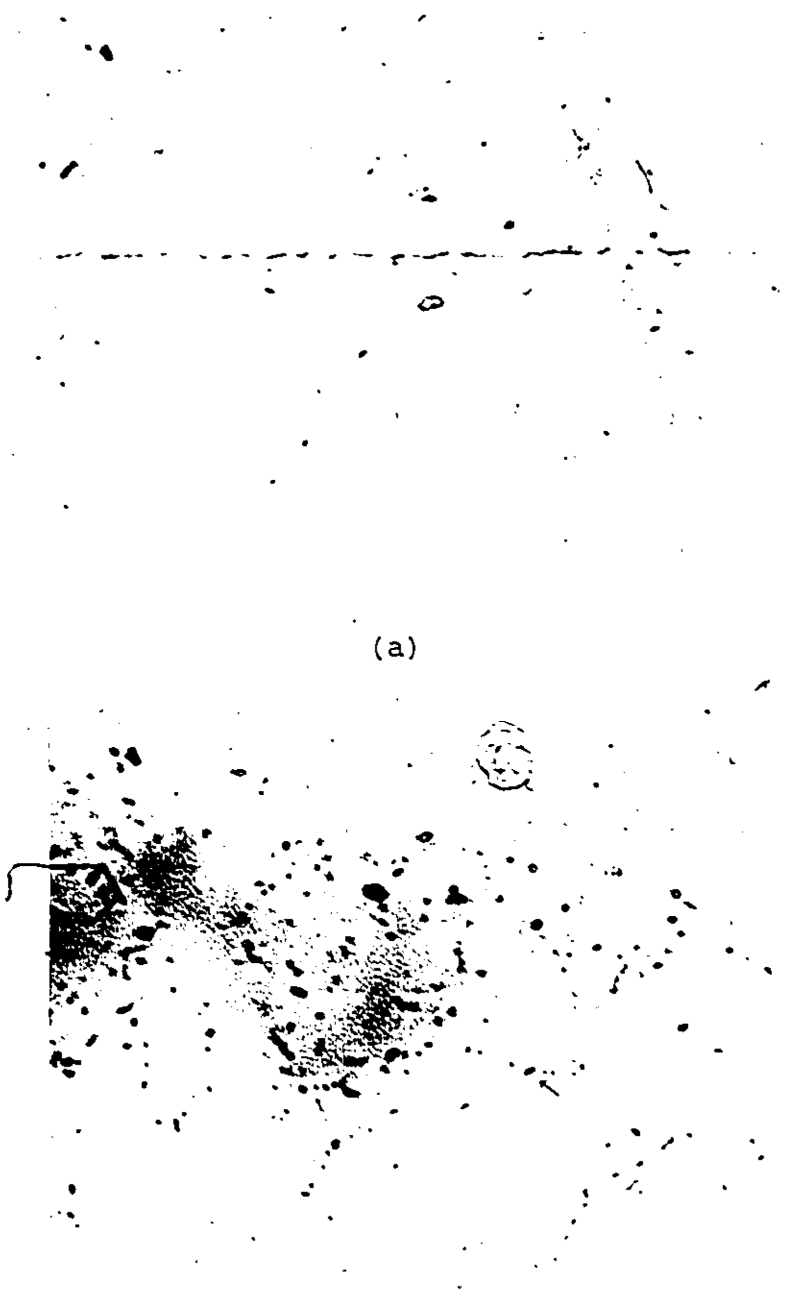

(a)

(b)

Figure 5 Homogenized microstructures, x500: (a) Al-3%Cu alloy; (b) Al-3%Cu-0.1%Be alloy. Note the insoluble particles (arrowed) in (b).

Samples from the cast ingots were analyzed spectroscopically for Cu and Be content by Detroit Testing Laboratories (DTL), and the results indicated little or no loss of Cu and Be in alloy preparation.

B. SOLUTION TREATMENT AND AGING

The solution treatment for all samples consisted of an additional 2 hour anneal at 540°C, followed by a water quench. For the investigation of clustering and GP zone formation, the samples were aged at room temperature at 110°C and at 150°C in an electric furnace (Lindberg) with the temperature controlled to ±1°C. The decomposition of the Al-3%Cu-0.1%Be and Al-3%Cu alloys was monitored by microhardness measurements. Thin foils were prepared for TEM studies from samples aged at 110°C for 530 h (corresponds to the hardness plateau) and from samples aged an additional 15 hours at 150°C. The additional aging treatment was required to activate the GP zone formation in Al-Cu-Be alloy.

For investigation of the θ' and θ precipitation, the samples were solution treated for 2 hours at 540°C, quenched in water and ice, and aged between 325°C-380°C. The resistivity technique, well established and frequently used for studying precipitation kinetics in alloys (e.g., (91)) was employed and supplemented by TEM study.

C. ANALYTICAL PROCEDURE

(1) Microhardness Analysis

For microhardness analysis, the aged samples were polished to 1μ finish using a conventional polishing technique. Leitz and Wetzlar microhardness tester was used with a diamond Vicker indentor, and loads of 100-200 gm. At least five readings were taken at random points on the specimen for each hardness determination to provide a statistical basis for the calculated mean hardness values.

(2) Optical Microscope, SEM, EDS and TEM Analyses

For optical microscopy, conventionally polished samples were given a final polish with a colloidal silica suspension (Buehler) and etched with Keller solution. For the scanning electron microscope (SEM) and energy dispersive (EDS) analyses, a progressive etch was carried out, sufficient to create a topographic contrast, yet mild enough to prevent etching out of the precipitates. "Nanolab 7" SEM, with a resolution of 700 nm and maximum useful magnification of x10,000, was used in the secondary electron imaging mode at 15kV (no constrast was obtained with backscattered electrons).

The EDS analysis was performed on a Kevex 5100 spectrometer coupled to the SEM. The National Bureau of Standards computer program (Frame B) was used with standards of pure Al, Cu ~~and~~ with Al_2Cu. The take-off angle was taken as 30°, and the accelerating potential was 15kV. A minimum of three countings or more were taken from each phase at different areas of the sample.

For the transmission electron microscope (TEM) analysis, 1 mm thin sections were cut from cylindrical samples using a low speed saw (Buehler). The sections were mechanically ground on 240 paper to a thickness of 0.2 mm. The final thinning was performed using a Fishione double jet electropolisher. Two electrolytes were used: 1) 10% glycerol, 10%

$HClO_4$, 80% ethanol and 2) 30%HNO_3, 70% methanol, (the latter producing cleaner thin foils), both maintained at -20°C to -30°C with a mixture of dry ice and alcohol. The thin foils were examined under the JEOL 100 CX TEM equipped with a double tilt holder, with 2A° resolution and operating at 100 kV. Most of the TEM work was done at <100> orientation verified by selected area diffraction pattern (SAD). Bright field, dark field and electron diffraction modes were employed.

(3) Resistivity Analysis

For the resistivity analysis, strips 0.1 mm thick, 4 mm wide and 72 mm long were cut from a cold rolled sheet of the alloy and the ends split (Figure 6) to provide current and voltage leads. The samples were stress annealed for 17 hours at 540°C prior to the aging treatments. The standard potentiometric method was employed with pure Al as the reference sample. The experimental set-up (Figure 7) consisted of a current regulated power supply (Spectromagnetic, average current drift ~0.03%), a Leeds and Northrup potentiometric facility capable of resolving 10^{-7}V, a Haake heat and circulating pump which maintained the temperature of the bath at ±0.01°C, and an Omega chart recorder.

(4) X-ray Diffraction

θ particles in Al-3%Cu-0.1%Be alloy aged 1 h at 380°C were extracted using the technique of F.H. Cocks et al(92). The procedure includes the dissolution of Al matrix in an electrolyte (8-hydroxy quinoline -5%, benzoic acid -20%, chloroform -20% and methanol -55%), using an Al cathode and a current density of 10 mA/cm^2. The extracted powder was

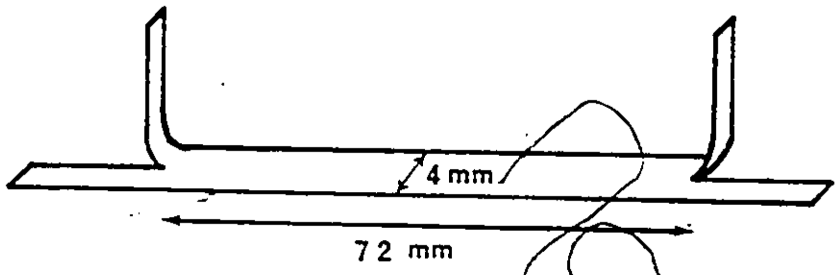

Figure 6 Resistivity sample.

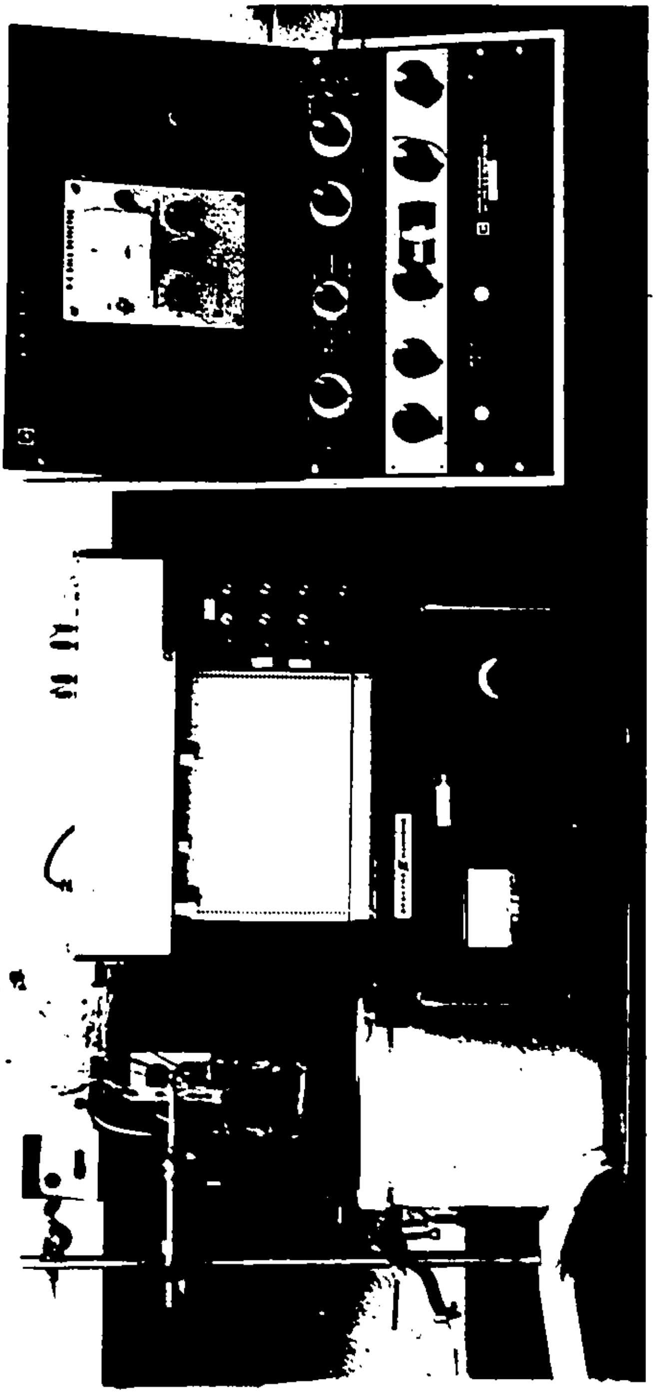

Figure 7 Experimental set-up for resistivity measurements.

separated from the electrolyte in a centrifuge, washed with methanol and dried in air, and analyzed by Debye-Scherrer technique with exposure time of ~1 hour. The diffractometer technique was used to examine powder samples of Al-53%Cu and Al-53%Cu-2.7%Be alloys. The alloys were crushed in a mortar, sieved to -300 mesh, and stress relieved for 17 hours at 150°C. CuK$_\alpha$ radiation (λ = 0.1542 nm) filtered by Ni, and a scanning rate of 0.5 2θ°/min. was used.

CHAPTER IV

RESULTS AND DISCUSSION

A. CLUSTERING AND GP ZONE FORMATION

(1) Hardness Measurements

Figure 8 gives the hardness vs. time for the Al-3%Cu, Al-3%Cu-0.1%Be and Al-0.2%Be alloys aged at room temperature. Each reading represents an average of five measurements with an experimental error of ±5%. For the Al-Cu alloy there is no significant change in hardness for the first 600 min. (here referred to as an incubation period) after which the hardness gradually increases from ~HV66 to ~HV90 after approximately 1200 min. For the Al-Cu-Be alloy, initially at a hardness HV70, the hardening starts as early as 15 min. after the quench. The initial hardening rate is relatively high during the first hour, reaching a hardness of ~HV103 after 9000 minutes. To determine if the independent precipitation of Be from the supersaturated alloy contributed to the aging process, an Al-0.2%Be alloy was subjected to an identical solution and aging treatment. The hardness remained relatively constant at ~HV21, and after 2400 min. increased to only ~HV25.

The hardening behaviour of the alloys was further investigated with aging treatments at 110°C (Figure 9) and 150°C (Figure 10). The Al-Cu alloy aged at 110°C exhibits an incubation period of approximately 450 min., following which the hardness increases from the initial value of ~HV64 to ~HV105 after 6300 min. For the Al-Cu-Be alloy aged at 110°C, hardening begins immediately with the start of the

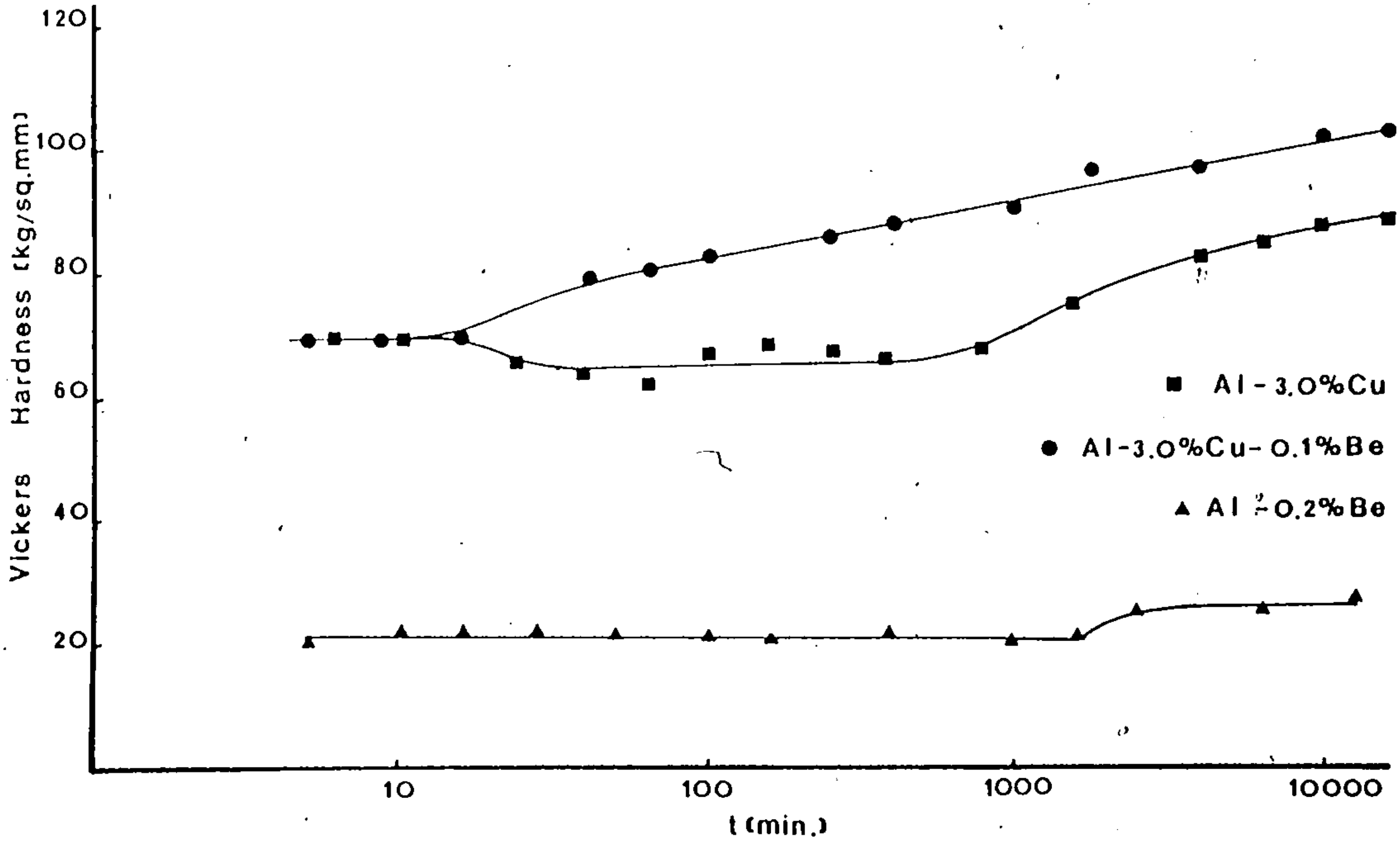

Figure 8 Hardness vs time for Al-3%Cu, Al-3%Cu-0.1%Be and Al-0.2%Be alloys aged at room temperature.

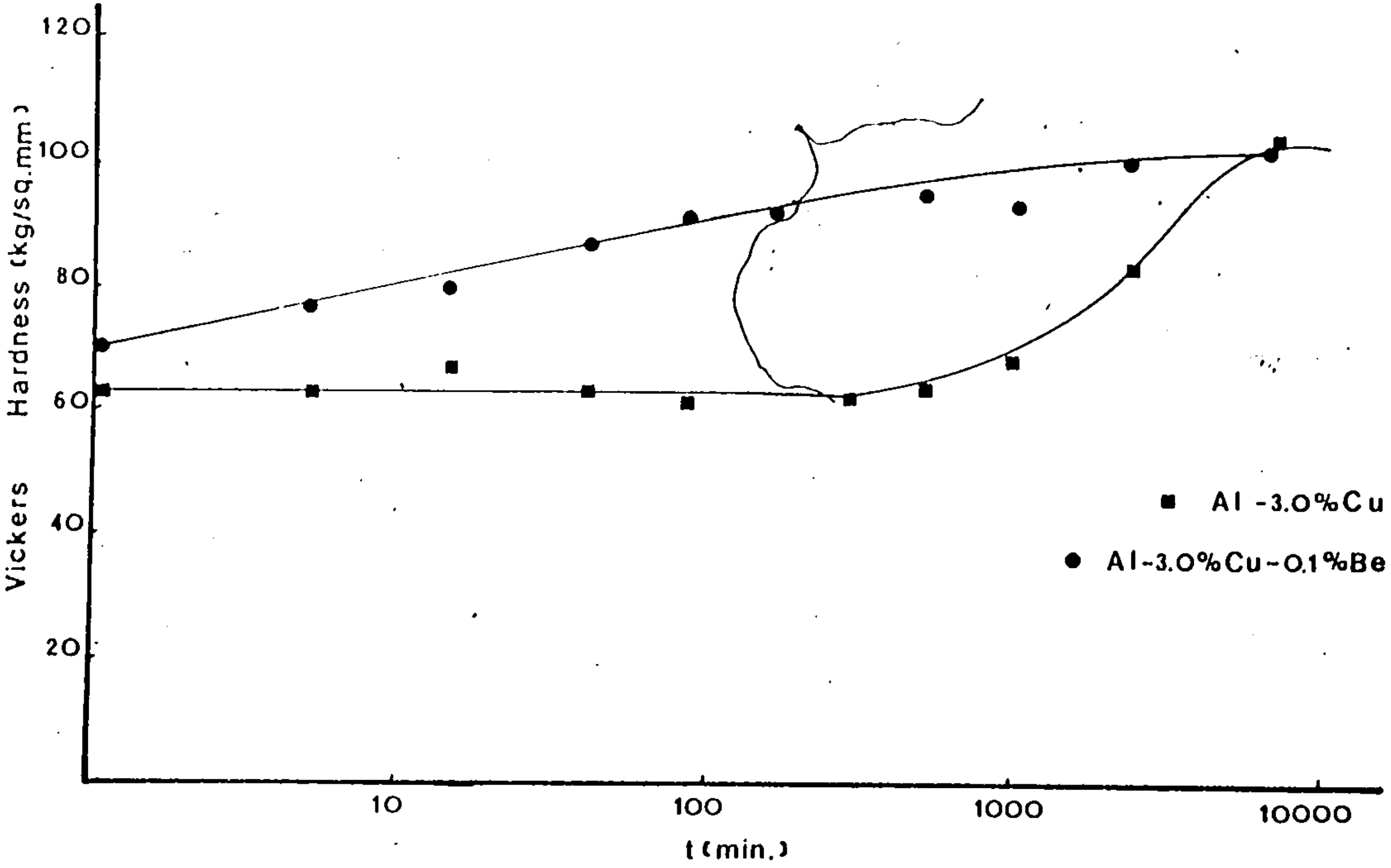

Figure 9 Hardness vs. time for Al-3%Cu and Al-3%Cu-0.1%Be alloys aged at 110^{o}C.

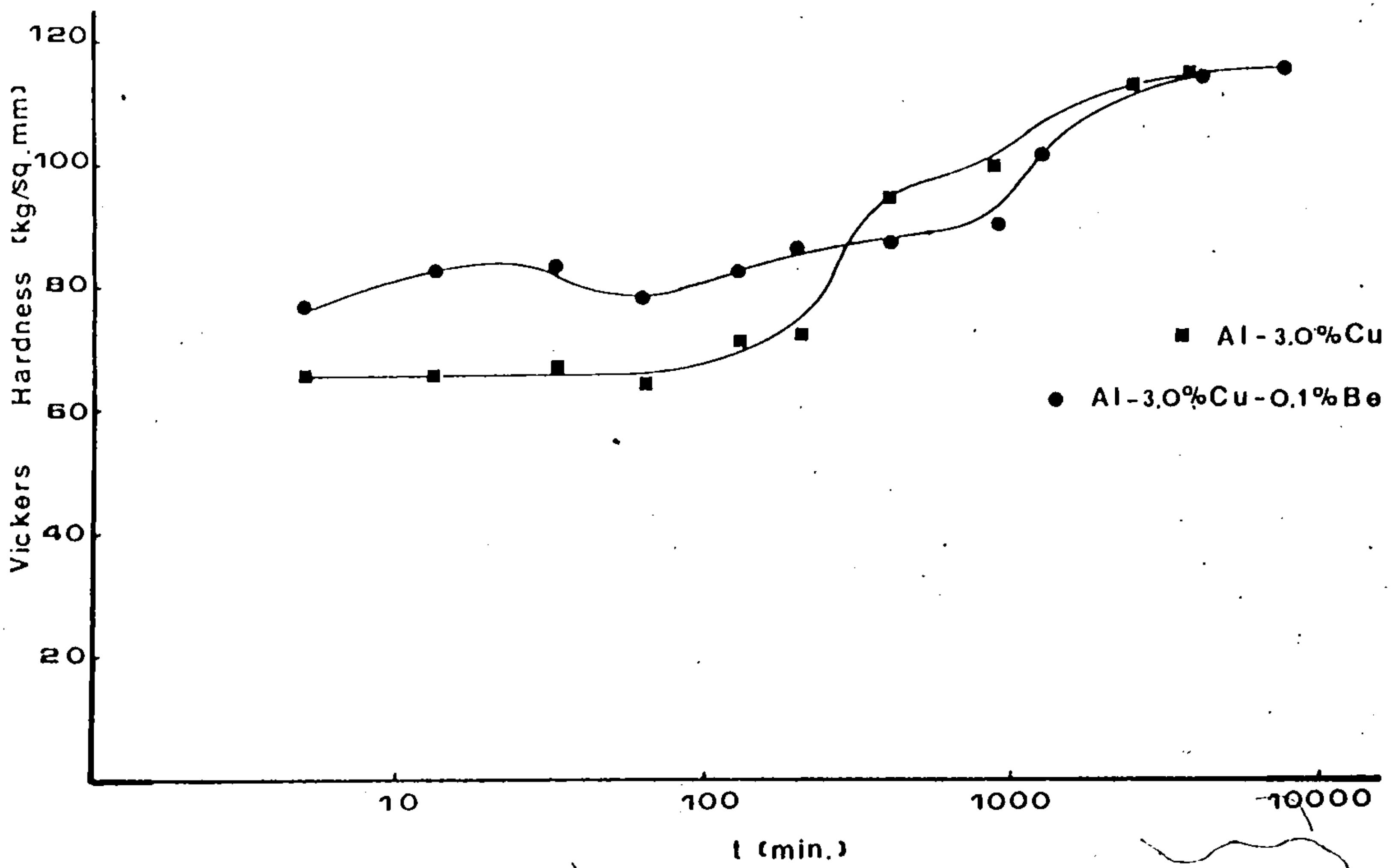

Figure 10 Hardness vs. time for Al-3%Cu and Al-3%Cu-0.1%Be alloys aged at 150°C.

aging cycle, the hardness increases from ~HV70 to ~HV103 after approximately 1440 min. For the aging treatment at 150°C, the Al-Cu alloy (initially at ~HV66) starts to harden after about 120 min. reaching the maximum hardness of ~HV115 after 4000 min. For the Al-Cu-Be alloy aged at 150°C, the initial higher hardness (~HV76) and rise indicates that hardening started immediately. The hardness varies, rising and falling slightly for the first 120 min. after which it increases to ~HV115. When Al-Cu-Be alloy is pre-aged at room temperature for several hours, a higher initial hardness followed by a larger temporary softening is observed (c.f., Figure 11).

(2) TEM Micrographs

Figure 12(a) shows the TEM micrograph and Figure 12(b) shows the corresponding electron diffraction pattern for the <100> orientation of the Al-3%Cu alloy aged at 110°C to the hardness plateau. The GP zones and the characteristic streaks in the diffraction pattern are readily evident. The bright field micrograph, Figure 13(a), and the corresponding electron diffraction, Figure 13(b), for Al-3%Cu-0.1%Be alloy aged at 110°C to the hardness plateau show that no GP zones are present at this stage. An additional aging treatment for the Al-3%Cu-0.1%Be alloy at 150°C for 15 hours was required for the GP zones to form (Figures 14(a),(b)). Dislocation loops were observed in both alloys aged to the hardness plateau (Figures 15,16); however, the loops in Al-3%Cu-0.1%Be (Figure 16) are larger and are closely related to the dis-

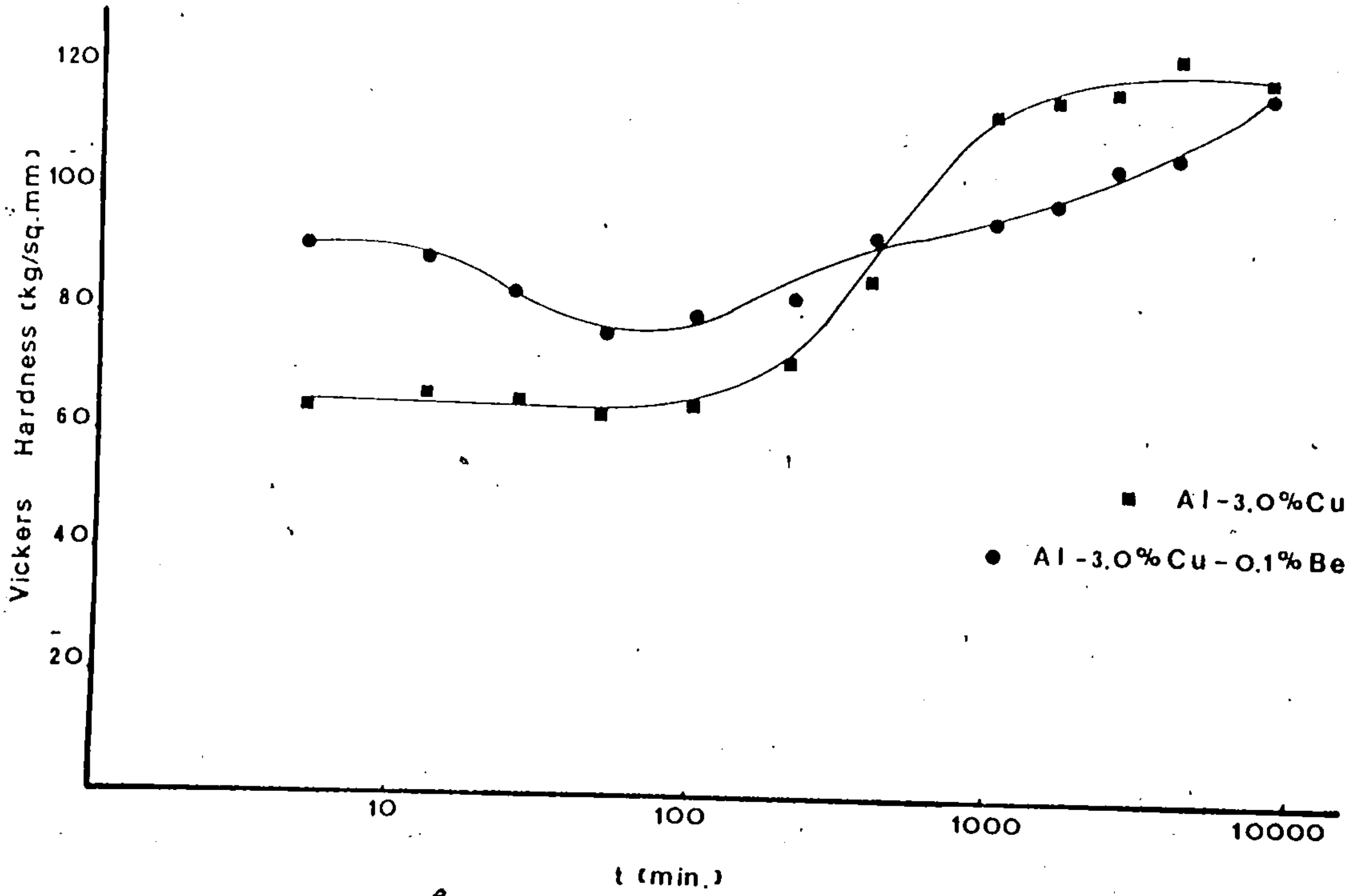

Figure 11 Hardness vs. time for Al-3%Cu and Al-3%Cu-0.1%Be alloys preaged 4 hours at room temperature, followed by aging treatment at 150°C.

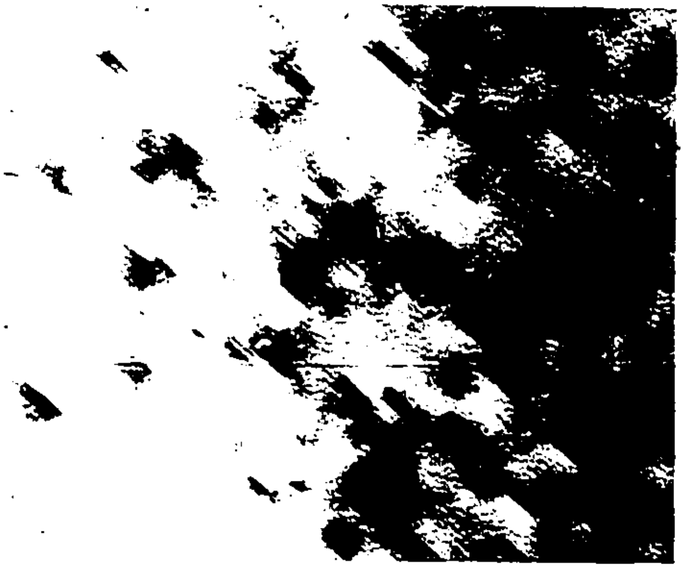

(a)

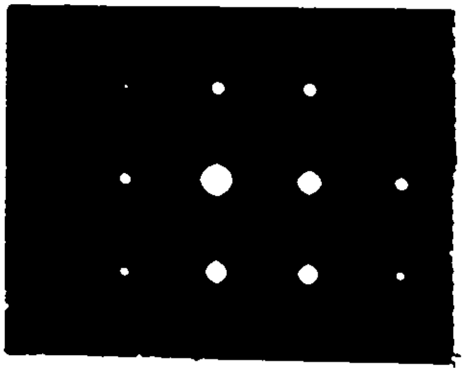

(b)

Figure 12 Al-3%Cu alloy aged 530h at 110°C (hardness plateau): (a) bright-field, ~<100> orientation, showing GP zones, x320,000; (b) electron diffraction pattern, ~<100> orientation.

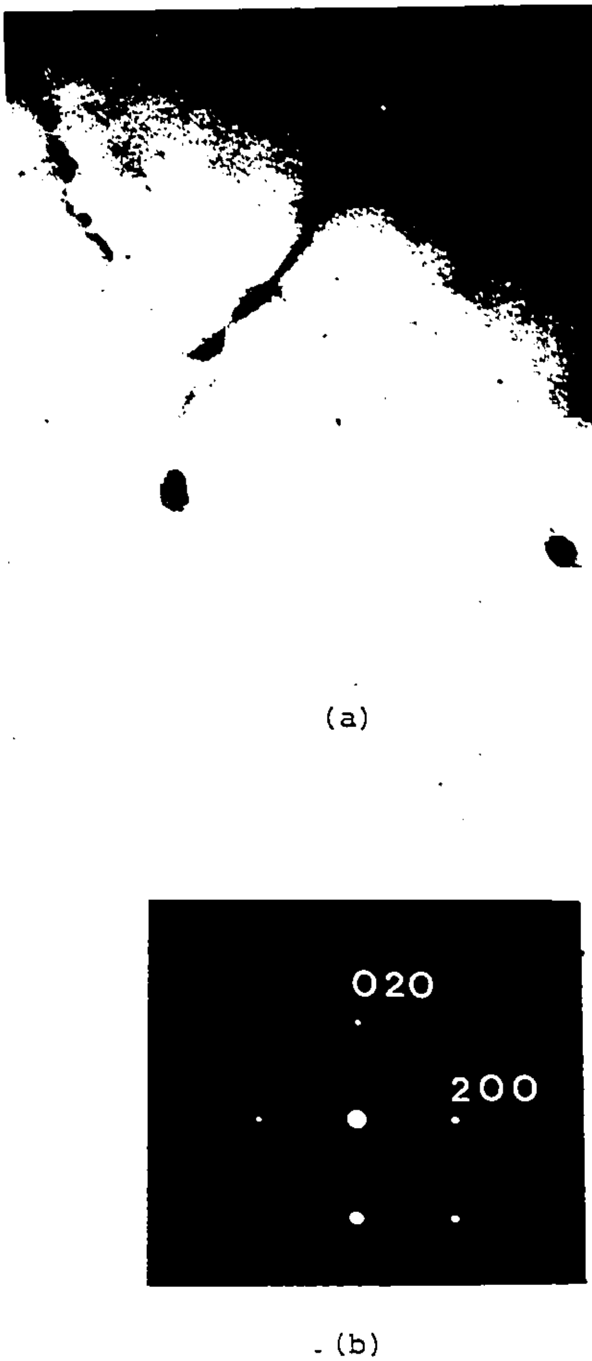

Figure 13 Al-3%Cu-0.1%Be alloy aged 530h at 110°C (hardness plateau): (a) bright field, ~<100> orientation, x 320,000; (b) electron diffraction pattern, ~<100> orientation.

(a)

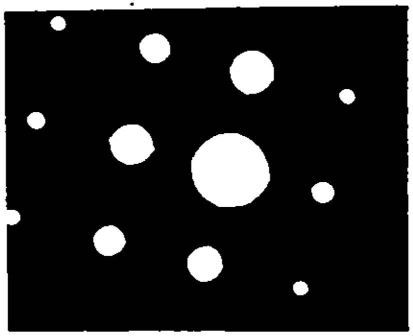

(b)

Figure 14 Al-3%Cu-0.1%Be alloy aged 530h at 110°C and additional 15h at 150°C: (a) GP zones ~<100> orientation, x 320,000; (b) electron diffraction pattern, ~<100> orientation.

Figure 15 Al-3%Cu alloy aged 530h at 110°C (hardness plateau) - dislocation loops, x160,000.

Figure 16 Al-3%Cu-0.1%Be alloy aged 530h at 110°C (hardness plateau): (a) and (b) edge-on orientation, at <011> pole; (c) and (d) "outside-inside" experiments around <101> pole.

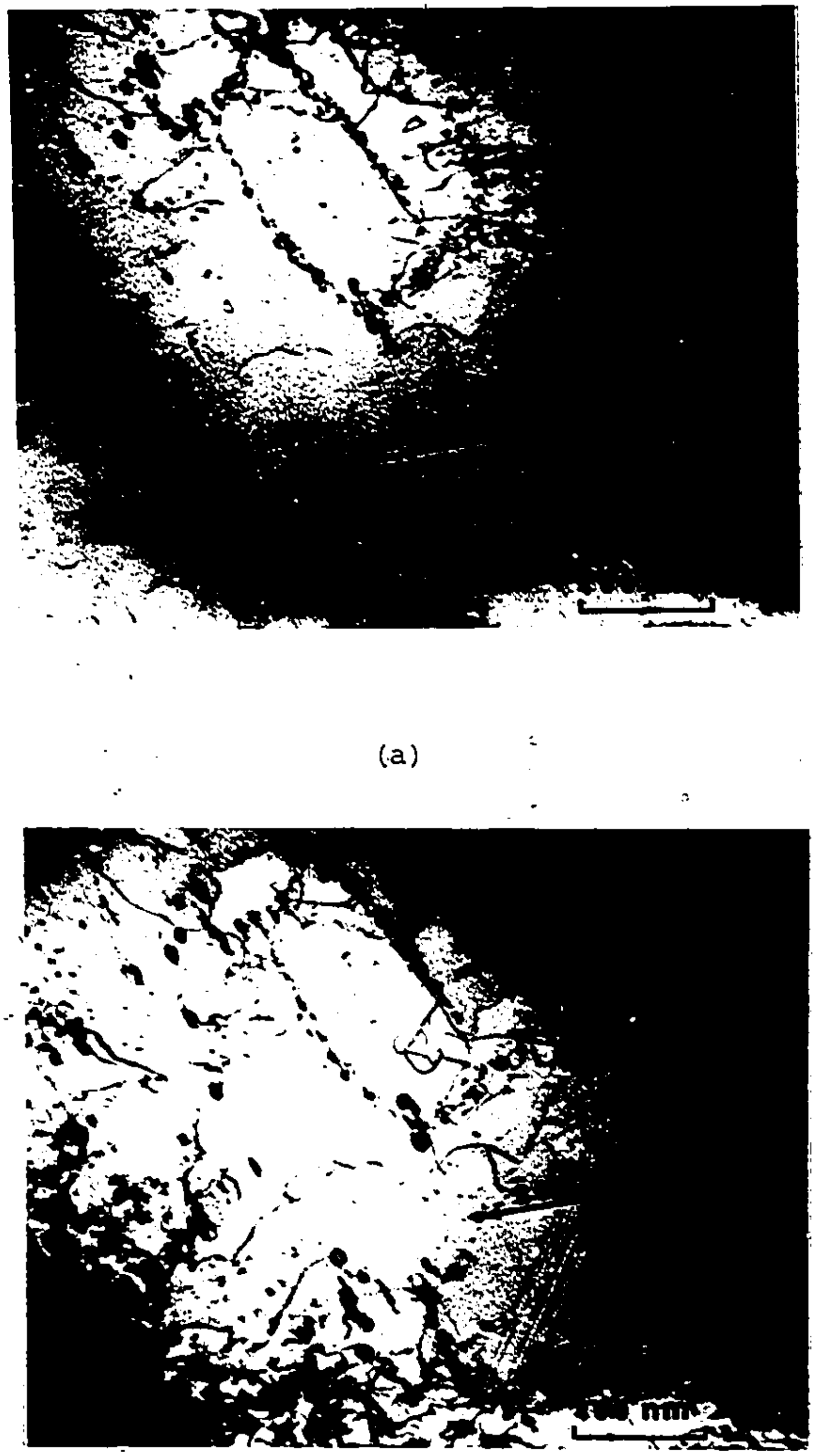

(a)

(b)

Figure 16 (cont'd).

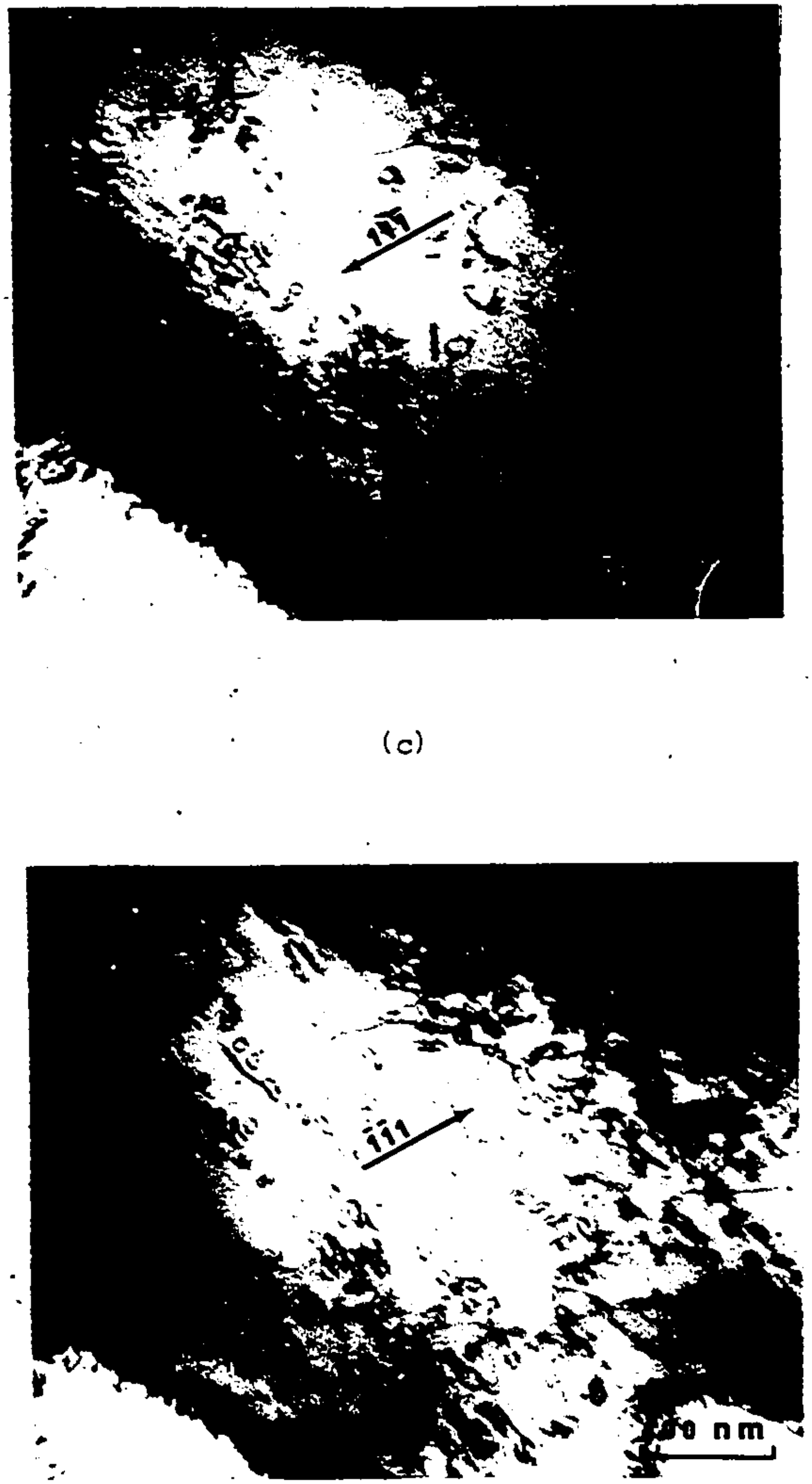

(c)

(d)

location lines. Figures 16(a) and (b) show an "edge-on" orientation of the loops in the Al-3%Cu-0.1%Be alloy which was ascertained using the diffraction vectors $\bar{g}=200$ (Figure 16(a)) and $\bar{g}=\bar{2}00$ (Figure 16(b)) at the 011 pole. The habit plane deduced from this analysis is (011) and the outside/inside contrast experiments with $\bar{g}=11\bar{1}$ and $\bar{g}=\bar{1}\bar{1}1$ around the 101 pole (Figures 16(c),16(d)), indicate that the loops are of a vacancy character. The Burgers vector obtained from $\bar{g}\cdot\bar{b}=0$ criteria is $\bar{b}=\frac{1}{2}<011>$.

(3) Discussion

It is evident from the above results that the rapid hardening of Al-Cu-Be alloy at room temperature and at 110°C is not due to an acceleration in GP zone formation, and that GP zone formation is in fact delayed. Nuyten(57) also reported a delay of GP zone formation in the Al-3.9%Cu-0.007%Be alloy. Contrary to the present results, a decrease in hardening was observed, suggesting that the amount of Be (0.1%Be as compared to 0.007%Be) plays an important role in the hardening process. Hardy(45), Hardy et al(46) and Silcock(47) reported GP1 and GP2 suppression in Al-Cu-(Sn, Cd,In) alloys, and a faster hardening rate between 110°C. 220°C was attributed to enhanced θ' formation. In the present study, none of the latter phases, GP2 or θ' were observed in samples aged to the hardness plateau (Figure 13(a),(b)). The higher hardening rate is evidently related to cluster formation that precedes the GP zone formation. The rapid hardening is observed only when both Cu and Be are present in the Al matrix, and indicates that interaction of Cu and Be atoms is required for the formation of clusters. The temporary softening of Al-Cu-Be alloy aged at 150°C (Figure 11) is a reversion of the cluster formation process that is a prerequisite for subsequent GP zone formation. A stable cluster composed of vacancies, Cu and Be atoms would explain the delay in GP zone formation by decreasing the number of vacancies and Cu atoms available for GP zone formation.

Clustering phenomena have been studied by De Sorbo et al(6) and others(7,8), who found that clustering in Al alloys will occur even at low temperatures. Migration of vacancy copper clusters through the Al matrix was proposed by Hart(9). The concept of "ternary clusters" of vacancies was used by Entwistle et al(10) to explain the accelerated hardening in Al-Cu-Mg alloy by the migration of Cu-Mg-vacancy clusters. Holmes and Noble(11) proposed the existence of Cu-Cd-vacancy clusters to explain an anomalous rise in resistivity and Noble(12) suggested that mobile vacancy-solute clusters exist in Al-Cu alloy with trace elements Cd, In or Sn. In a more recent study(93), hardening of an irradiated alloy was studied and attributed to the formation of small clusters. In the present work the process of Cu-Be-vacancy formation is probably preceded by a creation of solute rich regions around dislocations (due to the solute-dislocation interaction(80)), and subsequently clusters are formed. The possibility that the loops observed in the Al-3%Cu-0.1%Be alloy are the product of the clustering process is consistent with the observed association of the loops with the dislocation lines. The "vacancy nature" of the loops, while in agreement with the proposed model of the cluster, indicates only that vacancy clustering takes place during loop formation as it occurs in pure aluminum(94) and Al-Cu alloys(95). More extensive study, especially in-situ experiments with hot stage electron microscopy are required to establish the role of the loops in the clustering process in Al-3%Cu-0.1%Be alloy.

B. θ' AND θ PRECIPITATION

(1) Al-3%Cu Alloy

(a) θ' Formation

The specific resistivity vs. time plots for specimens aged at 380°C and at 325°C are shown in Figure 17. Similar plots were obtained for aging treatments at 340°C and 355°C. The fraction of precipitation completed (ξ) at time t (Figure 18), is given by eqn. (37) (see Jane et al(91)):

$$\xi = (\rho_o - \rho_t)/(\rho_o - \rho_\infty) \qquad (37)$$

where ρ_o, ρ_t and ρ_∞ are the specific resistivities at $t = 0$, $t = t$ and $t = \infty$ (reaction completed). The precipitation is assumed to obey Avrami type equation,

$$\xi = 1 - \exp(-kt^n) \qquad (17)$$

where k and n are constants related to the nuclei density and the growth mechanism. The parameter n is obtained from the slope of the plot log ($\ell n(1/1-\xi)$) and the activation energy from plot of $\ell n\left(\frac{d\xi}{dt}\right)_{\xi=0.5}$ vs. 1/T. The plots log ($\ell n\ 1/1-\xi$) vs. log t (Figure 19) are composed of two straight line segments and represent the θ' and θ precipitation, as verified

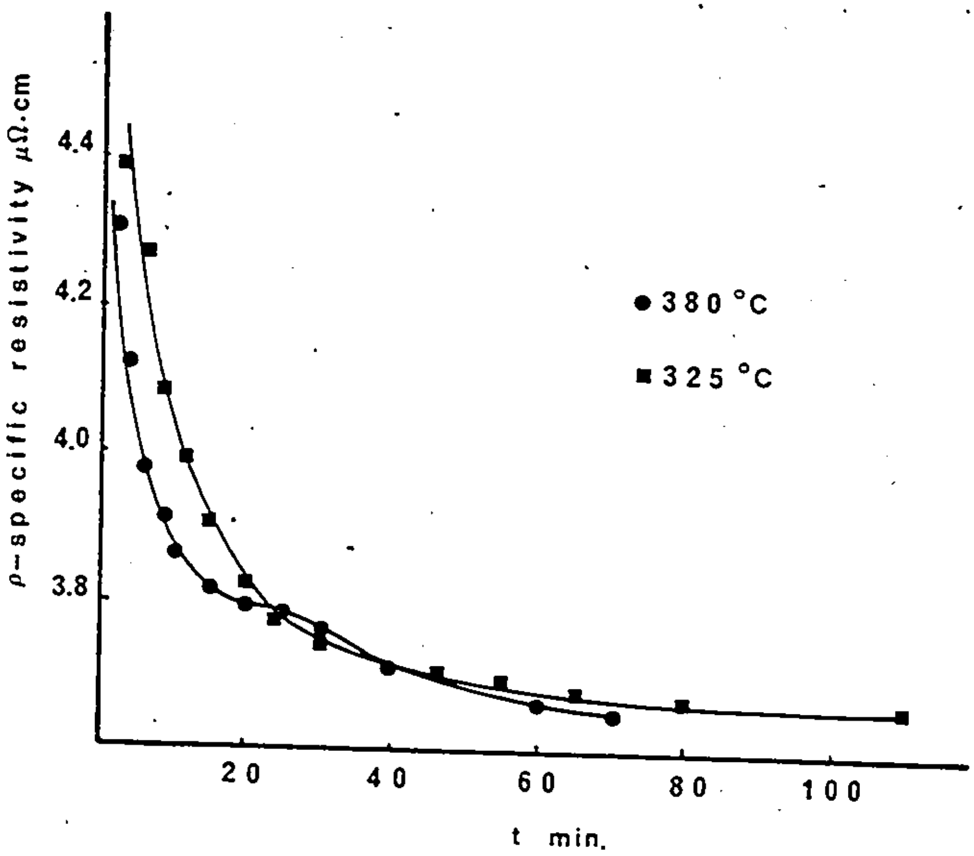

Figure 17 Al-3%Cu alloy, specific resistivity vs. time.

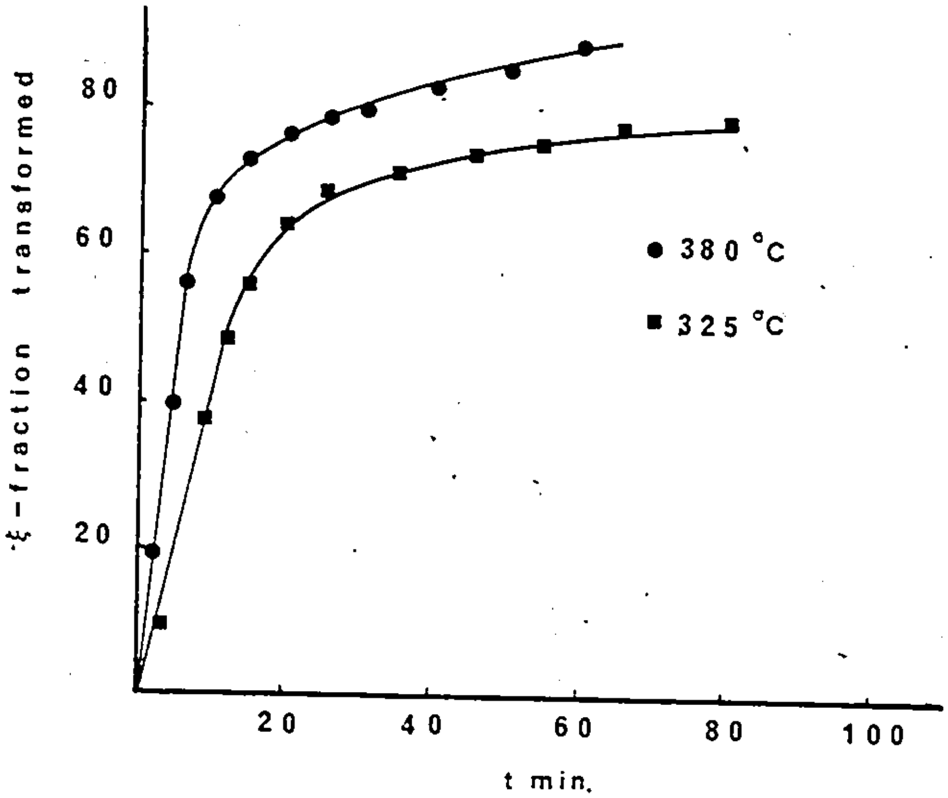

Figure 18 Al-3%Cu alloy, fraction transformed (ξ) vs. time.

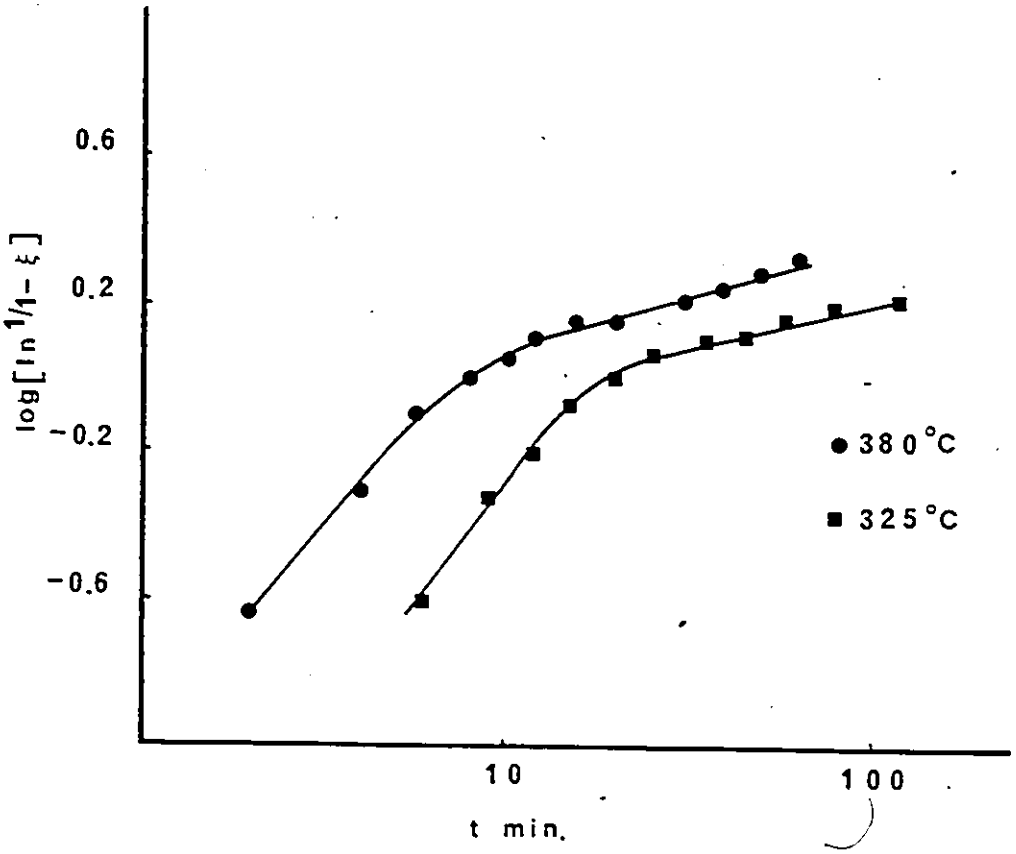

Figure 19 Al-3%Cu alloy, log (ℓn 1/1-ξ) vs. log t for the overall transformation.

by the TEM observation. The intersection of the two straight lines locates the time at which θ precipitation starts. The fraction transformed for θ' formation (calculated using eqn. (37) with the resistivity at the start of θ precipitation taken as ρ_∞) is given in Figure 20. Figure 21(a) and (b) show the θ' phase in TEM bright field mode and the corresponding electron diffraction pattern. The plot of log ($\ln 1/1-\xi$) vs. log t (Figure 22) gives a straight line for which the slope is $n = 1.68 \pm 0.1$, and indicates that the reaction obeys an Avrami equation for early saturation of nucleation sites. Papazian(36) and Melle et al(37) also show that θ' formation proceeds according to the Avrami equation; however, Papazian obtains $n = 1-1.2$. The activation energy for the transformation, obtained from plot of $\ln\left(\frac{d\xi}{dt}\right)_{\xi=0.5}$ vs 1/T (Figure 23) is 85.3 ± 10.9 kJ.

Ham(78) finds for disc of constant ratio that initially $n = 3/2$ but at longer times $n = 1$. For a case of a disc with constant thickness Ham(79) obtains $n = 2$ and at later times again $n = 1$. In the present study, a change in "n" towards $n=1$ was not observed (cf., Fig. 22), due to the formation of θ, which stops any further growth of θ' and initiates the θ' dissolution(43). The growth of θ' was studied extensively by Aaronson and Laird(32,33) and others(34). It is now well established that the thickening of θ' plates is slower than a diffusion controlled process and proceeds by lateral movement of ledges. The radial growth is, on the other hand, diffusion controlled or faster. It is proposed that the experimental value of

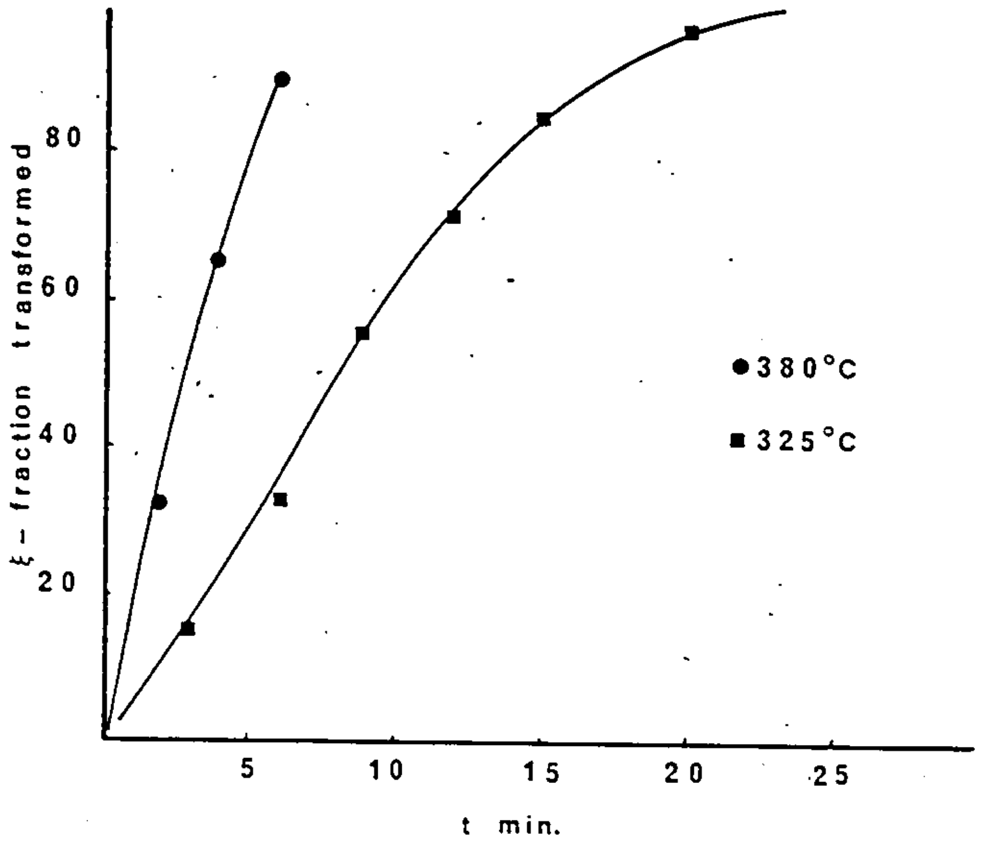

Figure 20 Al-3%Cu alloy, fraction transformed (ξ) of θ' vs. time.

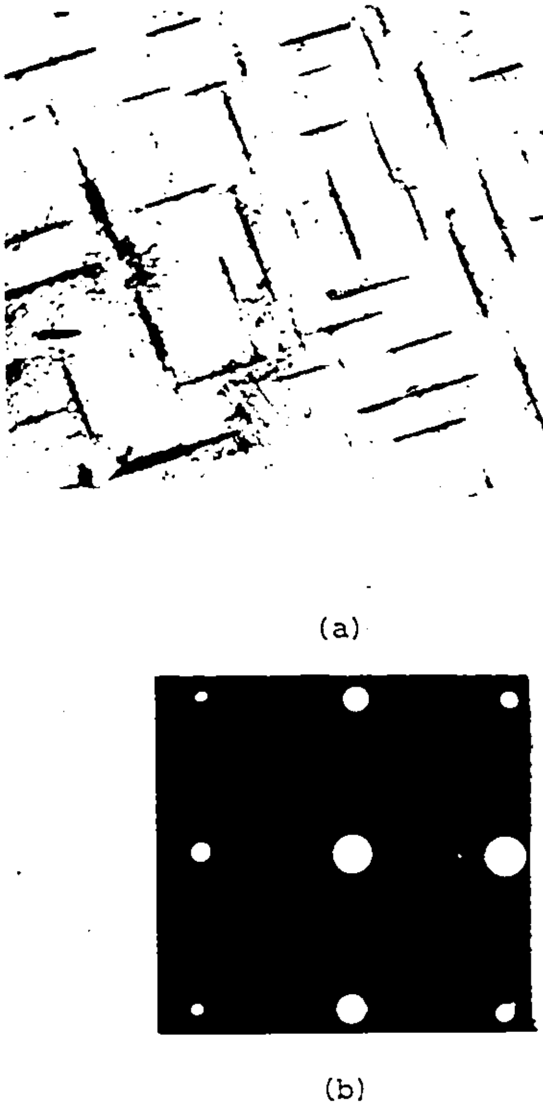

Figure 21 Al-3%Cu aged 10 min. at 380°C; (a) bright field ~<100> orientation, x20,000; (b) electron diffraction pattern, <100> matrix orientation.

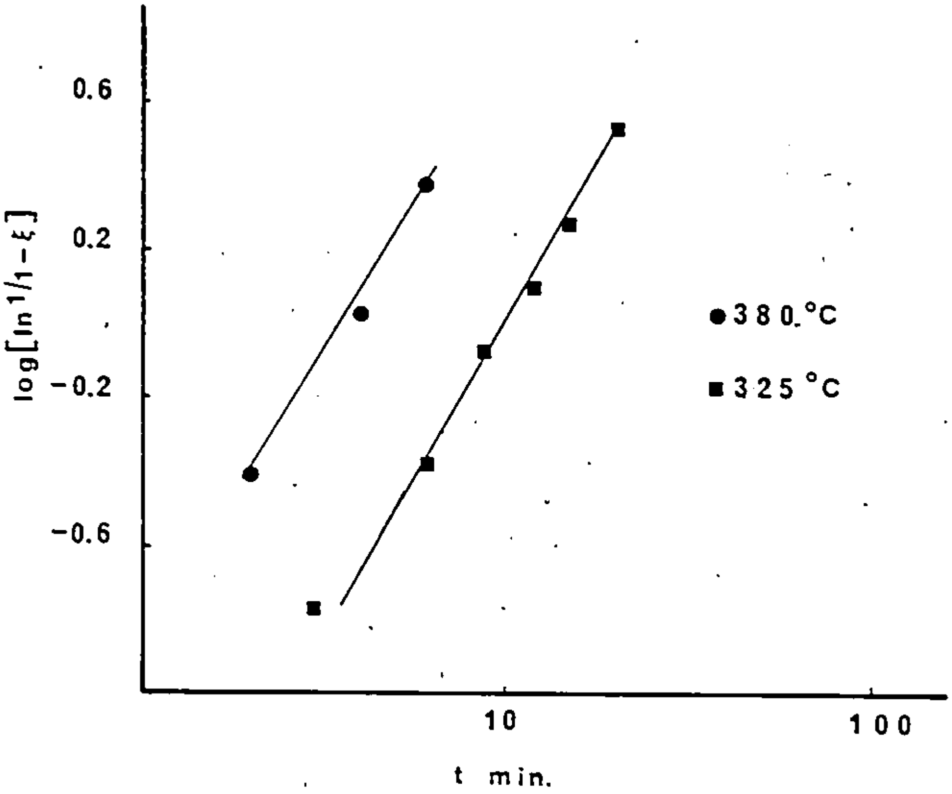

Figure 22 Al-3%Cu alloy, log(ℓn 1/1-$\varepsilon_{\theta'}$) for θ' phase vs. log t.

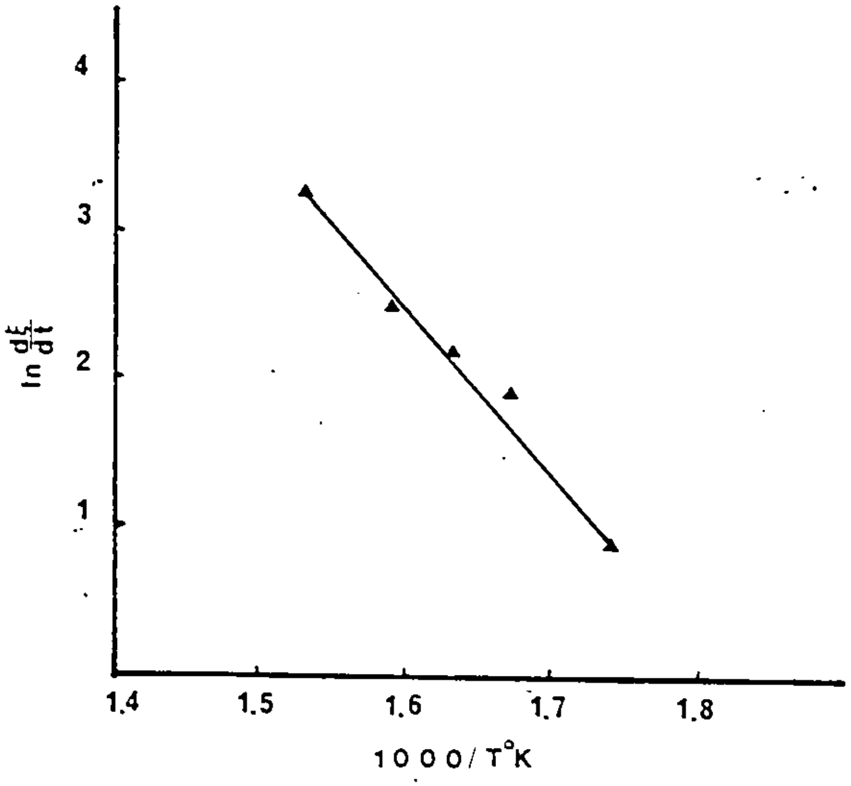

Figure 23 Al-3%Cu alloy, $\ell n\left(\frac{d\xi}{dt}\right)_{\xi=0.5}$ vs. 1/T (x1000).

n = 1.68, obtained in the present study, is due to the slow thickening of θ' plates, resulting in growth characteristics intermediate between the constant thickness (n = 2) and constant aspect ratios (n = 1.5) models of Ham.

The activation energy for θ' growth (85.3 kJ) is significantly lower than activation energy for diffusion of Cu in Al-Cu (129.6 kJ) as obtained by Murphy(41). Aaronson and Laird(33) report an activation energy of 75.2kJ - 117kJ for the thickening process and 79.8 kJ-98.6kJ for radial growth and the present result is in good agreement with their lower values. The relatively low activation energy suggests that the rate controlling process involves diffusion along dislocations and is consistent with the observed dislocations at the θ'/α interface(34). Diffusion along the edge of θ' plate and the ledges (which also are associated with dislocation(96)) are the more probable mechanisms.

(b) θ'→θ Transition

For the θ'→θ transition investigation, thin foils prepared from bulk samples, aged for 5, 10, 15, 20 and 60 mins. at 380°C, were inspected. Small rounded particles, identified as θ phase at later stage of aging by electron diffraction, are observed after 15 mins. aging period (Figure 24), their number increasing with aging time (Figure 25). Some of the particles have formed in the immediate vicinity of θ' precipitates and the dislocations (Figure 26). The presence of both θ' and θ is observed even at advanced stages of θ formation ($\xi>0.5$, Figure 27). Figure 28 shows a selected electron

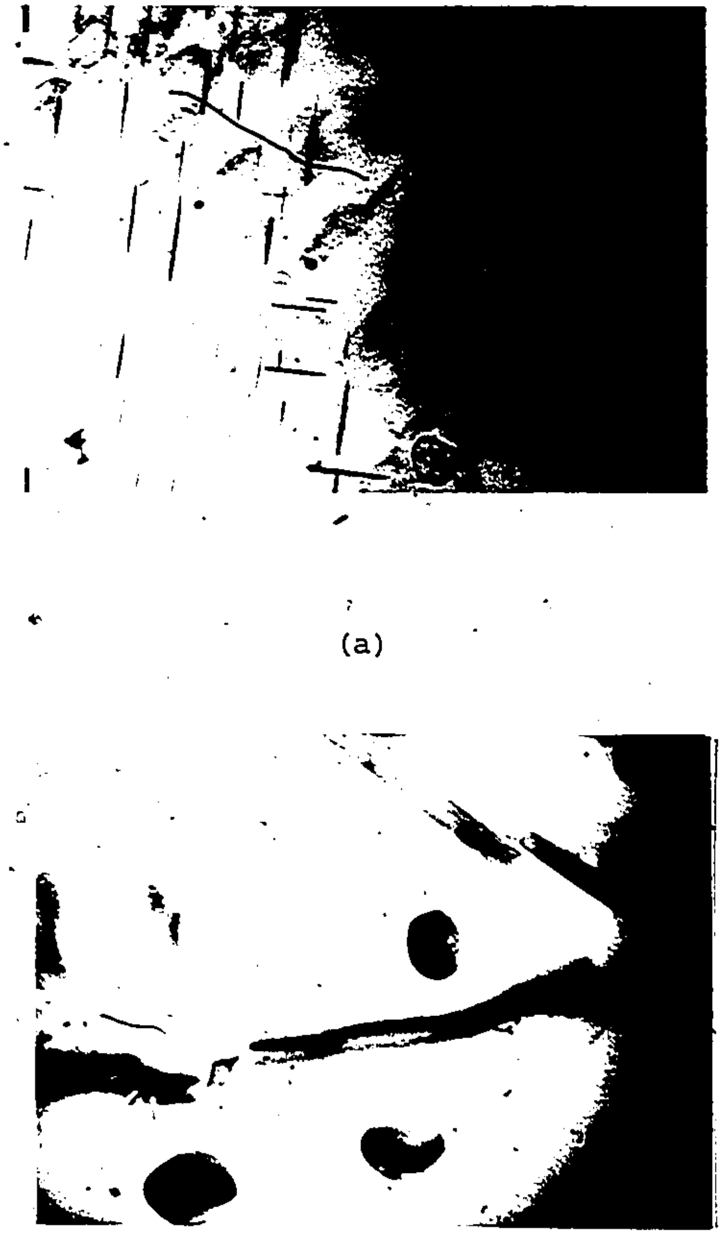

(a)

(b)

Figure 24 Al-3%Cu alloy, aged 15 min. at 380°C, θ phase formation: (a) x20,000; (b) x60,000.

(a)

(b)

Figure 25 Al-3%Cu alloy aged at 380°C: (a) 20 minutes; (b) 25 minutes, x20,000.

(a)

(b)

Figure 26 Al-3%Cu alloy, formation of θ phase on dislocations near θ' particles in (a) and (b), x60,000.

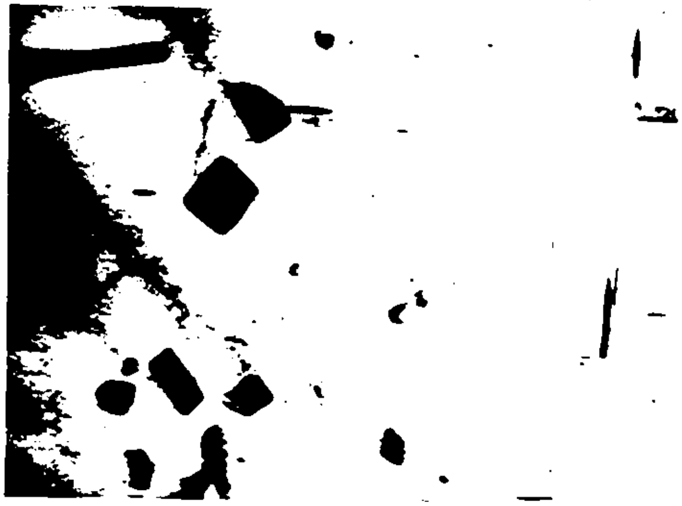

Figure 27 Al-3%Cu alloy, 60 min. at 380°C, mostly θ phase with some θ' particles, x 20,000.

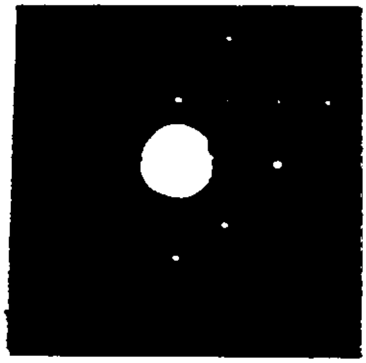

Figure 28 Al-3%Cu alloy, 60 min. at 380°C, electron diffraction pattern of θ.

diffraction pattern of single θ particle and the matrix taken after 60 mins. at 380°C. There is good agreement between TEM which shows that $\theta' \to \theta$ transition starts after 10 to 15 mins. and the resistivity method which locates the $\theta' \to \theta$ transition at approximately 10 mins. aging time at 380°C.

An IT diagram for the $\theta' \to \theta$ transition is constructed from the resistivity data by plotting the time at which formation starts vs. temperature (Figure 29). From the resistivity data the mean Cu concentration in solution, at time θ' starts to precipitate, is obtained using the relation:

$$x(\%\mathrm{Cu}) = 3\% - 2(4.5 - \rho_\theta) \tag{38}$$

(assuming the resistivity is a linear function of the solute concentration), where ρ_θ is the resistivity at which θ phase starts to precipitate. The metastable phase boundary of θ' between 300° - 380°C so obtained is superimposed on the equilibrium diagram (Figure 30). The α-θ' boundary reported by Hornborg(97) is shown for comparison.

Cahn(97a) has shown that the "metastable solvus" is more correctly termed "the coherent solvus" and is a part of the coherent phase diagram. The coherent phase diagram can be obtained by adding the elastic coherency strain energy

(W) contribution to the free energy of incoherent solid. The elastic energy is given by:

$$W = E_o \eta$$

where E_o is the effective modulus and η is the misfit parameter related to the lattice parameter (a) of the new phase and (a_o) of the matrix,

$$\eta = \frac{a-a_o}{a_o}$$

By adding the elastic energy, the common tangency points move inwards, resulting in a coherent solvus line, interior to the equilibrium incoherent solvus. Experimental evidence for the Al-Zn alloy, found in the work of Murakami et al$^{(97b)}$ and De Fontaine$^{(97c)}$, supports this model.

(c) θ Precipitation

The fraction of θ precipitation as a function of time, for 380°C and 325°C is given in Figure 31. A plot of $\ln(\frac{d\xi}{dt})_{\xi=0.5}$ vs. 1/T (Figure 32) gives the activation energy of 111.1 ± 5.2 kJ. The linear plot for log ($\ln 1/1-\xi$) vs. log t (Figure 33) indicates Avrami type kinetics for θ precipitation with $n = 0.63 \pm 0.04$, which according to Harper's treatment$^{(81)}$ is characteristic of precipitation on dislocations. Ham$^{(82)}$ has shown that the Harper equation can be used only as an approximation for the initial and very short period of precipitation,

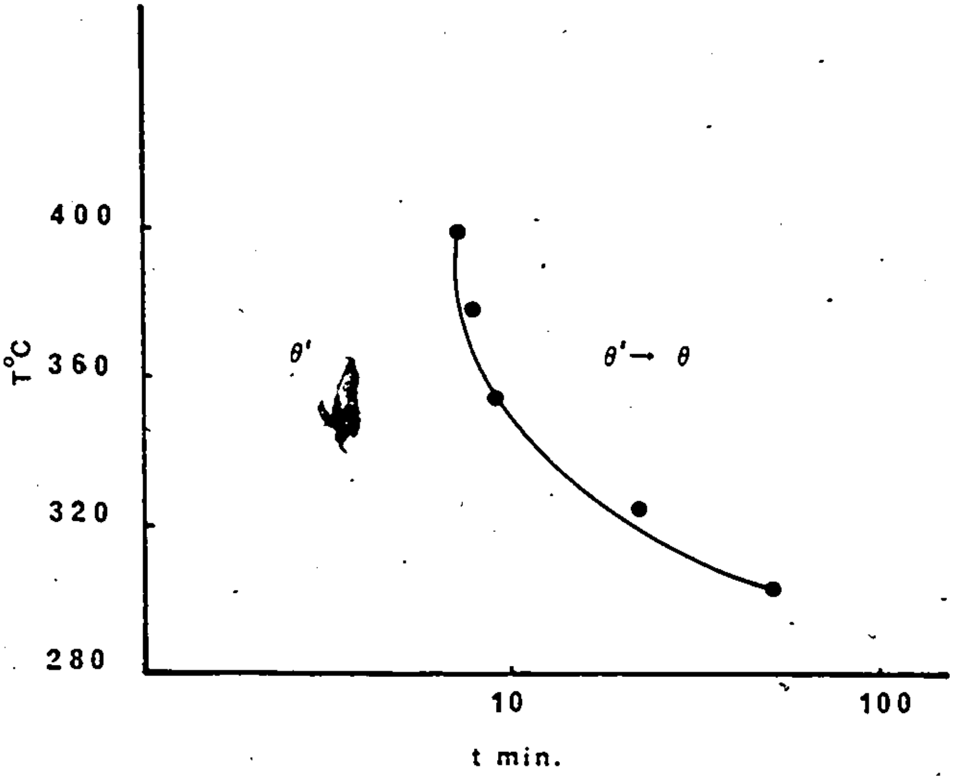

Figure 29. Al-3%Cu alloy, a TTT diagram for θ'→θ transformation.

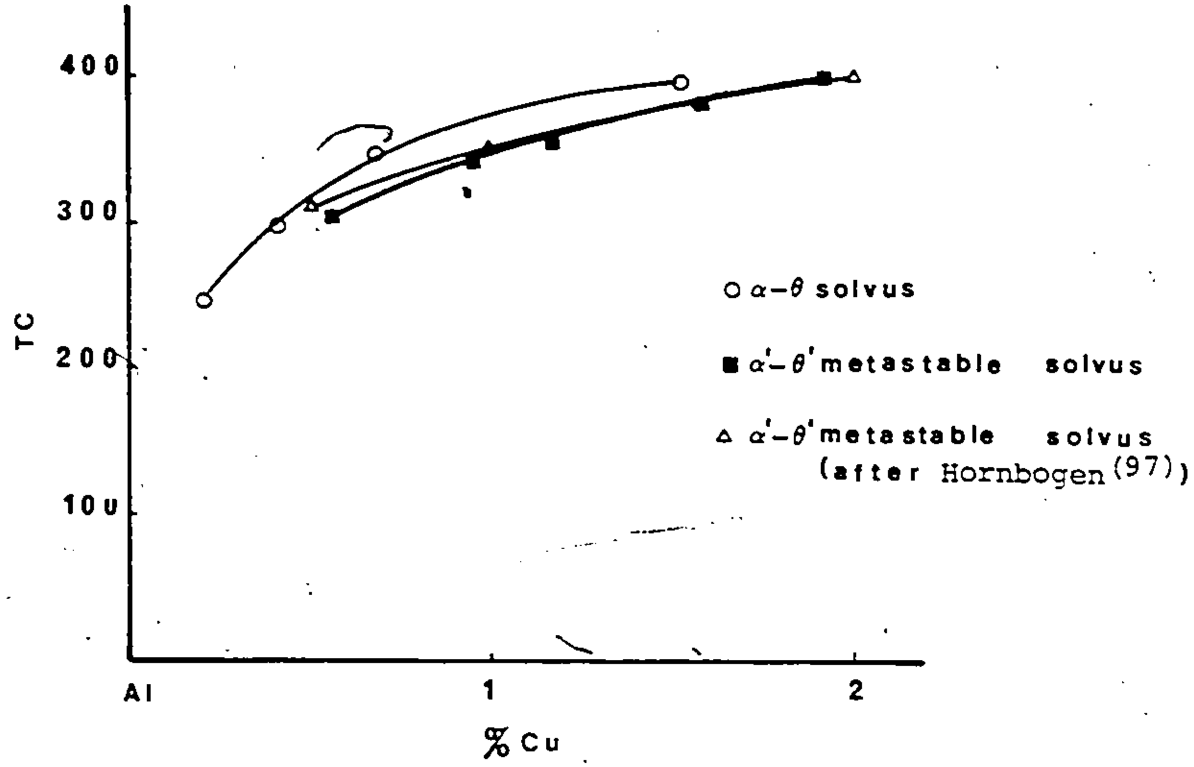

Figure 30 Al-3%Cu alloy, the Al-rich side of Al-Cu phase diagram, α/θ and the metastable α'/θ' solvus lines.

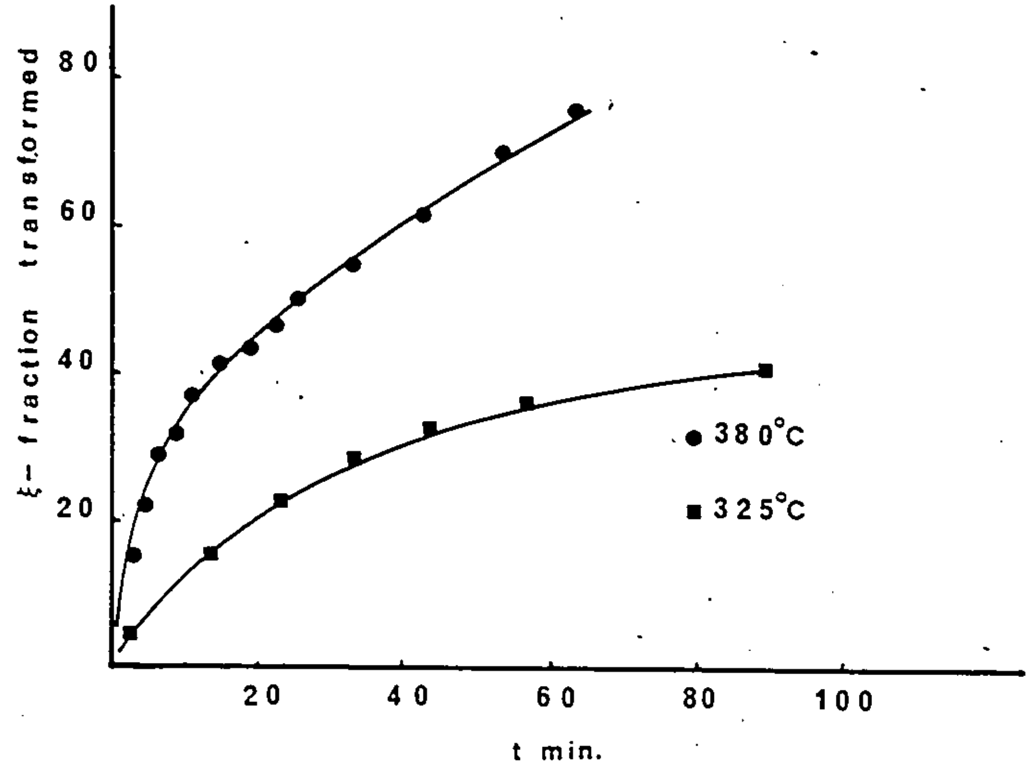

Figure 31 Al-3%Cu alloy, fraction transformed (ξ) of θ vs. time.

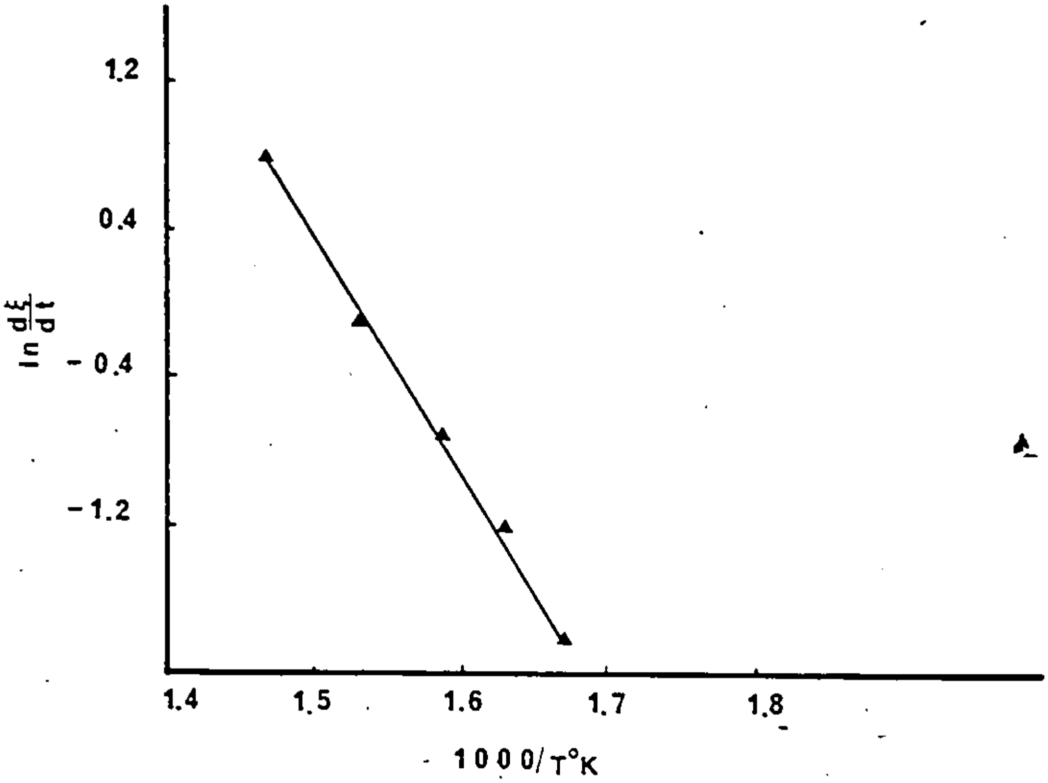

Figure 32 Al-3%Cu alloy, $\ell n\left(\frac{d\xi}{dt}\right)_{\xi=0.5}$ vs. 1/T, (x1000).

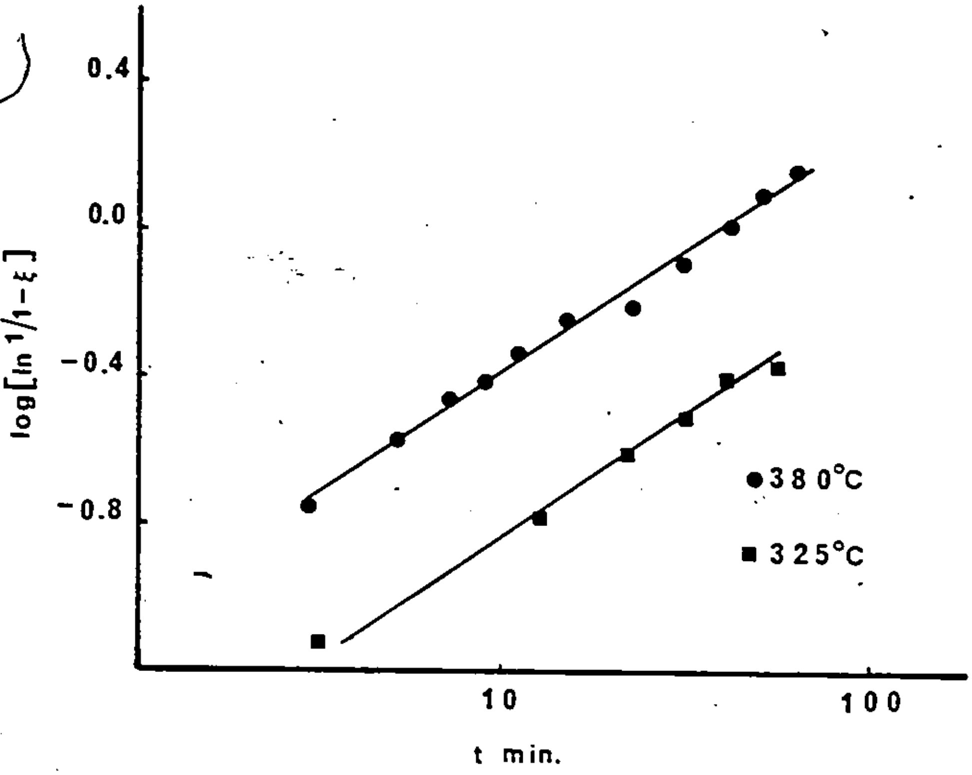

Figure 33 Al-3%Cu alloy, log(ℓn $1/1-\xi_\theta$) vs. log t for θ precipitation.

or in the case that the diffusion of solute atoms can be described by a steady state equation, normalized far from the particle to the instantaneous value of the average solute density.

It is proposed that the good experimental agreement with the Harper equation(81), obtained in the present study, is due to the θ' particle dissolution during θ formation. The θ' precipitates act as localized sources of solute and create a quasi-steady solute distribution.

A possible sequence which preserves the "precipitation on dislocation" character, involves the dissolution of θ', transport of Cu atoms to dislocation and by "pipe diffusion" to the growing θ particle. This model is consistent with observed presence of θ' particles even at advanced stage of θ precipitation and with the existing dislocation network connecting θ' and θ (Figure 26). It is also in agreement with the recent study of Butler(43).

(2) Al-3%Cu-0.1%Be Alloy

(a) θ' Formation

The resistivity measurements for the Al-3%Cu-0.1%Be alloy vs. aging time, at 380°C and 325°C, are given in Figure 34. The plots log (ℓn 1/1-ξ) vs. log t (Figure 35) are comprised of two straight line segments that represent θ' and θ precipitation, the intersection taken as the onset of θ formation. TEM observation (described below) are in agreement with this interpretation of resistivity plots.

The fraction transformed for θ' is given in Figure 36 and TEM bright field micrograph and the corresponding electron diffraction pattern (Figures 37(a) and (b)) confirm

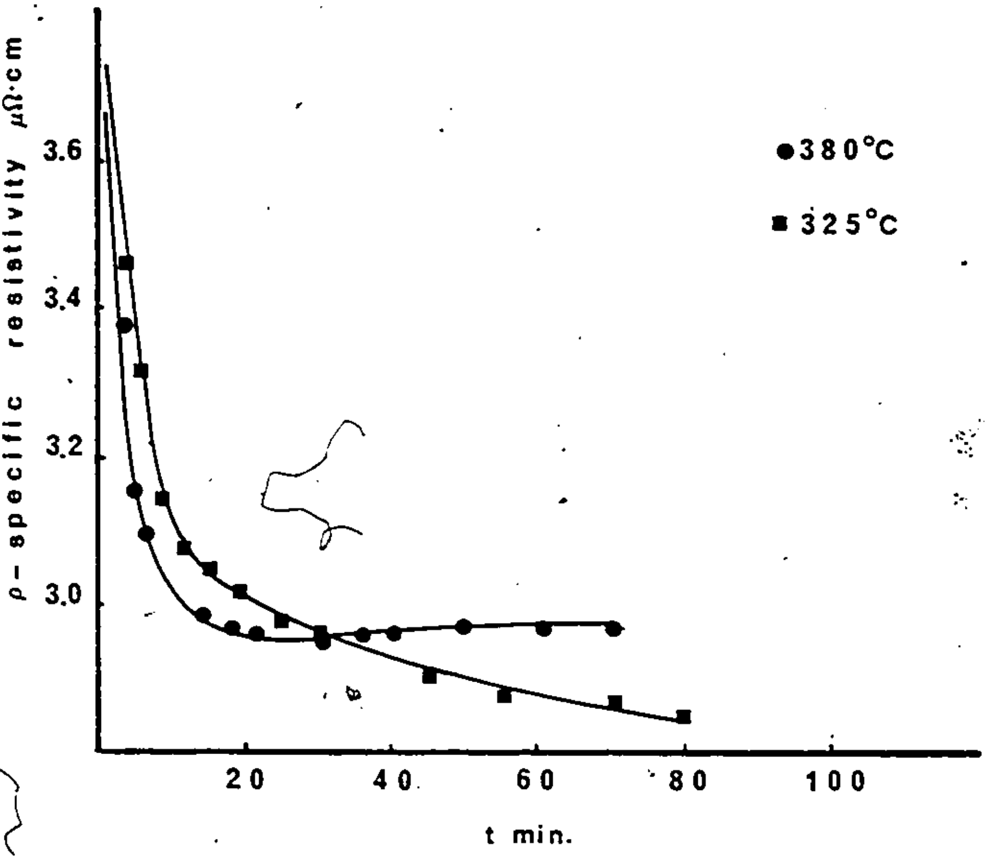

Figure 34 Al-3%Cu-0.1%Be alloy specific resistivity vs. time.

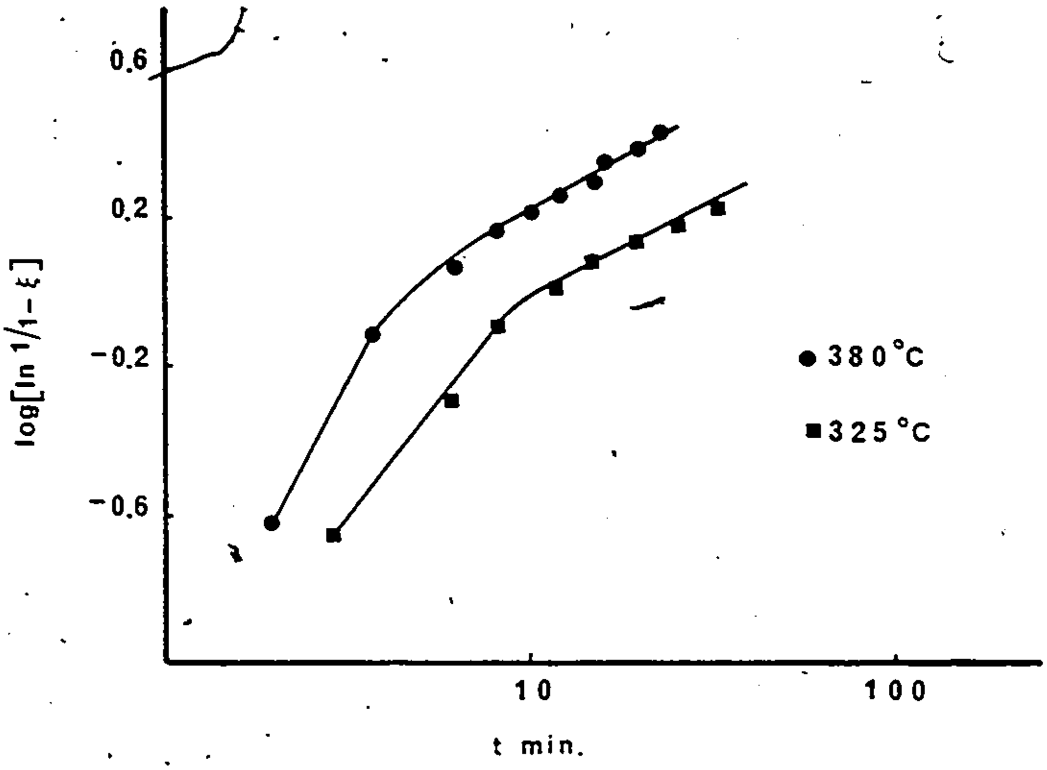

Figure 35 Al-3%Cu-0.1%Be alloy, log(ℓn 1/1-ξ) log t, for the overall transformation.

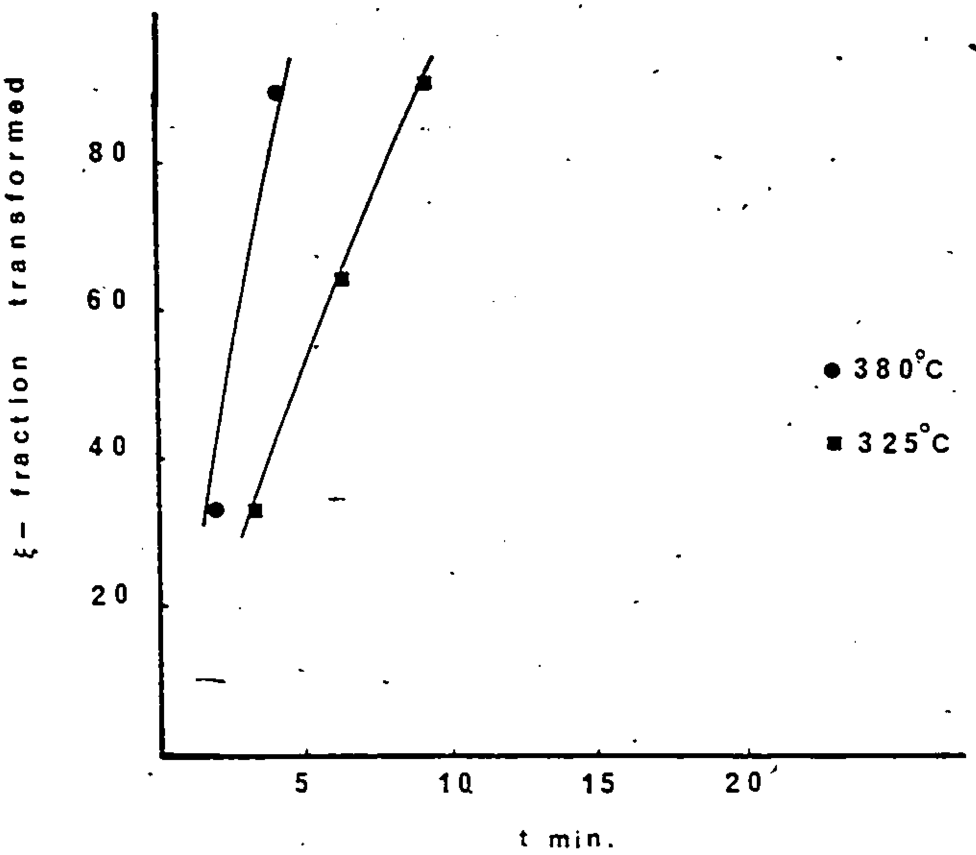

Figure 36 Al-3%Cu-0.1%Be alloy, fraction transformed (ξ) of θ' vs. time.

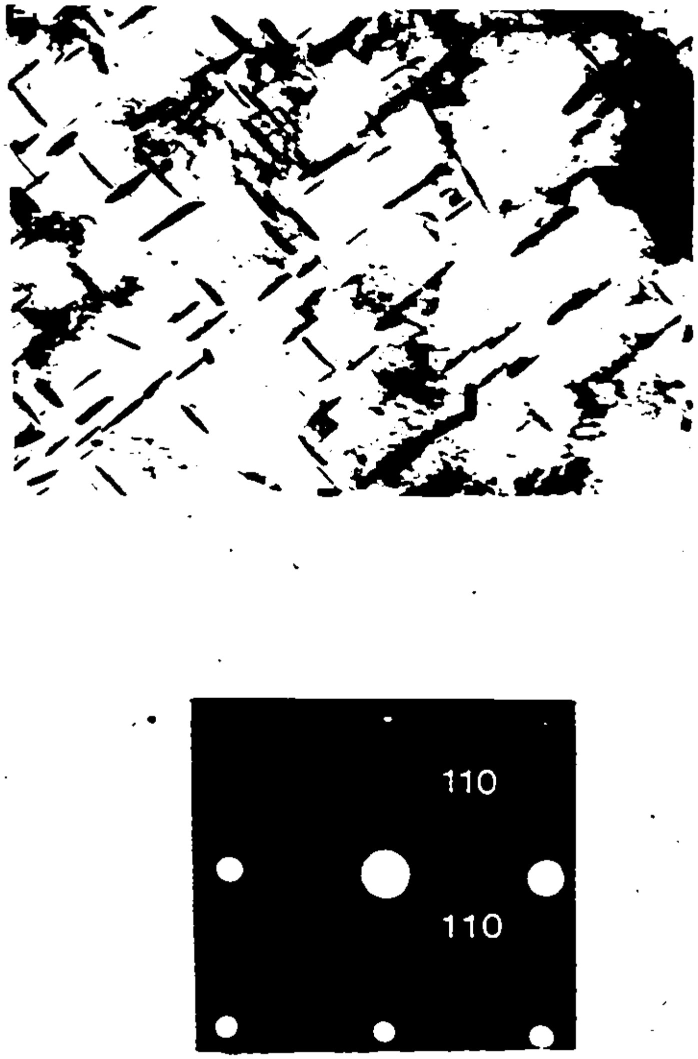

Figure 37 Al-3%Cu-0.1%Be alloy, aged 5 min. at 380°C: (a) bright field ~<100> orientation, x 20,000; (b) electron diffraction pattern, ~<100> matrix orientation.

the presence of θ' at this stage of precipitation. The plot of log(ℓn 1/1−ξ) vs. log t is a straight line (Figure 38) with the slope n = 1.6±0.1 which indicates Avrami type kinetics. The activation energy, calculated from the slope of $\ln\left(\frac{d\xi}{dt}\right)_{\xi=0.5}$ vs. 1/T, is 76.1±12.7 kJ/mole (Figure 39).

(b) θ'→θ Transition

Thin foils prepared from bulk samples aged 5, 10, 15, 20 and 60 mins. at 380°C were examined under TEM. Aging for 5 mins. at 380°C produces only θ' as evidenced in TEM bright field micrograph and the corresponding electron diffraction pattern (Figures 37(a) and (b)). Aging for 10 mins. at 380°C produces almost complete transition to θ phase as is seen in Figure 40(a) and confirmed by electron diffraction (taken after 60 mins. of aging at 380°C) in Figure 40(b). Both TEM and resistivity techniques locate the onset of θ formation at 5-10 min. of aging at 380°C. Using the resistivity data, an IT diagram was constructed in a manner similar to section (1)(b) and is shown in Figure 41.

(c) θ Precipitation

The fractions of θ precipitated at 380°C and 325°C vs. time are plotted in Figure 42. The activation energy, obtained from the slope of the plot $\ln\left(\frac{d\xi}{dt}\right)_{\xi=0.5}$ vs. 1/T is 108.5 ± 14.1kJ (Figure 43). The plot of log (ℓn 1/1−ξ) vs. log t (Figure 44) is linear ~~as~~ required for an Avrami-type reaction. The slope n = 0.72±0.07 indicates that, as in the case of Al-3%Cu alloy, dislocations play an important role in the θ formation.

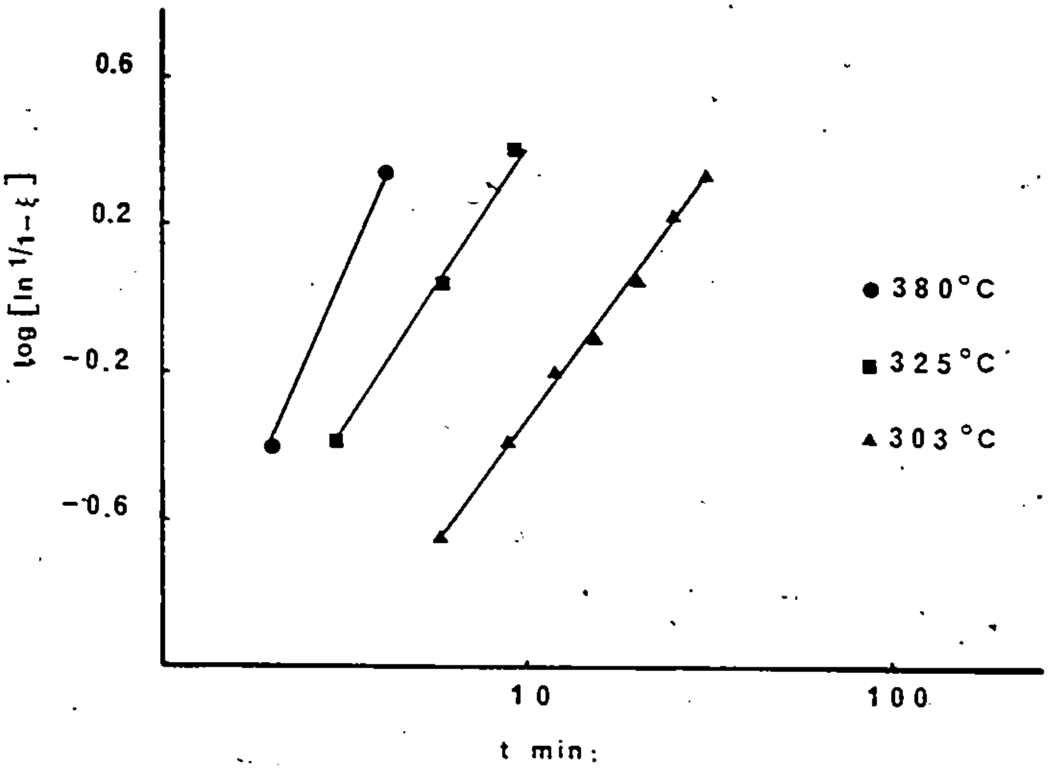

Figure 38 Al-3%Cu-0.1%Be alloy, log(ℓn 1/1-$\xi_{\theta'}$) for θ' phase vs. log t.

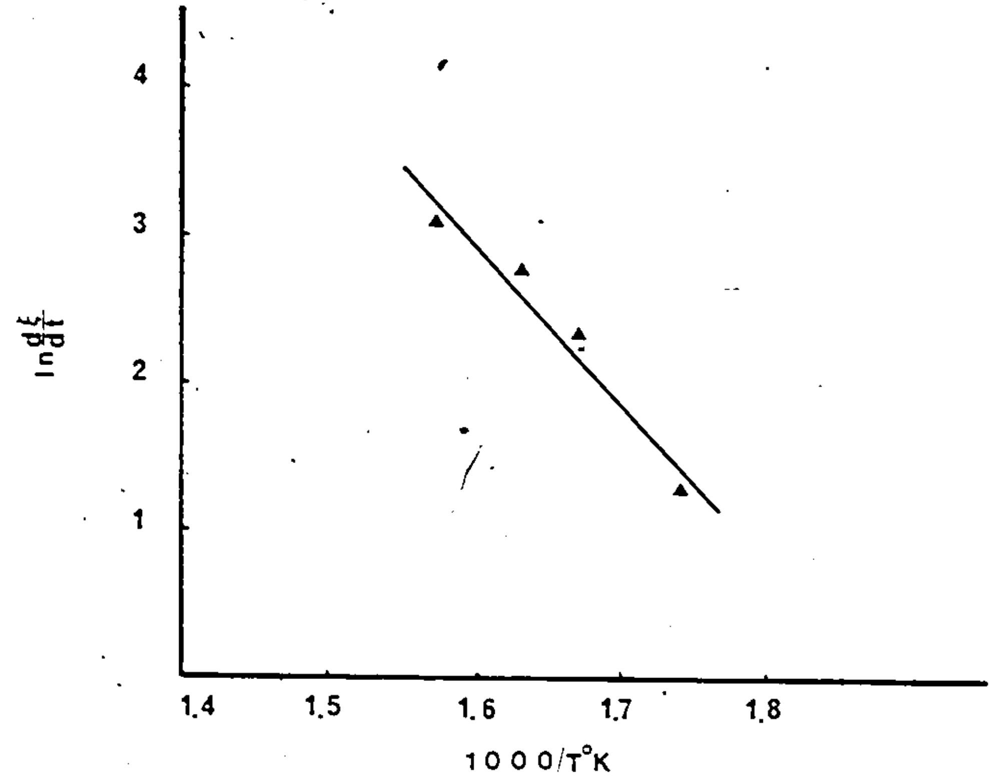

Figure 39 Al-3%Cu-0.1%Be alloy, $\ln\left(\frac{d\xi}{dt}\right)_{\xi(\theta)=0.5}$ vs. 1/T, (x1000).

(a)

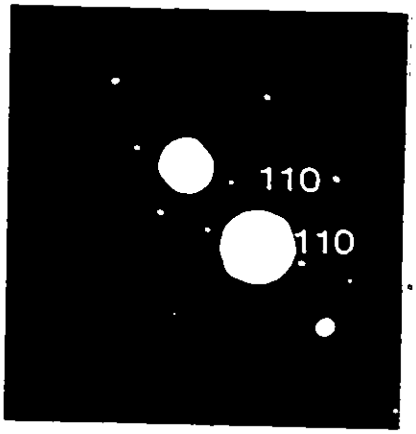

(b)

Figure 40 Al-3%Cu-0.1%Be alloy: (a) aged 10 min. at 380°C, bright field mode, showing mostly θ particles, ~<100> orientation, x20,000; (b) aged 60 min. at 380°C, electron diffraction pattern of θ.

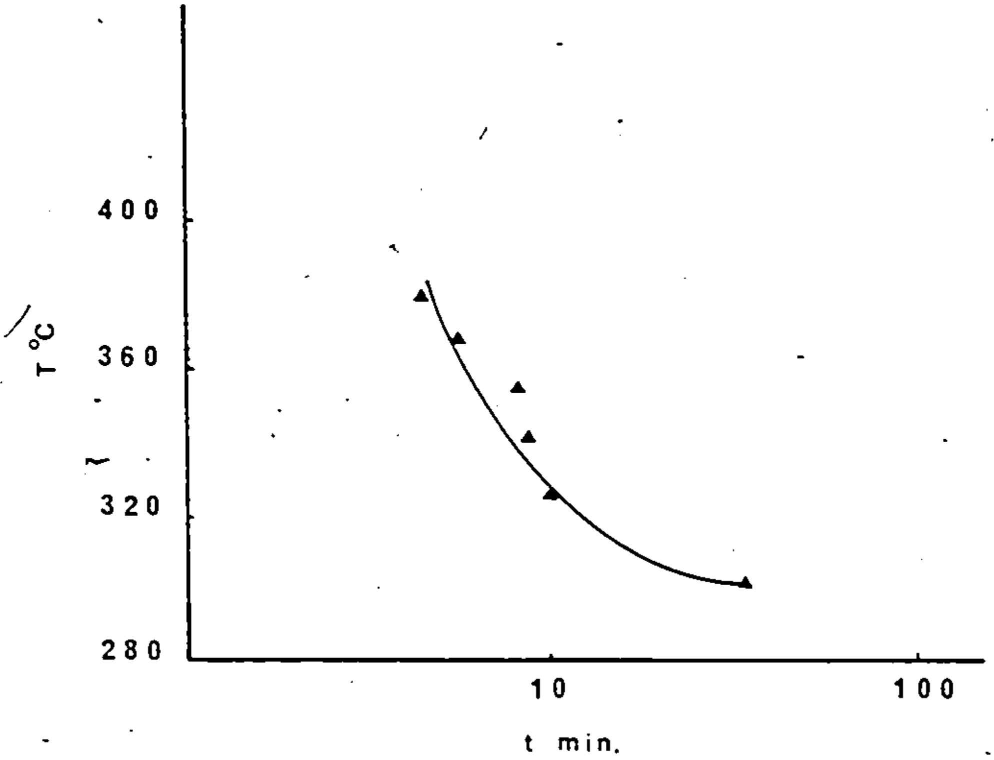

Figure 41 Al-3%Cu-0.1%Be alloy, a TTT diagram for θ'→θ transition.

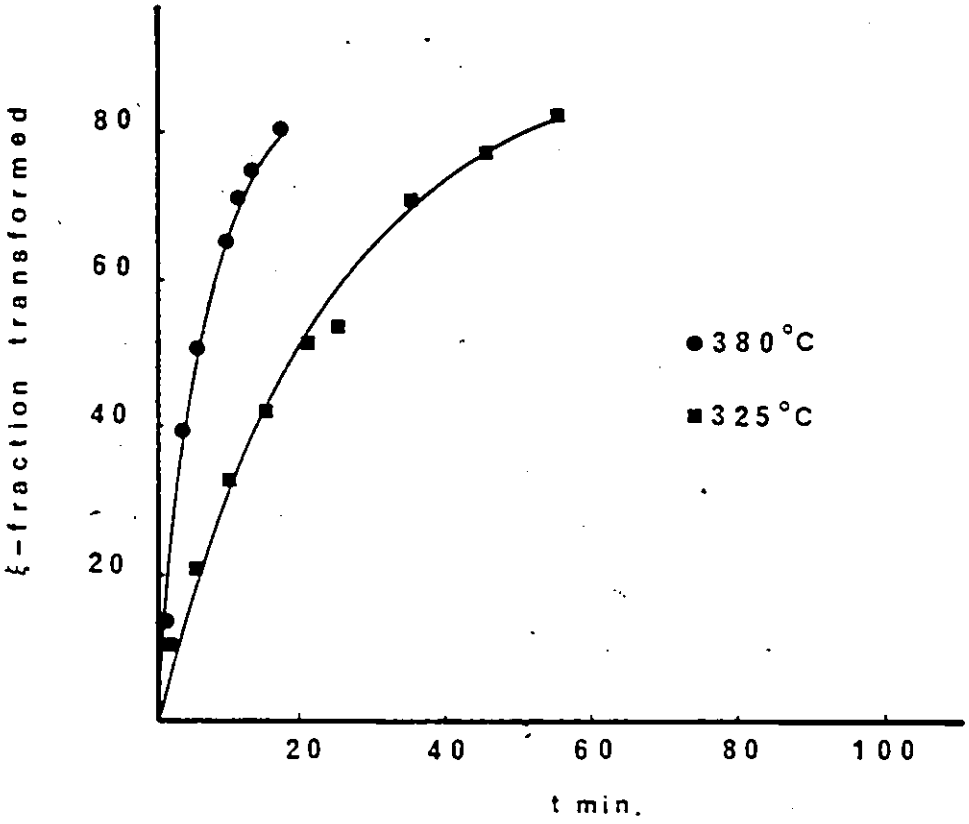

Figure 42 Al-3%Cu-0.1%Be alloy, fraction transformed (ξ) of θ vs. time.

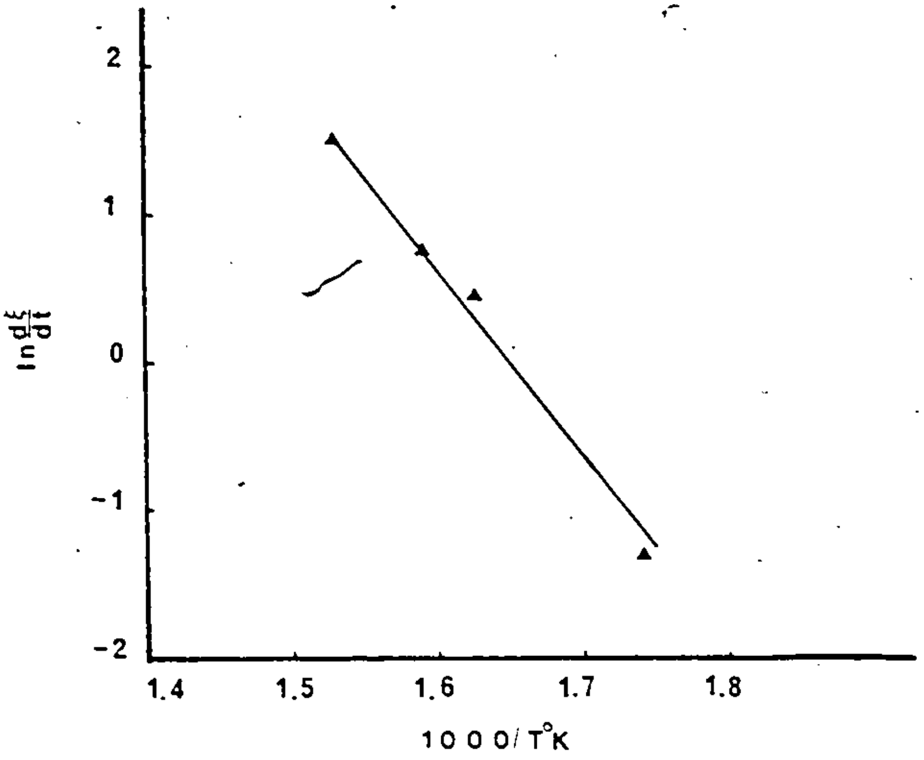

Figure 43 Al-3%Cu-0.1%Be alloy, $\ln\left(\frac{d\xi}{dt}\right)_{\xi(\theta)=0.5}$ vs. 1/T, (x1000).

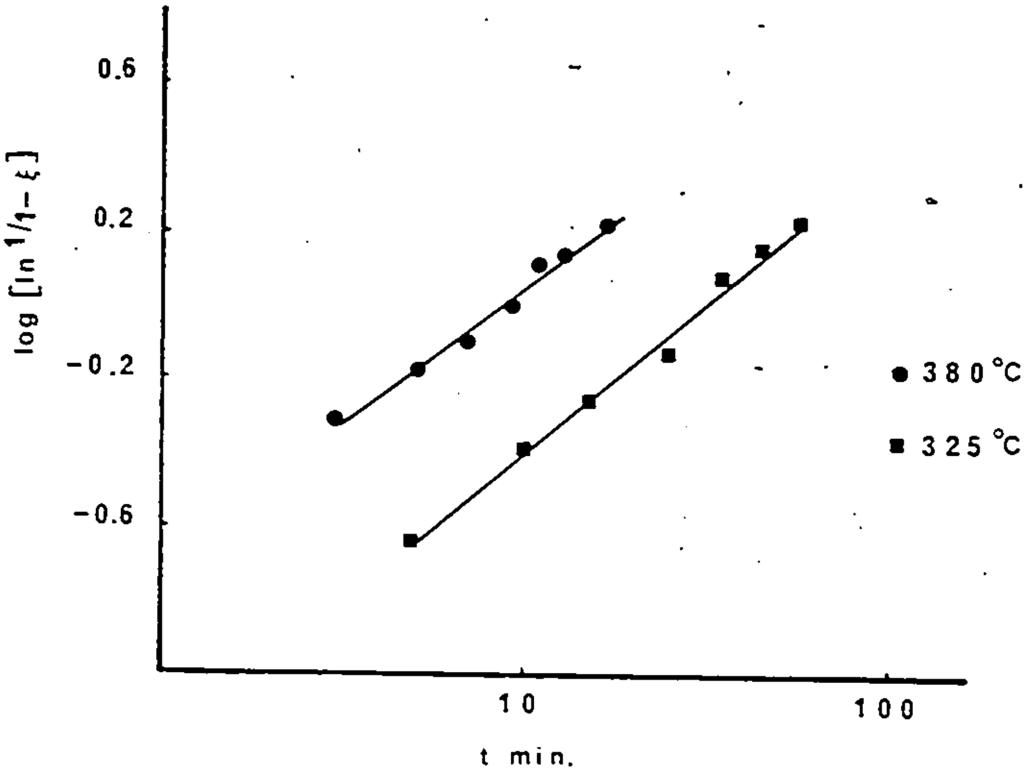

Figure 44 Al-3%Cu-0.1%Be alloy, log($\ln 1/1-\xi_\theta$) vs. log t for θ precipitation.

(d) Number of θ Particles

Density of particles (number/unit area) in Al-3%Cu-0.1%Be was estimated from SEM micrographs (Figure 45) and compared to Al-3%Cu alloy. Between 500-1000 particles were counted for each aging treatment and the fraction of θ precipitates was estimated by TEM. Thin foils were prepared from bulk samples (subjected to identical treatments as the SEM samples) and examined at <100> orientation which allows to distinguish between θ' and θ particles. The results are summarized in Table 2 and show significantly higher density of θ in Al-3%Cu-0.1%Be alloy aged for 10 and 20 min. at 380°C.

(3) Comparison Between Al-3%Cu and Al-3%Cu-0.1%Be Alloys

The precipitation of θ' and θ obeys the Avrami equation for both alloys. The activation energies for both phases are approximately the same (within experimental error) and so are the n values, indicating the same rate controlling step and the same growth mechanism. The Be addition does not change any of these characteristics of θ' and θ formation and the discussion of the experimental results presented in section (1)(c) is equally valid for Al-3%Cu-0.1%Be alloy.

The important effect of Be is seen in $\theta' \rightarrow \theta$ transition and the rate of θ formation. Comparison of the TTT diagrams (Figures 29 and 41) shows that the $\theta' \rightarrow \theta$ transition, occurs earlier in Al-Cu-Be alloy and inspection of TEM micrographs (Figures 25 and 40) and the plots of $\xi(\theta)$ vs. time (Figure 46) indicate the time to complete the $\theta' \rightarrow \theta$ transition is much shorter when Be is present. The fact that the activation

Figure 45 Al-3%Cu alloy, aged (a) 10 min. at 380°C, (b) 30 min. at 380°C and Al-3%Cu-0.1%Be alloy aged (c) 10 min. at 380°C and (d) 30 min. at 380°C. SEM micrographs, x10,000. Note the different morphology of θ particles in (c) as compared to θ' in (a)

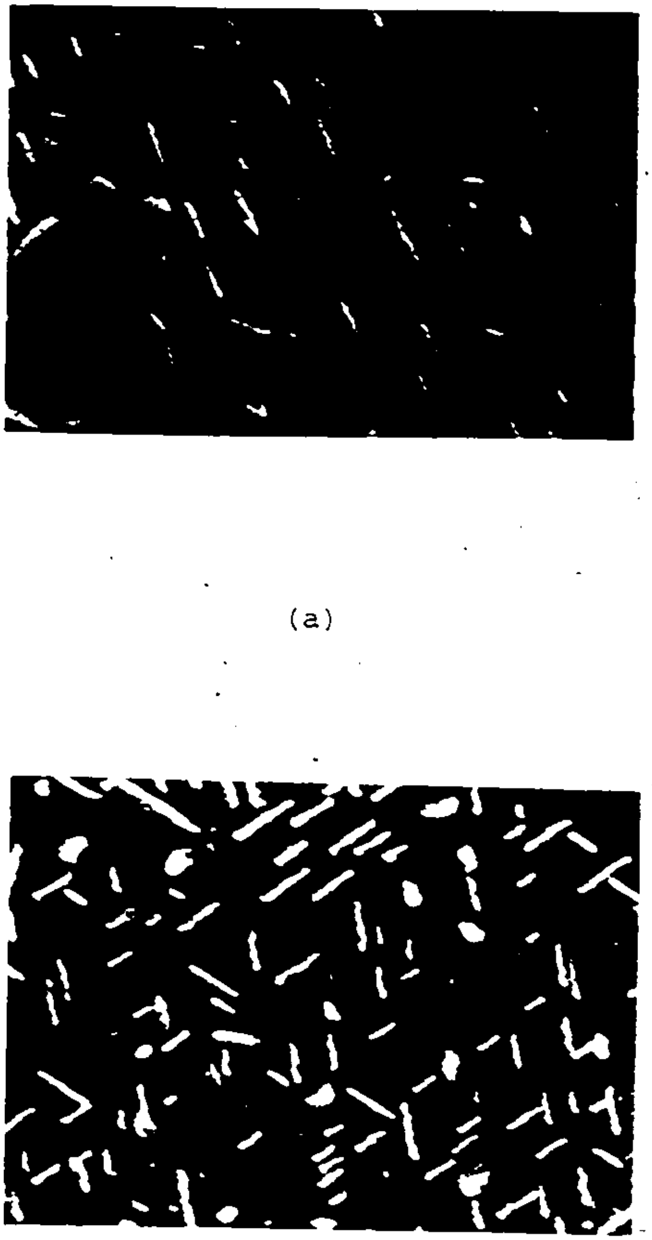

(a)

(b)

Figure 45 (cont'd.).

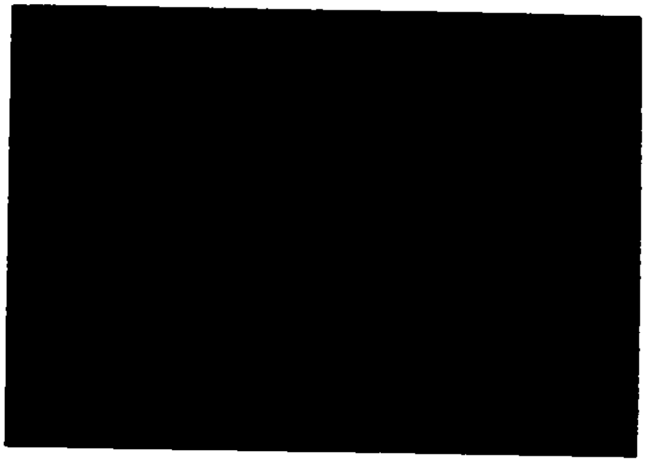

(c)

(d)

Table 2

Number of Precipitate Particles/cm^2 x 10^{-8} In Alloys Aged at 380°C

Alloy	Particle Count	Aging Time at 380°C		
		10 min.	20 min.	30 min.
Al-3%Cu	Total (θ'+θ)	2.54	2.0	2.5
	Fraction of θ	~0	~0.25	~0.6
	θ Particles	~0	0.5	~1.5
Al-3%Cu-0.1%Be	Total (θ'+θ)	4.31	1.8	1.9
	Fraction of θ	~1	~1	~1
	θ Particles	4.31	1.8	1.9

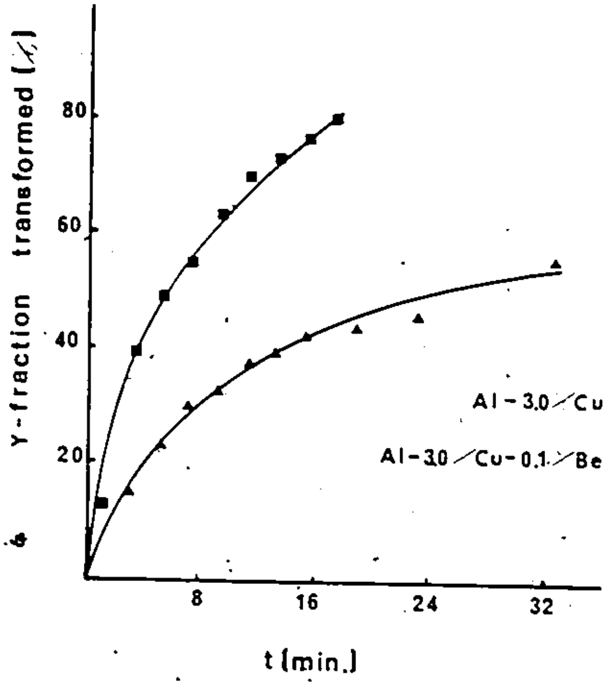

Figure 46 Al-3%Cu and Al-3%Cu-0.1%Be alloys, fraction transformed of θ vs. time at 380°C.

energies and the mechanisms of θ growth are the same in both alloys suggests that the effect of Be lies in the nucleation stage that precedes the growth process. It is proposed that Be creates a higher nuclei density of θ phase which results in an earlier and faster $\theta' \rightarrow \theta$ transition. This view is in agreement with the observed higher densities of θ particles in Al-3%Cu-0.1%Be (Table 2) and the calculated 'k' values in $\xi = 1 - \exp(-kt)$ (Figure 47). The higher k values, obtained for Al-Cu-Be alloy indicate a higher density of nucleation sites which in the case of the Harper equation are expressed in terms of dislocation densities. In section (1)(c), a model for θ formation was proposed, in which the dislocations are seen as a transportation network rather than nucleation sites. According to this model, the k value in the case of θ precipitation is related directly to the nuclei density.

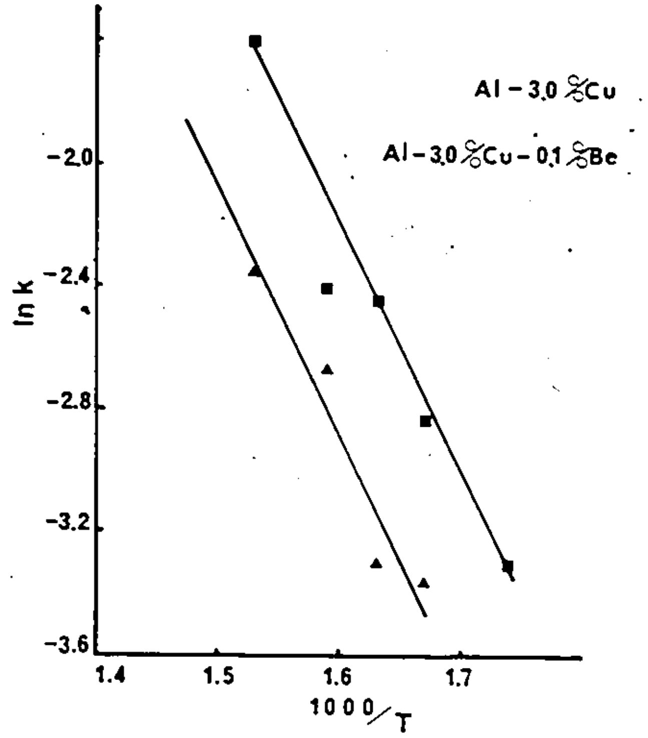

Figure 47 Al-3%Cu and Al-3%Cu-0.1%Be alloys, ℓn k vs. 1/T, (x1000).

CHAPTER V

DETERMINATION OF Be CONTENT AND THE STRUCTURE OF θ PHASE IN Al-3%Cu-0.1%Be ALLOY

Direct spectroscopic analysis of Be using the Kevex Energy Dispersive System is not possible due to the low atomic number of Be (n = 4). Several attempts using more sophisticated techniques, e.g., EDS with Li window by Met-Chem Testing Laboratories, Dearborn, Michigan, and electron energy loss analysis (E.E.L.S.) by McMaster University were unsuccessful due to insufficient sensitivity and contamination problems. The analysis was therefore performed using a combination of techniques: EDS, X-ray diffraction, metallography and extraction.

Microhardness (used mainly to identify the θ phase in the metallographic samples), EDS, and X-ray diffraction techniques were used in a comparative study of Al-53%Cu (Al_2Cu) and Al-53%Cu-2.7%Be alloys. The microhardness values in Table 3 represent the average of 6 readings and indicate an increase in hardness of θ phase when Be is present in the compound.

To determine the Be content in θ phase, EDS analysis was performed on the Al-53%Cu and Al-53%Cu-2.7%Be alloys. Using standards of Al, Cu and Al_2Cu, at least three determinations were made from at least three different areas of each sample, and the composition calculated using the NBS (Frame B) program.

The change in the atomic ratio Al/Cu (column 4, Table

Table 3

<u>Microhardness, X-ray Diffraction and EDS Analyses of 0 Phase</u>

0 Phase	Microhardness (HV)	Lattice Constants (nm)	Al/Cu Atomic Ratio	Composition
0 in Al-53%Cu	505±10	a = 0.6066 c = 0.4874	2.13±0.06	~$Cu_{0.98}Al_{2.08}$
0 in Al-53%Cu-2.7%Be	532±30	a = 0.6042±0.001 c = 0.4847±0.001	1.81±0.06	~$Cu_{0.86}(Al_{1.92}Be_{0.22})$

3) was calculated from the raw counts (i.e., the computer correction program was not used) and is taken to be indicative of Be replacing Al atoms.

The Be content was calculated using the computer corrected data and the difference method. The experimental error was estimated to be 2.9 atomic % for Al and 0.6 atomic percent for Cu. The approximate stoichiometric formula for $Cu(Al,Be)_2$ compound was calculated to be $Cu_{0.86}(Al_{1.92}Be_{0.22})$. However, the Be content is subject to problems associated with finding small differences between uncertain large numbers.

X-ray diffraction technique was employed to study possible changes in the unit cell of $Cu(Al,Be)_2$ compound. Powder samples of $CuAl_2$ and $Cu(Al,Be)_2$ alloys were prepared and admixed with W powder which served as internal standard. Shifts in θ peaks were measured relative to the nearest W peak to eliminate any changes of 2θ due to misalignment and the mounting procedure. Reproducibility was checked in three successive runs and the observed experimental error was $\pm 0.1^{\circ}$. Table 1 in Appendix I summarizes the experimental findings and shows that the peaks in $Cu(Al,Be)_2$ alloy are shifted to higher values indicating a decrease of 0.4±0.2% in "a" and 0.55±0.2% in the "c" lattice constants respectively. The observed change is in agreement with the smaller Be atoms replacing Al atoms, the mean atomic volume of Al, Cu and Be (based on their respective g.at. volume (cm^3) of 9.996, 7.09 and 4.898) being 0.0166, 0.0118 and 0.0081 nm^3.

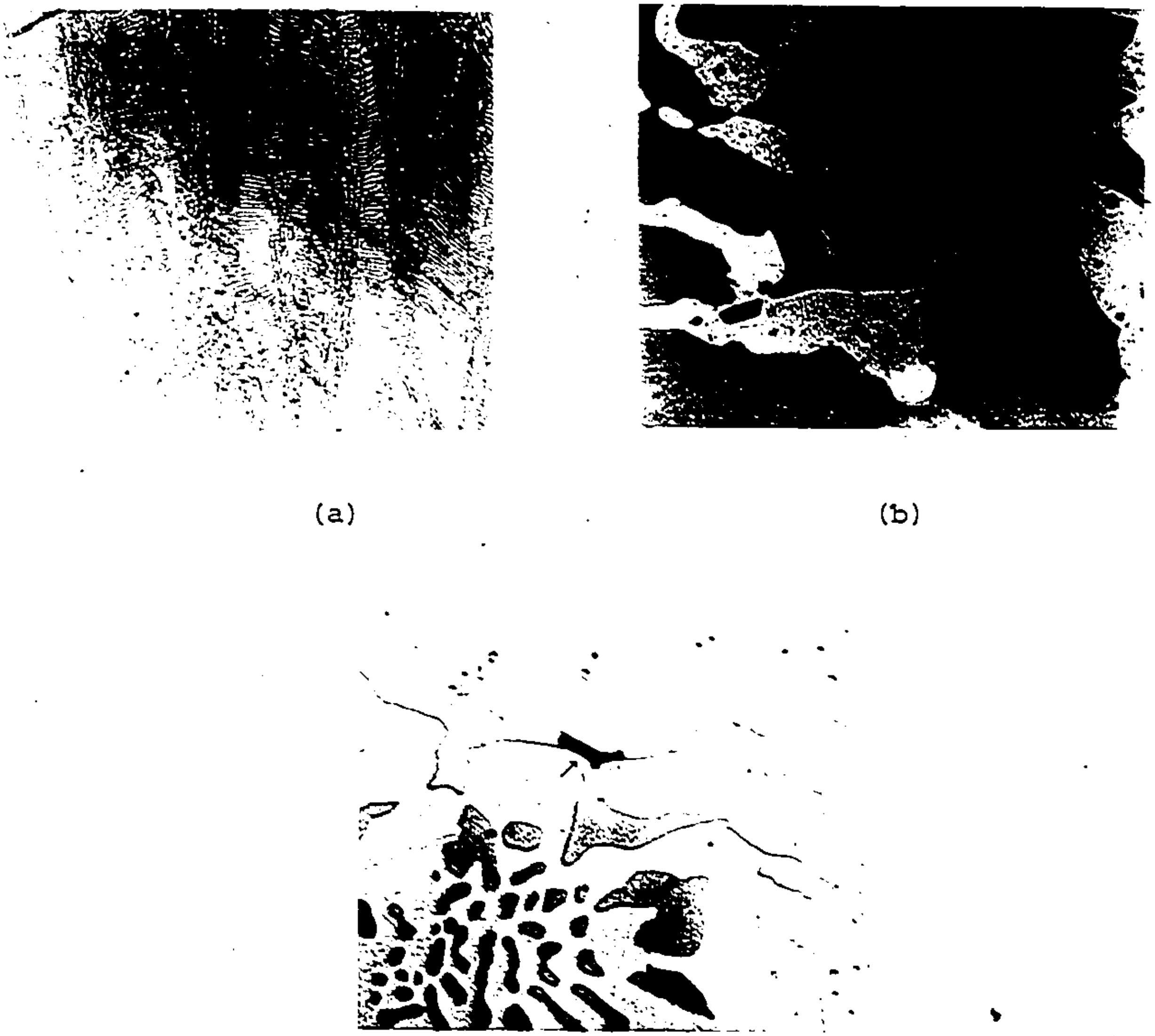
(a)

(b)

(c)

Figure 48 Al-35%Cu alloy (eutectic composition); (a) no Be added; (b) with 0.3%Be; (c) with 0.5%Be. Note the formation of a new phase (arrowed) in (c).

Alloys with eutectic composition (Al-35%Cu) containing 0, 0.14, 0.3 and 0.5%Be were prepared to metallographically estimate the maximum content of Be in θ phase (Figure 48). Only Al and θ were observed in alloys with 0, 0.14 and 0.3%Be, indicating that the θ phase has absorbed all added Be (the solubility of Be in Al is 0.06% at 640°C). In the eutectic alloy containing 0.5%Be, a new phase within the θ regions is observed. Noting that θ phase comprises 61% of the eutectic alloy, the metallographic study suggests that the maximum concentration of Be in θ phase is ~0.8% (~3 atomic percent).

A final attempt was made to analyze directly the θ particles in an overaged Al-3%Cu-0.1%Be alloy, using the extraction technique of F.H. Cocks et al(92). The procedure includes the dissolution of Al matrix in an electrolyte and separating the extracted particles from the solution in a centrifuge. The powder was analyzed by the Debye-Scherrer method and the results (Appendix II, Table 2) confirm the presence of θ phase. Diffraction lines of γ phase were also observed and identified as the second phase present in the homogenized Al-3%Cu-0.1%Be alloy. The diffraction lines, although clearly visible, were somewhat diffuse and no attempt was made to measure the change in lattice parameters a, c of θ from the Debye-Scherrer diffraction pattern.

Using a Beckman Spectra-Scan D.C. Plasma, microprocessor controlled spectrometer, model SS-3B, analysis of the extracted powder was performed by Met-Chem Testing Laboratories, and the total Be content of the powder was found to be 2.07%. The presence of γ phase in the extracted powder, prevents assigning this value to θ phase only. However, these results provide direct evidence that at least one of the γ and the θ phases absorb Be.

The combined results of hardness, EDS, X-ray diffraction metallography and the extraction technique indicate that Be is absorbed by the θ phase and that it is the Al component that is predominantly replaced. The concentration of Be in θ can be stated only approximately, and is in the range of 0.8-1.7%, as indicated by the EDS and metallographic analyses. The approximate stoichiometric formula $Cu(Al_{1.9}Be_{0.1})$, used in calculations of entropy of nucleation, corresponds to ~0.8%Be thereby giving the low boundary for entropy effect.

CHAPTER VI

CALCULATION OF NUCLEATION ENTROPY

A. Al-Cu SYSTEM: NUCLEATION ENTROPY OF $CuAl_2$

The procedure used to calculate the nucleation entropy for precipitation in solid alloys is similar to that for primary phase nucleation in liquid alloys, except that the solidification reaction must be replaced by the appropriate solid phase transformation, and the corresponding entropy change calculated or estimated. Table 4 gives the reaction sequence for calculating the molar nucleation entropy for the compound $CuAl_2$. The starting or initial condition is a solution-treated Al-1.3Cu alloy, and the reaction or aging temperature is $653^{o}K$. The reactions and sequence to be used in any given case are determined by the thermodynamic data available. For $CuAl_2$ the thermodynamic data available is for the liquid Al-Cu system$^{(98)}$, and the reaction sequence must be constructed around the formation reaction given for the liquid compound. In Table 4, the (reverse) formation of 1 mole (3g-atom) of regular liquid solution of Al-33.3Cu alloy is given by reaction 1a, for which the entropy change (-15.84) is given by:

$$\Delta S = -R(N_{Al}\ell nN_{Al} + N_{Cu}\ell nN_{Cu}) \qquad (39)$$

The formation entropy of 1 mole of liquid $CuAl_2$ at 1373K (reaction 2a) is taken from the data given by Hultgren et al$^{(98)}$. Adding 1a to 2a gives 3a, the reaction and corresponding entropy change (8.16) for the transformation of 1 mole

Table 4

Reaction Sequence for Calculating Molar Entropy of Nucleation of $CuAl_2$ From Al-1.3%Cu Alloy at 653°K

Reaction				ΔS, J $mol^{-1}K^{-1}$
1a	$3(Al\text{-}33.3\%Cu)^{reg}(\ell)$	$\rightarrow$	$Cu(\ell) + 2Al(\ell)$	-15.84
+				
2a	$Cu(\ell) + 2Al(\ell)$	$\xrightarrow{1373K}$	$CuAl_2(\ell)$	+24.00
3a	$3(Al\text{-}33.3\%Cu)^{reg}(\ell)$	$\xrightarrow{864K}$	$CuAl_2(\ell)$	~ + 8.16
+				
4a	$3(Al\text{-}33.3\ Cu)^{reg}(s)$	$\xrightarrow{864K}$	$3(Al\text{-}33.3\%Cu)^{reg}(\ell)$	~ 32.76
+				
5a	$CuAl_2(\ell)$	$\xrightarrow{864K}$	$CuAl_2(s)$	-43.70
6a	$3(Al\text{-}33.3\%Cu)^{reg}(s)$	$\xrightarrow{653K}$	$CuAl_2(s)$	~ - 2.78
+				
7a	$\infty(Al\text{-}1.3\%Cu)^{reg}(s)$	$\xrightarrow{653K}$	$3(Al\text{-}33.3\%Cu)^{reg}(s) +$ $\infty(Al\text{-}1.3\%Cu)^{reg}(s)$	~ -19.54
8a	$\infty(Al\text{-}1.3\%Cu)^{reg}(s)$	$\xrightarrow{653K}$	$CuAl_2(s) + \infty(Al\text{-}1.3\%Cu)^{reg}(s)$	~ -22.32

of regular liquid solution alloy to the real liquid compound. The entropy change for 3a is for 1373K, and it is necessary to calculate the corresponding entropy change for 864K, i.e., the fusion temperature of $CuAl_2$, since the fusion reaction and fusion entropy is used in the reaction sequence (reaction 5a). The absence of heat capacity information for the compound does not permit a temperature correction to the entropy change for 3a; however, the correction will be small, since it may reasonably be assumed that the heat capacities for the regular solution and real liquid alloy will not differ appreciably. The fusion of 1 mole of regular solid solution alloy of $CuAl_2$, composition is given in reaction 4a, for which the entropy change is the sum of the fusion entropies for the elements (2Al, 1Cu). The temperature correction is again omitted as the resulting correction is less than 4% (Appendix III).

The solidification of the compound is given in reaction 5a, for which the fusion entropy (-43.70) is taken from the data given by Smithells$^{(99)}$. Adding 3a, 4a, and 5a, gives reaction 6a, the (reverse) transformation of 1 mole of the real compound $CuAl_2$ to its regular solution counterpart, for which the entropy change is -2.78.

Reaction 7a denotes the nucleation reaction by which 1 mole of regular solid solution of Al-33.3%Cu alloy is formed in an infinite (∞) amount of regular solid solution of Al-1.3%Cu alloy. In the most general case, the entropy change for the nucleation reaction in the solid state is given by:

$$\Delta S = \Delta S_{TR} + \Delta S_M \qquad (40)$$

where,

$$\Delta S_{TR} = N^{\theta}_{Al}(S^{\theta}_{Al}-S^{\alpha}_{Al}) + N^{\theta}_{Cu}(S^{\theta}_{Cu}-S^{\alpha}_{Cu}) \quad (41)$$

$$\Delta S_{M} = R\ N^{\theta}_{Al}\ell n(N^{\alpha}_{Al}/N^{\theta}_{Al}) + N^{\theta}_{Cu}\ell n(N^{\alpha}_{Cu}/N^{\theta}_{Cu}) \quad (42)$$

and the superscripts θ and α refer to the bct and fcc structures of the θ compound and pure metals respectively. The inclusion of S_{TR} in S would denote that the regular solid solution 3(Al-33.3%Cu) appearing on the right-hand side of reaction 7a is referred to as the bct structure of the compound. However, in the reaction sequence of Table 4, the regular solid solutions in reactions 4a and 6a are referred to as the fcc structures of the components. As the same fcc reference state must be used in reaction 7a, the need for the $\alpha \rightarrow \theta$ transformation is removed, and S_M (Equation 42) constitutes the total entropy change for the nucleation reaction 7a. Adding 6a to 7a to obtain 8a removes the regular solution constraint for the compound, and reaction 8a gives the nuclation reaction and corresponding nucleation entropy for the formation of 1 mole of $CuAl_2$ from a regular behaving solid solution of Al containing 1.3%Cu at the tempering temperature of 653K.

The determination of the nucleation entropy of $CuAl_2$ from the real solid solution alloy requires appropriate thermodynamic information for the latter, which is not available. However, since the difference in molar entropies of mixing for regular and real solutions is small for dilute alloys (both converge and become zero at infinite dilution), the difference in the molar entropy for nucleation of $CuAl_2$, in the real vs. regular solid solution will be negligible for the Cu concentration in the present alloy ($N_{Cu} = 0.013$).

B. Al-Cu-Be SYSTEM: NUCLEATION ENTROPY OF $CuAl_{1.9}Be_{0.1}$

The results of the EDS and metallographic analysis of the θ phase containing Be show that the bct $CuAl_2$ phase dissolves up to 1.7%Be, and the decrease in the Al content indicates that Be atoms are incorporated (most probably) by displacing the Al atoms. Thus, the compound $CuAl_{1.9}Be_{0.1}$ is assumed to form (precise calculations give $Cu_{0.97}Al_{1.91}Be_{0.11}$) and Table 5 gives the appropriate reactions and sequence for calculating the molar nucleation entropy. The initial or starting condition is Al-1.3Cu-0.3Be solid alloy, solution treated at 873K to give a solid solution containing 1.3Cu and 0.1Be (assuming the maximum Be dissolved is given by the Al-Be phase diagram(100)). The procedure is essentially identical to that performed for the $CuAl_2$ phase except for two approximations required for lack of any thermodynamic data for the ternary compound. First, it is assumed that the formation entropy of the ternary liquid compound (reaction 2b) is approximately equal to the formation entropy of liquid $CuAl_2$. The basis for this assumption is the common bct structure, with the Be atom displacing 5% of the Al atoms, to give approximately similar short range orders for the liquid compounds.

The second approximation is the fusion entropy for $CuAl_{1.9}Be_{0.1}$ which is taken to be that for $CuAl_2$. The same argument given for the formation entropy approximation applies here also, i.e., the common crystal structure and the displacement of only 5% of Al atoms by Be atoms should not alter the bonding characteristics in the compound significantly.

It is noted that the 32% increase (negative) in the molar nucleation entropy derives mostly from the Be contribution to the mixing entropies (c.f., reaction 1b and 7b), which is not altered by errors introduced in the above approximations.

Table 5

Reaction Sequence for Calculating Molar Entropy of Nucleation of $CuAl_{1.9}Be_{0.1}$ From Al-1.3%Cu-0.1%Be Solid Solution Alloy at 653°K

Reaction				ΔS, $Jmol^{-1}K^{-1}$
1b	$3(Al\text{-}32.5\%Cu\text{-}3.8\%Be)^{reg}(\ell)$	$\rightarrow$	$Cu(\ell) + 1.9Al(\ell) + 0.01Be(\ell)$	-19.20
+				
2b	$Cu(\ell) + 1.9Al(\ell) + 0.1Be(\ell)$	$\xrightarrow{1373K}$	$CuAl_{1.9}Be_{0.1}(\ell)$	~ +24.00
3b	$3(Al\text{-}33.3\%Cu\text{-}3.3\%Be)^{reg}(\ell)$	$\xrightarrow{864K}$	$CuAl_{1.9}Be_{0.1}(\ell)$	~ + 4.80
+				
4b	$3(Al\text{-}33.3\%Cu\text{-}3.3\%Be)^{reg}(s)$	$\xrightarrow{864K}$	$3(Al\text{-}33.3\%Cu\text{-}3.3\%Be)(\ell)$	~ +32.35
+				
5b	$CuAl_{1.9}Be_{0.1}(\ell)$	$\xrightarrow{864K}$	$CuAl_{1.9}Be_{0.1}(s)$	~ -43.70
6b	$3(Al\text{-}33.3\%Cu\text{-}3.3\%Be)^{reg}(s)$	$\xrightarrow{423K}$	$CuAl_{1.9}Be_{0.1}(s)$	~ - 6.55
+				
7b	$\infty(Al\text{-}1.3\%Cu\text{-}0.1\%Be)^{reg}(s)$	$\xrightarrow{423K}$	$3(Al\text{-}33.3\%Cu\text{-}3.3\%Be)^{reg}(s) +$ $\infty(Al\text{-}1.3\%Cu\text{-}0.1\%Be)^{reg}(s)$	~ -22.70
*B	$(Al\text{-}1.3\%Cu\text{-}0.1\%Be)^{reg}(s)$	$\xrightarrow{423K}$	$CuAl_{1.9}Be_{0.1}(s) + \infty(Al\text{-}1.3\%Cu\text{-}0.1\%Be)^{reg}(s)$	~ -29.25

CHAPTER VII

CALCULATIONS OF STRAIN ENERGY, ΔG* AND RELATIVE NUCLEATION RATES

Transformations in the solid state are usually accompanied by volume changes that result in strain energy, which must be included in the free energy of nucleation of the critical-sized nucleus ΔG*. Nabarro(84) has shown that for incoherent precipitate the spherical form of precipitate has maximum strain energy (Fig. 1) and that the strain energy approaches zero for very thin plates ($c \ll r$).

In the present work, the incoherent case is analyzed and θ particles are assumed to be initially thin plates with c/r ratio equal to 1/20, similar to reported values for θ' precipitates(101). Allowance is made for the larger volumetric change (negative) in the $Cu(Al_{1.9}Be_{0.1})$ formation, as obtained from X-ray diffraction analysis. Calculations of strain energy are presented in Appendix IV and summarized in Table 6. The results indicate that within the approximations made, the strain energy of $Cu(Al_{1.9}Be_{0.1})$ is higher as compared to $CuAl_2$. The entropy term of $Cu(Al_{1.9}Be_{0.1})$ (eqn. (40)) must therefore be significantly larger to override the increased elastic energy and to enhance the nucleation rate.

When considering the role of strain energy in θ formation, it must be noted that the actual transformation took place at $T \sim \frac{1}{2} T_M^{Al}$ (T_M^{Al} is the melting temperature of Al) at which the relaxation processes are operative(102). The elastic constants have significantly lower value (30% decrease

Table 6

Strain Energy, ΔG* and Relative Nucleation Rate of $Cu(Al_{1.91}Be_{0.1})$ and $CuAl_2$

Phase	V $cm^3(g\cdot at^{-1})$	ΔV/V Al matrix	$W(f(\frac{c}{r})=0.1)$ Jcm^{-3}	$\lvert\Delta S_v\rvert$ $Jcm^{-3}K^{-1}$	$\Delta G^*(\Delta T=90^oK)$ $\gamma=3.25\times10^{-5}Jcm^{-2}$ $J\times10^{-23}$	$\frac{\dot{N}^{Cu(Al_{1.9}Be_{0.1})}}{\dot{N}^{CuAl_2}}$
Al	9.89	---	---	---	---	---
$CuAl_2$	8.95	-0.108	4.4	0.83	14847	---
$Cu(Al_{1.9}Be_{0.1})$	8.86	-0.116	5.1	1.10	9011	$\sim3.16\times10^{19}$

for Al(103) and the combined effect is to lower the actual elastic energy contribution to the nucleation process.

ΔG*, the free energy change associated with the formation of critical nuclei, is obtained using eqn. (32). The relative nucleation rates of $Cu(Al_{1.9}Be_{0.1})$ and $CuAl_2$ are calculated by inserting ΔG* values in eqn. (51), and taking γ the interfacial energy to be $\gamma = 3.25 \times 10^{-5} Jcm^{-2}$ (which is approximately half of the interfacial energy obtained from investigation of coarsening rate of θ(104)). The calculations are presented in Appendix V and summarized in Table 6. The results in Table 6 show that, although the incorporation of Be into the precipitate compound increases the strain energy by ~16%, the increase in ΔS_v more than offsets the strain energy effect to give a net decrease of ~39% in the free energy of formation of the critical-sized nucleus. This is a consequence of the dependence of ΔG* on the 4th power of ΔS_v and the square power of strain energy W (c.f., eqn. (32)). The higher calculated nucleation rate for the Al-3%Cu-0.1%Be alloy is consistent with the higher 'k' values obtained for the $Cu(Al_{1.9}Be_{0.1})$ precipitation, higher initial densities of θ particles and the observed faster θ'→θ transition in the Al-3%Cu-0.1%Be alloy.

CHAPTER VIII

CONCLUSIONS

From the results of the investigation, the following conclusions are presented:

1) Addition of 0.1%Be to Al-3%Cu alloy increases significantly the hardening rate when aging at room temperature and at 110°C.

2) Large dislocation loops, closely associated with dislocation lines were observed in Al-3%Cu-0.1%Be alloy, aged to the hardness plateau (530h at 110°C). GP zones are not present at this stage and an additional aging of 15h at 150°C was required to initiate the GP zone formation.

3) It is proposed that the increased hardening rate in Al-Cu-Be alloy is due to a clustering process in which stable clusters of Cu-Be and vacancies are formed in the immediate vicinity of dislocation lines. As a result, due to the depletion of Cu and vacancies, GP zone formation is delayed.

4) The temporary softening in Al-3%Cu-0.1%Be alloy during aging at 150°C is seen as a reversion of the clustering process. Subsequently, GP zones are formed in the matrix as observed experimentally. The dislocation loops observed at the plateau hardness are thought to be large clusters which have collapsed to form loops.

5) θ' precipitation in Al-3%Cu and Al-3%Cu-0.1%Be alloys proceeds according to an Avrami type equation with n = 1.6-1.7 and an activation energy of~76-85 kJ. The

relatively low activation energy indicates that rate controlling process involves diffusion along dislocation lines. Slow thickening of θ' plates results in growth characteristics intermediate between the two models proposed by Ham: a plate with constant thickness ($n=2$) and constant aspect ratio ($n=3/2$).

6) θ formation in Al-3%Cu and Al-3%Cu-0.1%Be alloys proceeds according to Harper eqn., with $n=0.63-0.72$ and an activation energy of ~108-111 kJ. It is suggested that the dissolution of θ' particles during θ formation creates a quasi-steady solute distribution and extends the applicability of Harper eqn. to longer times. The proposed sequence of θ formation involves dissolution of θ', transport of Cu atoms to dislocations (this step is responsible for the "precipitation on dislocation" character) and by pipe diffusion to the growing θ precipitate.

7) Estimation of the strain energy of an incoherent θ precipitate indicates that Be incorporation in θ phase increases the strain energy of precipitation.

8) The nucleation entropy of θ was calculated from appropriate combination of reactions. Significantly larger (absolute) entropy of formation was obtained for phase with Be, the increase being largely due to 21% change in the entropy of mixing.

9) According to the nucleation entropy theory, the incorporation of Be in θ phase leads to higher nucleation rate in agreement with the experimental results.

CHAPTER IX

RECOMMENDATION FOR FUTURE RESEARCH

1) Further study of the clustering process in Al-Cu-Be alloys is required to establish the kinetic process of cluster formation, the cluster composition and stability, and to understand the cluster GP zone transition. This stage of precipitation process has not been fully investigated yet. Resistivity and small angle X-ray diffraction (SAXD) are suggested experimental techniques.

2) The role of dislocation loops and the possibility they represent larger clusters that have collapsed merits investigation. The stability of the loops, presence of Cu and Be and the loops interaction with dislocation lines are to be defined, using hot stage electron microscopy and electron energy loss (EELS) system analysis.

3) In the study of θ nucleation, continuous observation of θ formation (using hot stage electron microscopy) is needed to identify nucleation sites and to verify the role of dislocation network in the transportation process.

4) A study of coarsening rate of θ particles would permit estimation of θ/matrix interfacial energy (using Lifshitz-Wagner Theory), and ascertain whether the interfacial energy is not altered by Be incorporation.

5) The ability of resistivity technique to locate the $\theta' \rightarrow \theta$ transition should be noted and utilized in other metastable→stable transformations. This allows the construction of metastable phase and TTT diagrams, and

allows better control of the aging procedure.

6) Further investigation is required to establish the Be content of θ phase and to ascertain that Be replaces Al preferentially. The possible experimental techniques include EELS and SAXD.

REFERENCES

1. A. Gunier: Nature, Vol. 142, 1938, p. 569.
2. G.D. Preston: Nature, Vol. 142, 1938, p. 570.
3. G.D. Preston: Phil. Mag. Vol. 26, 1938, p. 855.
4. A. Gunier: J. Phys. Radium, Vol. 8, 1942, (3), p. 124.
5. J.M. Silcock et al: J. Inst. Met., Vol. 82, 1953-4, p. 239.
6. W. DeSorbo et al: Acta Met., Vol. 6, 1958, p. 401.
7. D. Turnbull et al: Acta Met., Vol. 8, 1960, p. 277.
8. C.W. Tucker, Jr., and M.B. Webb: Acta Met., Vol. 7, 1959, p. 187.
9. E.W. Hart: Acta Met., Vol. 6, 1958, p. 553.
10. K.M. Entwistle et al: J. Inst. Met., Vol. 91, 1962-3, p. 84.
11. E. Holmes and B. Noble: J. Inst. Met., Vol. 95, 1967, p. 106.
12. B. Noble: Met. Sci., Vol. 2, 1968, p. 117.
13. T. Takahashi et al: J. Jpn. Inst. Light Met., Vol. 26, 1976, p. 587.
14. T. Abe et al: Acta Met., Vol. 30, 1982, p. 357.
15. H. Yoshida et al: Mat. Res. Soc. Symp. Proc., Vol. 21, 1984, p. 131.
16. A. Gunier: Ann. Phys., Vol. 12, 1939, p. 161.
17. A. Gunier: C.R. Acad. Sci. Paris, Vol. 231, 1950, p. 655.
18. R.B. Nicholson and J. Nutting: Phil. Mag., Vol. 3, 1958, p. 531.
19. V. Gerold: Z. Metalk., Vol. 45, 1954, p. 533 and 599.
20. V. Gerold: Acta Crystallogr., Vol. 11, 1958, p. 236.
21. K. Toman: Acta Crystallogr., Vol. 8, 1955, p. 587.
22. K. Toman: Acta Crystallogr., Vol. 10, 1957, p. 187.

23. K. Toman: Acta Crystallogr., Vol. 13, 1960, p. 60.

24. J.R. Parson et al: Phil. Mag., Vol. 21, 1970, p. 1105.

25. V.A. Phillips: Acta Metall., Vol. 21, 1973, p. 219.

26. V.A. Phillips: Acta Metall., Vol. 23, 1975, p. 751.

27. M. Yoshida et al: Phil. Mag., Vol. 34, 1976, p. 89.

28. X. Auvray et al: Acta Metall., Vol. 29, 1981, p. 1086.

29. H. Yoshida: "Solid to Solid Transformations," Proc. Conf. Pittsburg, Pa., 20-24 Aug. 1981, p. 363.

30. T. Abe et al: Acta Metall., Vol. 30, 1982, p. 357.

31. A.J. Bradley and D. Jones: J. Inst. Met., Vol. 51, 1933, p. 131.

32. C. Laird and H.I. Aaronson: Trans. TMS-AIME, Vol. 242, 1968, p. 1393.

33. H.I. Aaronson and C. Laird: Trans. TMS-AIME, Vol. 242, 1968, p. 1437.

34. R. Sankaran and C. Laird: Acta Metall., Vol. 22, 1974, p. 957.

35. Y.H. Chen and R.D. Doherty: Scrip. Metall., Vol. 11, 1977, p. 725.

36. J. Papazian: Metall. Trans., Vol. 13A, 1982, p. 761.

37. P. Merle et al: Scrip. Metall., Vol. 15, 1981, p. 373.

38. K.R. Kinsman et al: Acta Metall., Vol. 15, 1967, p. 1244.

39. D. Waughan and J.M. Silcock: Phys. Stat. Sol., Vol. 20, 1967, p. 725.

40. C. Laird and H.I. Aaronson: Acta Met., Vol. 14, 1968, p. 171.

41. J.B. Murphy: Acta Metall., Vol. 9, 1961, p. 563.

42. S. Kang and C. Laird: Acta Metall., Vol. 22, 1974, p. 1481.

43. E.P. Buttler: "Solid to Solid Transformation," Proc. Conf., Pittsburg, Pa., 20-24 Aug. 1981, p. 673.

44. A.H. Sully et al: J. Inst. Met. Vol. 76, 1949-50, p. 269.

45. H.K. Hardy: J. Inst. Met., Vol. 80, 1951-52, p. 483.

46. H.K. Hardy et al: J. Inst. Met., Vol. 82, 1953-54, p. 236.

47. J.M. Silcock et al: J. Inst. Met., Vol. 84, 1955-56, p. 23.

48. J.M. Silcock: Phil. Mag., Vol. 4, 1959, p. 1187.

49. J.B.M. Nuyton: Acta Met., Vol. 15, 1967, p. 1765.

50. S.K. Das et al: Septieme Congres International de Microscope Electronique, Grenoble, 1970, p. 533.

51. R. Sankaran and C. Laird: Mat. Science Eng., Vol. 14, 1974, p. 271.

52. H. Suzuki et al: J. Jpn. Inst. Light Met., Vol. 30, 1980, p. 3.

53. W.L. Fink et al: Trans. Amer. Inst. Min. Met. Eng., Vol. 128, 1938, p. 223.

54. A. Chitty: J. Inst. Met., Vol. 86, 1957-58, p. 65.

55. M.L.V. Gayler: J. Inst. Met., Vol. 60, 1937, p. 75.

56. W. Koch and T.W. Nothing: Aluminum, Vol. 17, 1935, p. 535.

57. J.B.M. Nuyton: Scrip. Met., Vol. 3, 1967, p. 645.

58. B. Noble et al: Acta Met., Vol. 18, 1970, p. 339.

59. M. Volmer and A. Weber: Z. Phys. Chem., Vol. 119, 1926, p. 227.

60. R. Becker and W. Doring: Ann. Phys., Vol. 24, 1935, p. 719.

61. D. Turnbull and J.C. Fisher: J. Chem. Phys., Vol. 17, 1949, p. 71.

62. J.W. Christian: "The Theory of Transformations in Metals and Alloys," 1964, Oxford (Pergamon Press), p. 537.

63. W.V. Youdelis: Met. Science, Vol. 9, 1975, p. 464.

64. W.V. Youdelis: Met. Science, Vol. 13, 1979, p. 540.

65. S.P. Iyer and W.V. Youdelis: Aluminum, Vol. 53, 1977, p. 152.

66. W.V. Youdelis and S.P. Iyer: Aluminum, Vol. 2, 1979, p. 152.

67. C-S. Yang: Thesis, University of Windsor, 1980.

68. W.V. Youdelis: Met. Science, Vol. 12, 1978, p. 363.

69. A. Ramon and K. Schubert: Z. Metallkd., 1965, p. 44.

70. G.W. Delamore and R.W. Smith: Metal. Trans. Vol. 2, 1971, p. 1733.

71. W.V. Youdelis and O. Kwon: Met. Science, Vol. 17, 1983, p. 379.

72. W.V. Youdelis and O. Kwon: Met. Science, Vol. 17, 1983, 385.

73. W.A. Johnson and R.F. Mehl: Trans. Amer. Inst. Min. Engrs., Vol. 135, 1939, p. 416.

74. M. Avrami: J. Chem. Phys., Vol. 71, 1939, p. 1103.

75. J.W. Christian: "The Theory of Transformations in Metals and Alloys," 1964, Oxford (Pergamon Press), p. 489.

76. C. Wert and C. Zener: J. Appl. Phys., Vol. 21, 1950, p. 5.

77. C.A. Wert: J. Appl. Phys., Vol. 20, 1949, p. 943.

78. F.S. Ham: J. Phys. Chem. Solids, Vol. 6, 1958, p. 335.

79. F.S. Ham: J. Appl. Phys., Vol. 30, 1959, p. 1518.

80. A.H. Cottrell and B. Bilby: Proc. Phys. Soc. (London) Series A, Vol. 62, 1949, p. 45.

81. S. Harper: Phys. Rev., Vol. 83, 1951, p. 709.

82. F.S. Ham: J. Appl. Phys., Vol. 30, 1959, p. 915.

83. J.W. Christian: "The Theory of Transformation in Metals and Alloys," 1964, Oxford (Pergamon Press) p. 188.

84. F.R.N. Nabarro: Proc. Roy. Soc., Vol. A175, 1940, p. 519.

85. J.D. Eshelby: Proc. Roy. Soc., Vol. A241, 1957, p. 376.

86. A.G. Khachaturyan: Sov. Phys. Solid State, Vol. 8, 1967, p. 2163.

87. J.A. Wert: Acta Met. Vol. 24, 1976, p. 65.

87a. N. Kinoshita and T. Mura: Phys. Stat. Sol. (A) Vol. 5, 1971, p. 759.

88. D.M. Barnett et al: Scripta Met., Vol. 8, 1954, p. 1447.

89. J.K. Lee et al: Met. Trans., Vol. 8A, 1977, p. 963.

90. N. Raghaven and M. Cohen: "Solid-State Phase Transformations," 'Treatise on Solid State Chemistry,' Vol. 5, Ed. N.B. Hannay, 1975, (Plenum Press), p. 67.

91. A.K. Jena et al: J. Mater. Science, Vol. 16, 1981, p. 2544.

92. F.H. Cocks et al: J. Mater. Science, Vol. 12, p. 494.

93. E.E. Bloom: "Irradiation Strengthening and Embrittlement," 'Radiation Damage in Metals,' Ed. N.L. Peterson and S.D. Harkness, 1975, (Metals Park, Ohio, ASM), p. 295.

94. G. Das and J. Washburn: Phil. Mag., Vol. 11, 1965, p. 955.

95. G. Thomas and M.J. Whelan: Phil. Mag., Vol. 4, 1955, p. 511.

96. V. Dahmen and K.M. Westmacott: Phys. Stat. Sol. a, Vol. 80, 1983, p. 249.

97. E. Hornborg: "Nucleation of Precipitates in Defect Solutions," 'Nucleation,' Ed. A.C. Zettlemonger, 1969, New York (Marcel Dekker, Inc.), p. 354.

97a. J.W. Cahn: Acta Met., Vol. 10, 1962, p. 907.

97b. M. Murakami et al: J. Inst. Metals (London), Vol. 99, 1971, p. 160.

97c. De Fontaine: "Treatise on Solid State Chemistry," Vol. 5, Ed. N.B. Hannary, 1975, New York (Plenum Press), p. 129-178.

98. R. Hultgren et al: "Selected Values of the Thermodynamic Properties of Binary Alloys," 1973, (Metals Park, Ohio, ASM), p. 151.

99. C.J. Smithells: Metals Reference Book, 1967, London (Butterworths), p. 226.

100. M. Hansen: "Constitution of Alloys," 1958, (McGraw-Hill), p. 73.

101. P. Merle and J. Merlin: Acta Met., Vol. 29, 1981, p. 1929.

102. J.W. Christian: "The Theory of Transformation in Metals and Alloys," 1964, Oxford (Pergamon Press), p. 417.

103. C. Zener: "elasticity and Anelasticity of Metals," 1948, Chicago, Illinois, (The University of Chicago Press), p. 24.

104. D. Janoff and M.E. Fine: Mater. Science Eng., Vol. 64, 1984, p. 67.

105. R.C. Weast: "Handbook of Chemistry and Physics," 1976-77, Cleveland, Ohio, (CRC Press), p. D-62.

106. J.P. Hirth and J. Lothe: "Theory of Dislocations," 1968, New York (McGraw-Hill), p. 761.

107. L. Guillet and R. Le Roux: "Intermetallic Compounds," Ed. J.H. Westbrook, 1967, (John Wiley), p. 456.

108. J.M. Silcock and C. Ellwood: J. Inst. Met., Vol. 74, 1948, p. 457.

109. W.B. Pearson: "A Handbook of Lattice Spacings and Structures of Metals and Alloys," 1958, (Pergamon Press), Vol. 1, p. 329.

APPENDIX I

Shift in Principal X-ray Reflection and the Calculated Change in Lattice Parameters in Al_2Cu-Be as Compared to Al_2Cu

Lattice Plane	Shift in 2θ (deg.)	Decrease in a,c(%)
110	+0.15	
200	0.0	
121	+0.25	
112	+0.1	a = 0.4 %±0.2%
222	+0.2	c = 0.55%±0.2%
123	+0.55	
240	+0.15	
332	+0.3	
134	+0.6	

APPENDIX II

Debye-Scherrer Analysis of Extracted Powder

$2\theta^{\circ}$	d($\mathring{A}$)	Planes of $\theta(h,k,\ell)$	Planes of $\gamma(h^2+\rho_2^2+\ell^2)$
21.4	4.35	110	
26.0	3.43		6
30.5	2.93		9
39.1	2.30	121	
43.0	2.10	112	
44.1	2.06		18
48.4	1.88	(130 & 202)	21
50.2	1.82		22
58.0	1.59	222	
67.2	1.39	123	
70.0	1.34	240	42
76.7	1.24	332	48
78.2	1.22	004	50,51
82.3	1.20	(150 & 242)	53
90.0	1.08	152	
93.3	1.06	224	

APPENDIX III

APPENDIX III

Temperature correction for reaction 4a (Chapter V) is calculated below, using the appropriate C_p values$^{(105)}$ for Al and Cu in liquid and solid state:

$$\begin{aligned}
\Delta S_{Al}^{\rightarrow\ell}(864^{o}K) &= \Delta S_{Al}^{s\rightarrow\ell}(932^{o}K) + \int_{932}^{864} \Delta C_p^{Al} d\ell nT \\
&= 2.76 + \int_{932}^{864} (2.06-0.00286T)d\ell nT \\
&= 2.8 \text{ e.u.}
\end{aligned}$$

$$\begin{aligned}
\Delta S_{Cu}^{s\rightarrow\ell}(864^{o}K) &= \Delta S_{Cu}^{s\rightarrow\ell}(1356^{o}K) + \int_{1356}^{864} \Delta C_p^{Cu} d\ell nT \\
&= 2.29 + \int_{1356}^{864} (2.1-0.0015T)d\ell nT \\
&= 2.08 \text{ e.u.}
\end{aligned}$$

$$\begin{aligned}
\Delta S_{3(Al-33.3Cu)}^{s\rightarrow\ell}(864^{o}K) &= 2\Delta S_{Al}^{s\rightarrow\ell}(864) + \Delta S_{Cu}^{s\rightarrow\ell}(864) \\
&= 7.68 \text{ e.u.} \\
&= 32.1 \text{ J/mol}^{o}K
\end{aligned}$$

The resulting correction is less than 4% and has been omitted in the view of the extrapolation involved and the relatively inaccurate heat capacity for liquid metals.

APPENDIX IV

For a plate-like incoherent θ precipitate, the strain energy per atom is:

$$W_1 = C_6\ 2\mu^{Al}((v^{CuAl_2} - v^{Al})^2/3v^{CuAl_2})\cdot 3\pi c/4r \qquad (48)$$

with,

$$\frac{c}{r} \sim \frac{1}{20}$$

$$\mu^{Al} = 2.85 \times 10^{11}\,\mathrm{dyn/cm^2}\,(106)$$

$$C_6 = K^{CuAl_2}/(3K^{CuAl_2} + 4\mu^{Al}) \qquad (49)$$

and,

$$K^{CuAl_2} = \frac{\mu^{CuAl_2}\cdot 2(1+\nu)}{3(1-2\nu)} \qquad (50)$$

Taking, $\nu = 0.31$, and $\mu^{CuAl_2} = 3.6 \times 10^{11}\,\mathrm{dyn/cm^2}$ (107), the calculated K^{CuAl_2} and C_6 are: $K^{CuAl_2} = 8.3 \times 10^{11}\,\mathrm{dyn/cm^3}$ and $C_6 = 0.2$ respectively.

v^{Al} is the average volume of atom in matrix, using the x-ray data of Silcock and Ellwood (108) for Al-2.98%Cu, v^{Al} is calculated to be 0.01642 nm^3. The average atomic volume in CuAl$_2$ is obtained by dividing the volume of unit cell into 12 parts (number of atoms per unit cell) giving the volume of 0.01483 nm^3 (in good agreement with gram·atom volume data given by Pearson (109)). Thus,

$$(v^{CuAl_2} - v^{Al})^2/3v^{CuAl_2} = 0.057 \times 10^{-24}\ \mathrm{cm^3}$$

Substituting all the values back to eqn. (48), we obtain,

$$W_1 = 6.5 \times 10^{-16}\ \mathrm{erg/atom}$$

Elastic energy per unit volume is obtained by multiplying by the number of atoms in 1 cm^3 which is:

$$n = \frac{12}{178} \times 10^{-24}\text{cm}^3 = 0.674 \times 10^{23}\text{atom/cm}^3$$

giving,

$$W_1 = 4.4 \text{ J/cm}^3.$$

For $Cu(Al_{1.9}Be_{0.1})$ precipitate, the X-ray diffraction analysis (Chapter IV) indicates that the unit cell of $Cu(Al_{1.9}Be_{0.1})$ is smaller than that of $CuAl_2$. The new lattice constants are: a = 0.6042nm and c = 0.4837 nm. The corresponding volume of unit cell is 0.17658 nm³ and the average atomic volume is 0.014715 nm³. Using this value for $V^{Cu(Al_{1.9}Be_{0.1})}$, $\Delta V^2/3V$ is recalculated:

$$\frac{\Delta V^2}{3V} = \frac{(V^{Cu(Al_{1.9}Be_{0.1})} - V^{Al})^2}{3V^{Cu(Al_{1.9}Be_{0.1})}} = 0.066 \times 10^{-24}\text{ cm}^3$$

The new value of $\Delta V^2/3V$ is substituted in eqn. (48) giving:

$$W_1 = 5.1 \text{ J/cm}^3$$

APPENDIX V

ΔG^* for an incoherent-disc-shaped $CuAl_2$ precipitate is given by eqn. (32). Substituting the appropriate values of strain energy, the entropy change, and taking $\gamma = 3{,}25 \times 10^{-5}$ J/cm² gives for $\Delta T \sim 90^{\circ}K$:

$$\Delta G^* = [\frac{32\pi}{3} \cdot (4.4)^2 \cdot (3.25\text{x}10^{-5})]^3/(90 \cdot 1.23)^4$$

$$= 14847 \text{ x } 10^{-23}\text{J}$$

and for $Cu(Al_{1.9}Be_{0.1})$:

$$\Delta G^* = [\frac{32\pi}{3} \cdot (5.1)^2(3.25\text{x}10^{-5})]^3/(90 \cdot 1.5)^4$$

$$= 9011 \text{ x } 10^{-23}\text{J}$$

The relative nucleation rate of $Cu(Al_{1.9}Be_{0.1})$ and $CuAl_2$ is:

$$\frac{\dot{N}^{Cu(Al_{1.9}Be_{0.1})}}{\dot{N}^{CuAl_2}} = \frac{\exp[-\Delta G^{*Cu(Al_{1.9}Be_{0.1})}/kT]}{\exp[-\Delta G^{*CuAl_2}/kT]}$$

$$= \exp[(-9011 + 14847) \cdot 10^{-23}/1.38\text{x}10^{-23} \cdot 653]$$

$$= 6.36 \text{ x } 10^2$$

APPENDIX VI

COMMENTS ON RESISTIVITY MEASUREMENTS

Resistivity readings of samples aged at the various temperatures where obtained by interrupting the aging treatment, quenching the sample and measuring its resistivity in water bath (distilled and deionized) which was kept at $29^{\circ}C \pm 0.01^{\circ}C$. The resistivity data so obtained are then used to obtain the fraction transformed (ξ),

$$\xi = \frac{\rho_o - \rho_t}{\rho_o - \rho_\infty}$$

where ρ_o, ρ_t and ρ_∞ are the initial resistivity, the resistivity at time t and resistivity at the end of precipitation process. ρ_o is obtained by extrapolation of the later readings and is probably slightly higher than the true initial resistivity. (However, the extrapolations did give consistently the same value for ρ_o regardless of the aging temperature). Short time values of ρ_t are also subject to error due to the fact that it takes finite time to heat up the sample to the aging temperature.

In addition to errors inherent in the experimental procedure, it is assumed that the change in vacancies and dislocation densities contributes insignificantly to the overall decrease in resistivity which is taken to reflect the decrease in concentration only. The good agreement between TEM and resistivity results and between the metastable solvus of θ' obtained in this study and the work of Hornbogen suggest that the effects discussed above are not significant.

VITA AUCTORIS

1947	Born in Czechoslovakia
1961	Emigrated to Israel
1967	Military service in the Army - Israel
1977	Graduated with B.Sc. degree, Department of Mineral Engineering, Technion - Israel Institute of Technology.
1978	Engineer in the Powder Metallurgy Department, Iscar Ltd.
1981	Received M.Sc. degree, Department of Materials Engineering, Technion - Israel Institute of Technology
1981	Registered in Ph.D. program, Department of Engineering Materials, University of Windsor.